To My Parents,

Mr & Mrs Lincoln Lieu

RADIATION TRANSPORT WITHIN THE SOURCE OF HARD COSMIC X-RAY PHOTONS

A THESIS

submitted by

RICHARD LIEU

for the degree of

DOCTOR OF PHILOSOPHY

in the

UNIVERSITY OF LONDON

March 1981

ABSTRACT

Two important aspects of hard cosmic X-ray sources, viz. a source location technique and the radiation transport problem in accreting binary systems are studied. The former involves ground-based experiments and test flight of a tungsten modulation collimator rotating about a fixed axis. The frequency and phase of the modulation function serve to give an unambiguous determination of the position of an X-ray source in the sky. On the radiation transport problem, data analysis of the Vela X-1 binary results in one additional spectral point and two additional upper limits to previous observations. This, together with other reports on binary X-ray sources (Her X-1, 4U0115+63, 4U1626-67) strongly suggest the association of intense magnetic fields (10^{7}-10^{9} tesla) with the compact object and the quantum mechanical nature of electrons in the accreting plasma near the magnetic polar regions. Calculations of the cross sections for (quantized) cyclotron radiation, Compton scattering and thermal Bremsstrahlung in an intense magnetic field will be presented in detail.

TABLE OF CONTENTS

		Page
ABSTRACT		1
ACKNOWLEDGEMENTS		4
CHAPTER 1	INTRODUCTION TO X-RAY ASTRONOMY	5
1.1	Early History	5
1.2	The Ariel V Satellite with Special Reference to Experiment F	6
1.3	Nature and Identification of X-ray Sources	7
1.4	Galactic X-ray Sources	9
1.4.1	Supernova Remnants	10
1.4.2	Compact X-ray Sources	11
1.5	Extra-galactic X-ray Sources	13
1.5.1	Normal Galaxies	13
1.5.2	Active Galaxies	13
1.5.3	Seyfert Galaxies	14
1.5.4	Quasi-Stellar Objects	14
1.6	Conclusion	15
CHAPTER 2	THE MODULATION COLLIMATOR TECHNIQUE IN OBSERVATIONAL X-RAY ASTRONOMY	17
2.1	Introduction to the Modulation Collimator	17
2.2	Modulation Collimator - Construction	20
2.3	Detector and Electronics Devices	21
2.4	Tests performed in Laboratory	24
2.4.1	Depth of Modulation and Angular Response	25
2.4.2	The Effect of Tungsten Fluorescence on Modulation Properties	28
2.4.3	Laser Investigation of Modulation Properties and Angular Response	30
2.5	Modulation Collimator - Flight Configuration	31
2.6	The Test Flight	32
CHAPTER 3	ARIEL V HARD X-RAY OBSERVATION OF VELA X-1	36
3.1	Introduction	36
3.2	The Detector	36
3.3	The Observation	37
3.4	Data Analysis	38
3.5	Conclusion	47
CHAPTER 4	RADIATION PROCESSES IN THE MAGNETIC POLAR REGIONS OF AN ACCRETING BINARY PULSAR	49
4.1	Introduction to Binary X-ray Sources	49
4.2	Experimental Evidence of the Association of Strong Magnetic Fields with Pulsars	51
4.3	Compton Scattering	52
4.4	Cyclotron Bremsstrahlung	54
4.5	Vacuum Polarization	54
4.6	Overall Radiation Transport	55

		Page
CHAPTER 5	A NEW APPROXIMATION FOR THE HIGH MAGNETIC FIELD COMPTON CROSS SECTION	57
5.1	Introduction	57
5.2	Symmetry Properties of the Motion of a Charged Particle in a Uniform Magnetic Field	58
5.3	Absorption and Emission of Photon	60
5.4	The Calculation	63
5.5	The Electron Propagator	65
5.6	The S-Matrix	67
5.7	The Cross Section	70
5.8	Compton Resonances	73
CHAPTER 6	A REVISED CALCULATION OF THE BREMSSTRAHLUNG CROSS SECTION IN THE HIGH MAGNETIC FIELD OF PULSARS	80
6.1	Introduction	80
6.2	The S-Matrix	81
6.3	Bremsstrahlung Cross Section	90
6.4	Discussion	93
REFERENCES		103
APPENDIX		108

ACKNOWLEDGEMENTS

I express much gratitude and appreciation to my supervisor, Dr J.J. Quenby, for his consistent advice and encouragement. I owe much to Professor T.W.B. Kibble for his invaluable insight in quantum electrodynamics, which forms the backbone of the subject matter of Chapters 5 and 6. I am also deeply grateful to my parents, Mr and Mrs L. Lieu, for their financial support and for their counselling throughout the years.

People who have provided me help in the specific projects of the individual chapters are :

Professor H. Elliot for allowing me to work in his group and to use the facilities.

Mr K. Beurle, Dr A.R. Engel and Mr A. Bewick for their diligent assistance in the laboratory experiments and balloon test flight of the rotation modulation collimator (Chapter 2).

Mr A.J. Evans and Dr A.R. Engel for their information of the Ariel V satellite, of the IC hard X-ray detector on board, and of the conventional data analysis procedures (Chapter 3).

Mr A.J. Evans for his provision of references to the subject matter of Chapter 4.

Mr A.J. Evans for his collaboration in an attempt to resolve the difficulties associated with quantum cyclotron line formation (Chapter 5).

CHAPTER 1

INTRODUCTION TO X-RAY ASTRONOMY

1.1 Early History

Discussions and hints concerning the possible existence of high energy photon fluxes from celestial objects other than the sun date back as early as 1958. At that time the general opinion was that while the Sun provided at Earth an X-ray flux of 10^6 photons cm^{-2} s^{-1}, the flux from possible stellar objects would be $\lesssim 10^{-3}$ cm^{-2} s^{-1}, a value far too small to be detected without the development of sophisticated telescopes. In fact, the discovery of the first X-ray source (Giacconi et al 1962) was made as a result of a rocket flight, the primary intention of which was on the detection of lunar fluorescent radiation.

The rocket payload consisted of 3 Geiger counters (each of effective area ~ 10 cm^2) equipped with anticoincidence plastic scintillators to suppress cosmic rays charged particles background. During the flight a large peak in counting rate was found in the south azimuthal direction, which corresponded to a source emitting at a rate 10^7 - 10^8 times greater than the sun if the source was a nearby star. Subsequent rocket flights confirmed the discovery as a strong isolated source was identified in the Galactic Centre (Scorpio) region. In 1964 the modulation collimator technique (Chapter 2) gave the position of the source to within 30' and revealed that its size is < 7' (Oda et al 1965). The source was also identified in the optical region as a blue star-like object of 13th magnitude by Tokyo and Palomar Observatories. While refined observations of Sco X-1 were being made a source in the vicinity of the Crab Nebula

was also detected, first by the 1963 rocket flight of the Naval Research Laboratory (Bowyer et al 1964*a*).

Among the subsequent large number of rocket and balloon experiments it appears indisputable that the next major step in X-ray Astronomy occurred with the launch of the UHURU (SAS A) in December 1970 (Giacconi et al 1974). UHURU is the first satellite devoted entirely to X-ray Astronomy. The principle aim was an all sky survey of X-ray sources, to provide first estimates of intensities and spectral parameters. Subsequent X-ray experiments performed on board OSO-7, OAO Copernicus, Vela satellites and a few others, all attempted to extend/refine UHURU results. As most of these are scanning experiments, suitable for overall survey, observations involving high positional and spectral resolution were not extensively carried out until the launch of Ariel V in 1974.

1.2 The Ariel V Satellite with Special Reference to Experiment F

The satellite is spin stabilised and carries two scanning and four pointing experiments. One of the scanning experiments is specifically concerned with survey work (Experiment B) and the other carries out an all-sky monitoring of sources to detect sudden changes in flux (Experiment G). Three of the pointing experiments are designed to measure spectra and position of sources with higher sensitivity than UHURU, in the range 1 keV to 1 MeV (Experiments A, C and F), while the fourth pointing experiment is more speculative and aims to measure or set limits on polarisation and line emission in the X-ray flux from sources (experiment D).

Experiment F, designed and built at Imperial College, measures spectra of sources from 30 keV to 1 MeV. During its operation in 'Normal Mode' the energy range is divided into 15 logarithmically spaced energy

channels. This mode of observation does not provide information of rapid time development in the spectra of certain X-ray sources, such as pulsars or black holes, because of the long integration period required to obtain a signal of statistical significance. Thus, a sensitivity of 10^{-3} photons cm^{-2} keV^{-1} s^{-1} at 40 keV is attainable in a minimum of two days. However, experiment F, together with experiments C and D can also operate in a 'Pulsar Mode' in which X-ray counts are stored in one of sixteen phase channels depending on the photon arrival time. These channels cycle at the pulsar frequency. Each of the three experiments operate with a single energy bandwidth, but in different parts of the spectrum, so they can be combined to give some spectral information. Chapter 3 describes a recent (1979) observation of the binary X-ray pulsar 4U0900-40 (Vela X-1) by Experiment F in its 'Normal' mode.

1.3 Nature and Identification of X-ray Sources

The UHURU satellite surveyed 85% of the sky to a sensitivity of 2×10^{-10} erg cm^{-2} s^{-1} or better in the 2-6 keV range. The results are shown in the source density N(S) versus source strength S plot (Fig.1.1). Two populations are clearly distinguished, the first one includes all sources outside 20° of the galactic plane, and $N(S) \propto S^{-1.5}$. This seems to indicate that we are here seeing galactic as well as extra-galactic phenomena (if we assume a uniform distribution of stars within the galaxy and a uniform distribution of galaxies within the universe, then $N(S) \propto r^3$ and $S \propto \frac{1}{r^2}$ so that $N(S) \propto S^{-1.5}$). In fact, the extended 3U catalogue, published in 1974 (Giacconi et al 1974) indicates that among the 161 X-ray sources, ~20 were identified* as of extra-galactic origin. The second population includes all sources within 20° of the

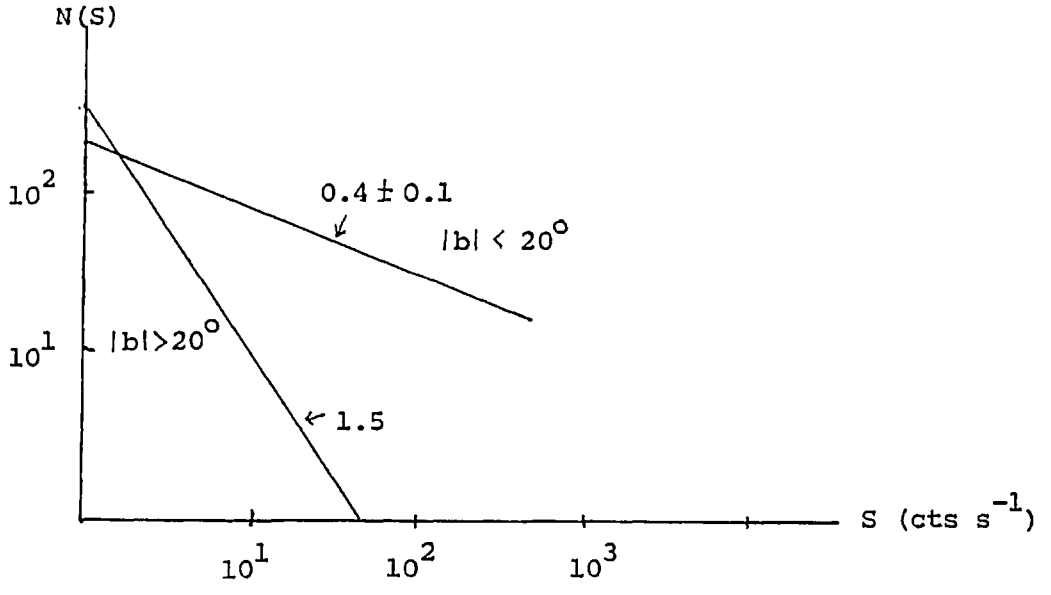


Fig 1.1 The integral number of sources of intensity greater than S is plotted as a function of intensity S. The sources are divided into two groups: one is galactic latitude $|b| < 20^\circ$, the other is galactic latitude $|b| > 20^\circ$.

---

* Work on the identification of galactic and extragalactic X-ray sources with optical, radio and infra-red objectshas been done almost immediately after the discovery of Sco X-1. The 'identification' of any given X-ray source is often a gradual and subjective process. First of all,X-ray positions almost always contain a larger error box than the corresponding radio or optical positions (this is due to the high frequency of the radiation and the low count rate actually detected). Thus an optical counterpart may be first suggested on the basis of rather tenuous evidence. It may thenbecome more generally accepted as more precise X-ray measurements become

galactic plane, and $N(S) \propto C S^{-0.4}$. Here there is a striking difference between the observed slope and the slope of -1 expected for a uniform distribution of equal luminosity sources. The much flatter observed slope indicates that we are seeing essentially all of the bright sources in our galaxy and that there is a spread in intrinsic luminosities.

1.4 Galactic X-ray Sources

Most galactic and extra-galactic X-ray sources have been identified as one of the following categories.

- Galactic
  - Supernova Remnants
  - Compact X-ray Sources
- Extragalactic
  - Normal Galaxies
  - Active Galaxies
  - Seyfert Galaxies
  - Quasi-stellar objects.

We will begin by a discussion of the two common classes of galactic phenomena.

---

available and as the peculiar nature of the optical object becomes more evident. In some cases, identical periodicities or simultaneous flaring at X-ray and optical wavelengths establish the identification with certainty (see later in chapter).

1.4.1 Supernova Remnants

Supernova Remnants have an extended emission region which varies between 0.1- a few parsecs. The center of the emission sometimes contain an X-ray pulsar (e.g. Crab and Vela X). In the case of the Crab, pulsations of the same period and phase were also observed in the radio and the optical. The period of the pulsar was observed to be increasing at a rate which implies a rotational kinetic energy loss of 2×10^{38} erg s^{-1}, which is the same as the total luminosity observed from the nebula. The energy loss can take the form of magnetic dipole radiation or the acceleration of charged particles (by the rotating magnetic field) from the equatorial to the polar region near the surface of the star. In the latter case the particles stream out into the nebula and produce the extended source of radio, optical and X-ray emission. Such particles may also form a good candidate for the origin of cosmic rays.

However, recently Ricker et al (Ricker et al 1975) confirmed at higher energies the observation of Bowyer et al (Bowyer 1964b) of a large angular extent for the X-ray source in the Crab. The exact relation between the accelerated particles and the pulsar has become far less clear since the recent observations revealed a displacement between the X-ray source and the pulsar. This unresolved problem become one of the chief motivations for the extension of the modulation collimator technique (by far among the best methods in precise X-ray positioning) to Hard X-ray (50-100keV) energies.

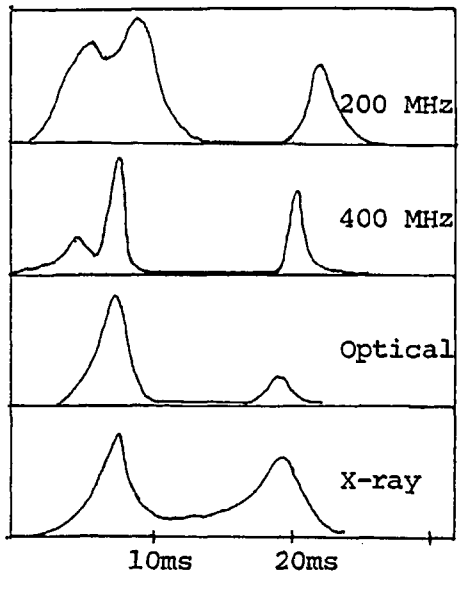


Fig 1.2 Pulsed emission from the Crab Pulsar in the X-ray, optical and radio spectrum.

1.4.2 Compact X-ray Sources

Sources not associated with supernova remnants generally fall into a second category, characterised by rapid variability (~seconds or less), large luminosity ($\sim 10^{36}$-10^{38} erg s^{-1}) and hard spectra (~ 10-100 keV) - all of which suggest that they are related to gravitationally collapsed objects (i.e.neutron star or black hole). The fact that the accretion of matter from a nearby star on to the compact object can release energy detectable in the X-ray range of frequencies was recognized as early as 1964 (Hayakawa et al 1964). The search for the presence of binary companions in the compact X-ray sources then began, but it was not until 1971 that the binary nature of the source Cen X-3 was unambiguously established by Uhuru observations(Giacconi et al 1971). Cen X-3 was found to be a pulsar of period 4.8 seconds eclipsed every 2.087 days by an unseen (X-ray dark)companion. The source was subsequently identified with a 13th magnitude object (Cen-3) having an (optical) binary period of 2.087 days (Giacconi et at 1974). Subsequently the binary nature of more and more X-ray sources were discovered. We describe below a few important cases:

(a) Hercules X-1 The pulsating source in Hercules (2U1705+34) has an (unusually short) 1.24 seconds period and a 1.700 day occultation cycle (Tananbaum et al 1972). Observations of long term variability revealed that Her X-1 also possesses a 35 day on-off cycle, which is interpreted as due to periodic changes in the accretion rate. The source was identified with the 15-13 magnitude star HZ-Hercules(Tananbaum et al 1972) which has the same binary period of 1.7 days in the optical.

(b) Cygnus X-1 With the help of the relatively good location (Rappaport et al 1971) of Cyg X-1 a radio source was discovered (Braes and Miley 1971), the precise location (1") of which led to the optical identification (Webster and Murdin 1972) of Cyg X-1 as a 5.6 day spectroscopic binary. However, earlier search for a similar 5.6 day effect in the X-ray emission was not successful. Subsequent observations by Uhuru revealed a remarkable flaring of the source in the 2-6 keV and (less so) in the 6-20 keV region. This coincided (in time) with the appearance of a weak radio source in theCyg X-1 region. The correlated behaviour reassured scientists of the correctness of the radio, and hence optical, identification. The search for binary cycles for Cyg X-1 thus continued. In 1974-75 a 5.6 day modulation synchronized with HDE 226868 was observed over a 6 month accumulation of the Ariel V All Sky Monitor (ASM) data. In April, 1975 the source underwent flaring and a similar 5.6 day modulation was reported in the 'High State' data (Holt et al 1976).

(c) Cygnus X-3 A 9 day observation of Cyg X-3 by Uhuru revealed the presence of a 4.8 hour periodicity in the 2-6 keV emission (Parsignault et al 1972). The Uhuru data also indicated flaring of the object in the very beginning of September 1972, which corresponded to the same period when a high level activity was observed from the radio counterpart (Braes and Miley 1972). This correlation appears to support the radio identification of Cyg X-3. One year later Becklin et al (Becklin et al 1973) reported coordinated X-ray and Infrared observations - the X-ray and IR fluxes vary in phase with a 4.8 hour period. This establishes the IR identification of Cyg X-3 and, through the positional

coincidence (2") of the IR and the radio source, also the radio identification.

1.5 Extra-galactic X-ray Sources

Extra-galactic X-ray Sources were discovered in the 1960's when the sources in Virgo and Centaurus A were identified with nearby active galaxies that are also strong radio emitters. Subsequently the Uhuru survey revealed the existence of more than 60 X-ray sources at high galactic latitudes, about half of which are identified with extra-galactic objects.

1.5.1 Normal Galaxies

The nearest galaxies outside our own, the Magellanic Clouds - are identified as X-ray sources. The Small Magellanic Cloud contains a binary stellar source with luminosity (2-6 keV) 1.3×10^{38} erg s^{-1}. The Large Magellanic Cloud contains four discrete X-ray sources, and has a total luminosity (2-7 keV) 3.8×10^{38} erg s^{-1}. It is unclear whether all of these objects are binary systems.

1.5.2 Active Galaxies

Several active galaxies are known to be strong emitters in both the X-ray and radio frequencies (e.g. NGC1275, 3C390.3, 3C273). However, the majority of extra-galactic X-ray sources are, at most, weak radio emitters. In fact, only one object, Cen A, can a physical relation between the X-ray and radio emission be established. Cen A has an extended double radio source lying approximately north and south of the giant elliptical galaxy NGC5128. There are also two inner lobes centred on the optical galaxy. The position of the X-ray source, as given by the 3U Catalogue (Giacconi et al 1974) coincides with that of the optical

galaxy with an error box of area 45 sq. min. Recently X-radiation has also been detected from the large radio lobes (Cooke et al 1978).

1.5.3 Seyfert Galaxies

In recent years the number of identified Type 1 Seyfert Galaxies has increased dramatically. At least 25 Seyferts are now reliably identified with 2A, Uhuru or SAS-3 X-ray sources. Seyfert Galaxies have an X-ray luminosity (2-10 keV) of 10^{42}-10^{45} erg s^{-1}, and a typical time variability$\sim$month (although NGC4151 is known to 'flare' over a period of days and possibly 12 mins., see Tanabaum et al 1978). These, together with detailed studies of possible correlations of the X-ray with optical, infra-red and radio emissions (Elvis et al 1978) strongly suggest that the X-rays originate in the dense inner region (extent $\sim$ 0.1 pc) of a Type 1 Seyfert Galaxy. The size and spectrum of 2U1207+39 (NGC 4151) have been obtained from Uhuru data (Kellogg 1973) and gives an upper limit of 15' diameter. This corresponds to$\sim$50 kpc diameter so that the size of the X-emitting region is not greater than that of the galaxy. More precise measurement of source position and extent is clearly necessary.

1.5.4 Quasi-Stellar Objects

3C273 was the only certain QSO identified as an X-ray source(see Bowyer et al 1970, Kellogg et al 1971) until recently, when a refined SAS-3 measurement of the former Ariel V position of the source 2A2251-179 led to its identification with a bright (B$\sim$16) quasi-stellar object MR 2251-178 (Ricker et al 1978). This object, at a redshift of .068, has an X-ray luminosity (2-10 keV) of 5×10^{44} - 1.6×10^{45} erg s^{-1}. The power of the modulation collimator technique in X-ray positioning

is seen most clearly here as we compare the SAS-3 Mod Col error box (shown in Fig 1.3 as circle) for 2A2251-179 with that of Ariel V (shown as square in Fig. 1.3).

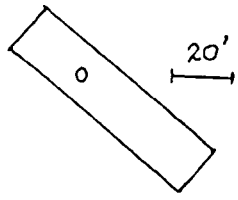


Fig 1.3

1.6 Conclusion

From the above discussion it is clear that the current research on the subject of Extra-galactic X-ray Sources is still in a rather primitive stage, but can be significantly enhanced by more precise positional measurements of such objects. This does not only lead to identifications of sources, but also provides information of source sizes and extent of tails, lobes etc. which is invaluable towards the development of correct models for the systems.

We have already seen in section 1.5.4 how the technique of rotation modulation collimator in the low energy (2-10 keV) region provided significant improvement in positional measurements. Parallel to this is the development of high resolution focussing optics with imaging detectors in the Einstein (HEAO 2) Observatory (Giacconi et al 1979). This technique is applicable in a similar energy range (0.2-4 keV). Apart from the apparent discrepancies in the Hard X-ray mapping of the Crab (section 1.4.1) we enlist below additional reasons for the necessity of precise attitude data at higher energies - 10-100 keV - a regime in which only the modulation collimator method remains applicable (by the use of a suitable Hard X-ray absorbing material for collimator manufacture).

(a) Mapping of hard tails of extended sources (e.g. Perseus Cluster). Most recent HEAO-1 observations of the Perseus Cluster reveals that

the spectrum exhibits a previously unknown hard (>25 keV) component (Primini et al 1980). Precise positioning was not possible as slat collimators were used on board.

(b) Resolution of Galactic Centre confusion. The 2° region in the vicinity of the Galactic Centre contains an assortment of highly variable X-ray sources. It is known that there are at least seven sources, three of which have been measured very precisely by the modulation collimators on board Ariel V and SAS-3 satellites. The others (GX359+2 and some bursters) were well above the Uhuru and SAS-3 thresholds.

(c) Precise location of X- and Gamma ray bursts. Nishimura 1975 first demonstrated that source location is still possible if $\nu > \nu_b$ where ν is the frequency of the rotating collimator (see Chapter 2) and ν_b is the frequency of the burst. Three X-ray burst sources have been identified with faint ($m_B \sim 18$) blue stars using the SAS-3 modulation collimator system (see McClintock et al 1977, Davidsen 1975). The technique should be extended to hard X- and soft gamma ray bursts.

The construction, laboratory experimentation and balloon test flight of a tungsten modulation collimator designed to meet the above demands will be discussed in Chapter 2.

CHAPTER 2

THE MODULATION COLLIMATOR TECHNIQUE IN OBSERVATIONAL X-RAY ASTRONOMY

2.1 Introduction to the Modulation Collimator

Cosmic X-ray photons are detected through the observable events which they produce upon interaction with suitable matter. This fact, together with the superior time resolution which can be obtained and the low flux rates from even the strongest sources in the sky, implies that single photon counting is inevitable. Moreover there is present above the atmosphere (all experiments have to be at high altitudes due to the strong attenuation of the atmosphere) a significant background of high energy events against which one must detect discrete sources. Most physically determined quantities are limited by count statistics.

Slat collimators of every imaginable type have been used to restrict the viewing direction of the detectors. The smallest view angles that have been achieved is about $\frac{1}{2}°$. The basic design (Discussed in some detail by Giacconi et al 1974) has to meet the following requirements :

1. High angular resolution. This demands adequate wall thickness, otherwise the collimation will be lost at high energy.
2. Wide aperture. This would mean a minimal of wall thickness.

Such apparently conflicting demands are resolved in a modulation collimator (Oda 1965) by the use of planes of wire grids. The wide aperture of the collimator reduces the constraint of an accurate pointing of the device to the source. Moreover, when the source is scanned, a large brightness is achieved because it is seen with numerous repetition.

The bigrid collimator (Fig 2.1) consists of two wire grids in

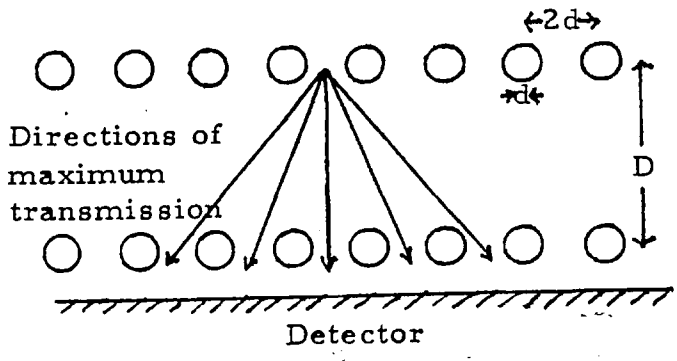


FIG 2.1

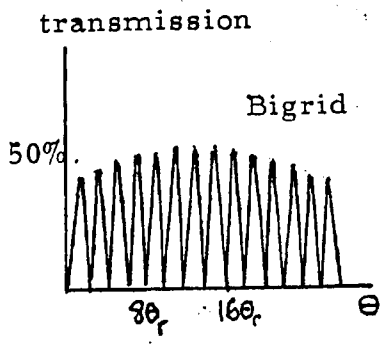


FIG 2.2

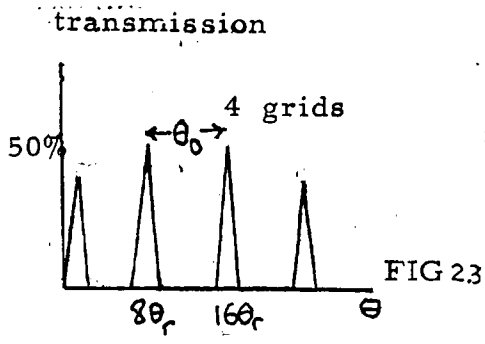
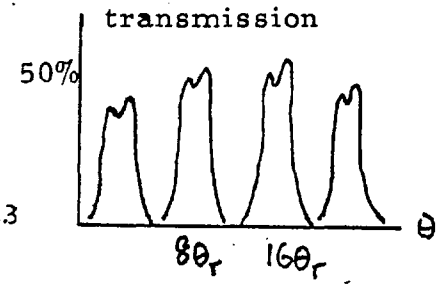


FIG 2.3



8 grids
Finite source
size

FIG 2.4

front of an X-ray sensitive detector. Each grid has parallel wires of diameter d and spacing 2d. The net angular response of the ideal bigrid device to X-rays is cyclic and triangular in shape with peak transmission of 50% (Fig 2.2). The directions of such maxima are planes in 3-dimensional space. The response angle is defined as the FWHM $\theta_r = \frac{d}{D}$ where D is the distance between the grids. Wire planes with 0.1 mm wire on 0.1 mm centres have been used. With D $\sim$ 1 m fine angular resolution $\theta_r < 1'$ can be achieved.

The bigrid system determines the angular size of an X-ray source with size $< 2\theta_r$ and clearly distinguishes sizes above and below this range.

Furthermore, it is effective for sources at large angles to its axis. For extended sources of size > $2\theta_r$ and for regions of high source density when more than one source is in the field of view, a multigrid collimator is developed. Here the addition of wire planes at intermediate spacing (each new plane placed midway between the closest pair) has the effect of removing alternate transmission bands and one is left with individual bands of the intrinsic width $\frac{d}{D}$ separated by an angle $2^{k-1}\frac{d}{D}$ (Fig2.3)where k is the total number of planes. This style collimator can be used effectively for studying the structure of extended sources up to a size $2^{k-1}\frac{d}{D}$ with a resolution $\frac{d}{D}$ (Fig.2·4).It also reduces the probability that two or more sources will simultaneously lie within the field of view.

In both the bigrid and multigrid collimators the planes of maximum transmission allows for multiple transits of a single source during a single scan across the region with the resulting accumulation of statistics. However, a problem introduced with such a device is that a given sighting of an extended source easily results in a multiplicity of positions, essentially a series of lines in the sky. To reduce position ambiguity a rotating modulation collimator (Mertz 1967) is used. Consider the case of a bigrid collimator rotated around the sky. Fig 2.5shows a source at an angle $\theta = \theta_o$ from the centre of the field of view, and at an azimuthal angle $\phi = \phi_o$ w.r.t. an arbitrary reference. Lines on the sky correspond to maximum (solid) and minimum (broken) transmission through the collimator. The intensity varies

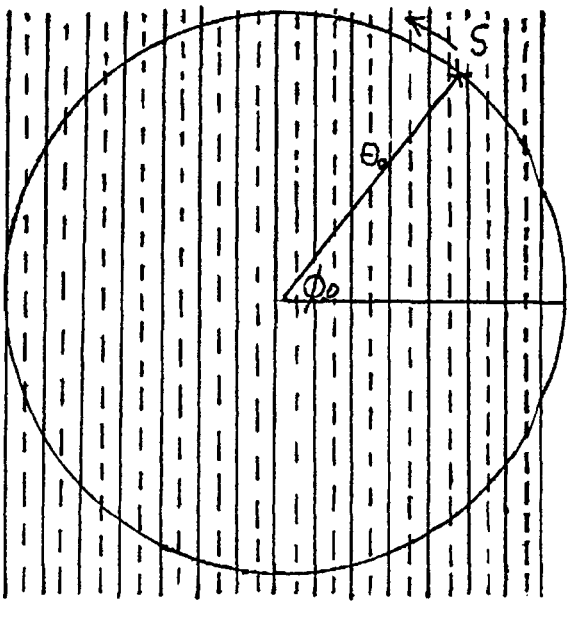


FIG 2.5

as a simple triangular function of the parameter $x = \theta_o \cos(\phi-\phi_o)$ from which information about θ_o and ϕ_o can be found by the technique of fast Fourier analysis (Schnopper et al 1968) or cross-correlation (Schnopper 1970).*

RMC measurements of galactic X-ray sources were performed in the satellites Ariel V (Cruise et al 1975), SAS-3 (Schnopper et al 1976) and HEAO-1 (Gursky et al 1978). All observations were made in the low energy region (typically 1-10 keV photons) using proportional counters with sizes of a few 100 cm^2. The present objective is to extend the technique to hard X-rays (10-100 keV) region. Although not the ideal material for accurate wire collimator manufacture, the element tungsten was still employed. This is because the absorption coefficient α of tungsten (defined as $I = I_o(1-e^{-\alpha d})$ where I_o is the incident intensity, I is the transmitted intensity and d is the length of material traversed) varies from 30 cm^{-1} to 4 x 10^3 cm^{-1} in the range 10-100 keV, so that a typical wire thickness of 1 mm is sufficient for the purpose of removing hard X-rays.

2.2 Modulation Collimator - Construction

The basic design consists of two planes of parallel wires, 1 mm diameter and 1 mm separation. The distance between the planes is 4.9 cm. The theoretical value of the FWHM is thus

$$\frac{1 \text{ mm}}{4.9 \text{ cm}} = 1°10'$$

Tungsten wires (99.97% purity) have been used. Each was

---

* In addition, Nishimura (1975) suggested that source location is still possible in the case when the source is transient (e.g. gamma burst) provided that the collimator is rotated with a frequency $\nu \gtrsim \nu_b$ where ν_b is the frequency of the burst.

stretched by a force of 1.5 kN which took the wire slightly beyond its elastic limit. The wires were then mounted in two planes on a steel frame. To maintain a constant separation (1 mm) between the wires throughout their lengths, the wires were slightly stretched, hexagonal screws being used to maintain the tension. Aluminium spacers were then fixed (with slight pressure on the wires) on each plane at the positions shown (Fig. 2.6).

2.3 Detector and Electronics Devices

The scintillation crystal was of NaI (Tl), area 200 cm^2 and thickness 2 mm. The detection efficiency (i.e. the probability that the crystal scintillates, given that a photon has interacted) as a function of photon energy is shown in Fig 2.7. One surface of the crystal is protected from the outside by a thin aluminium plate and the other surface is coupled to two 3" EMI 9758B

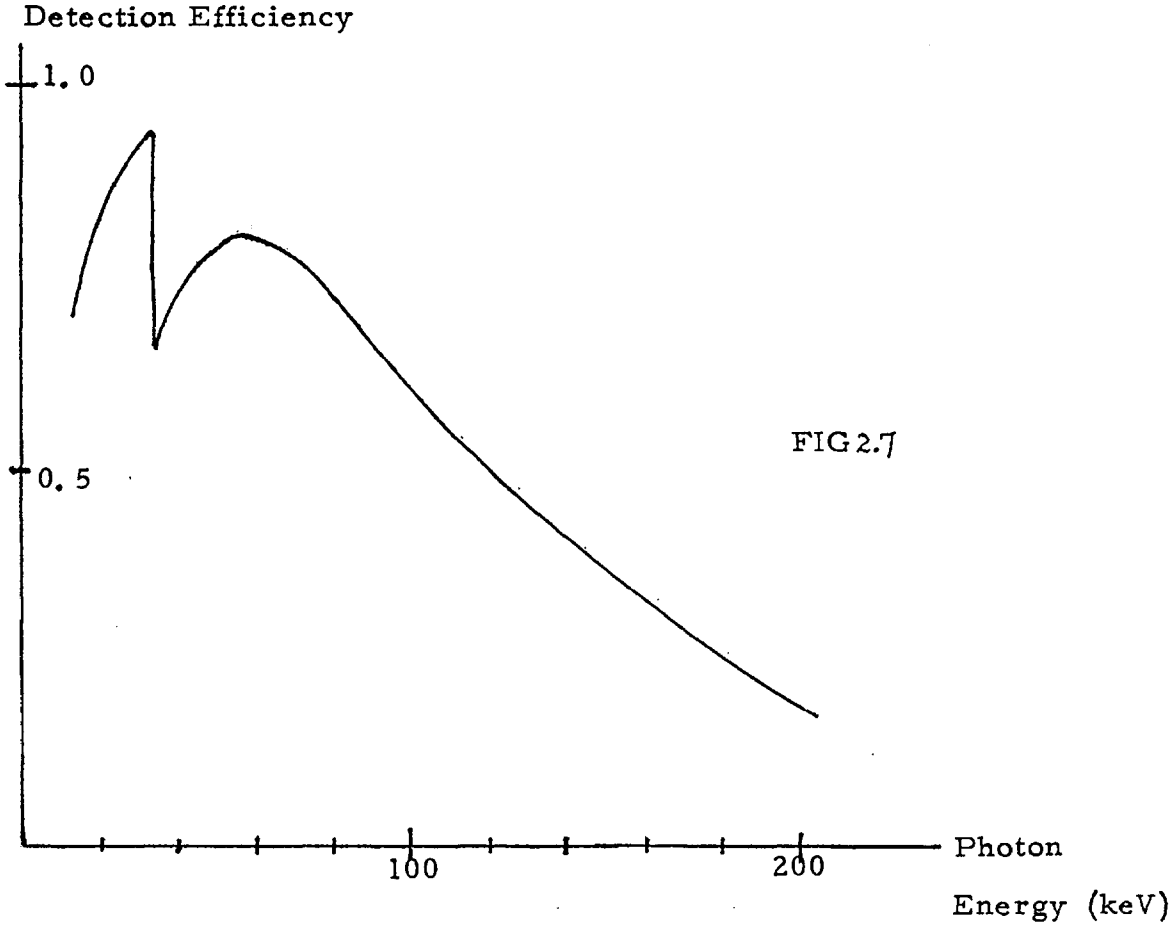


FIG 2.7

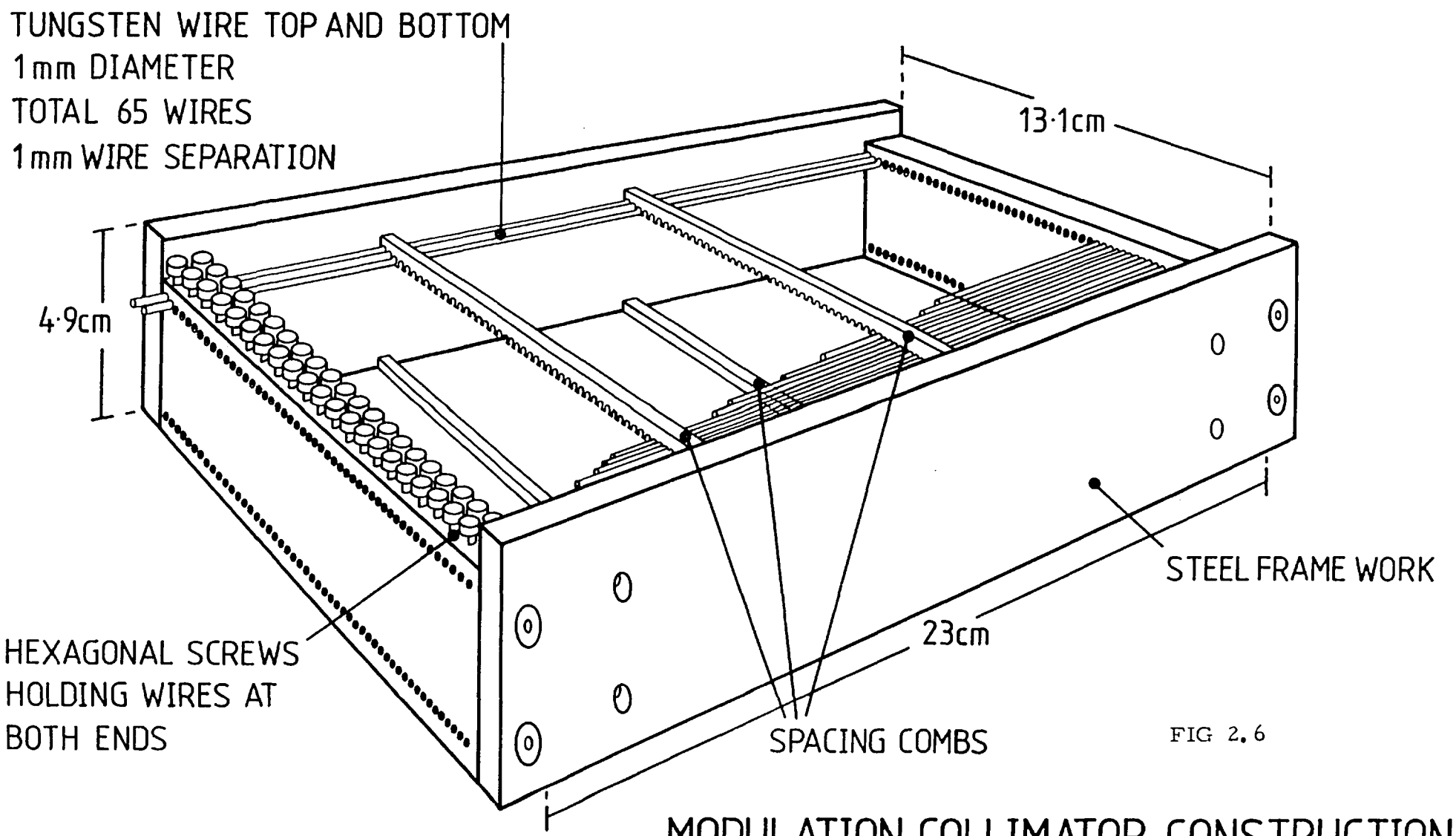


FIG 2.6

MODULATION COLLIMATOR CONSTRUCTION

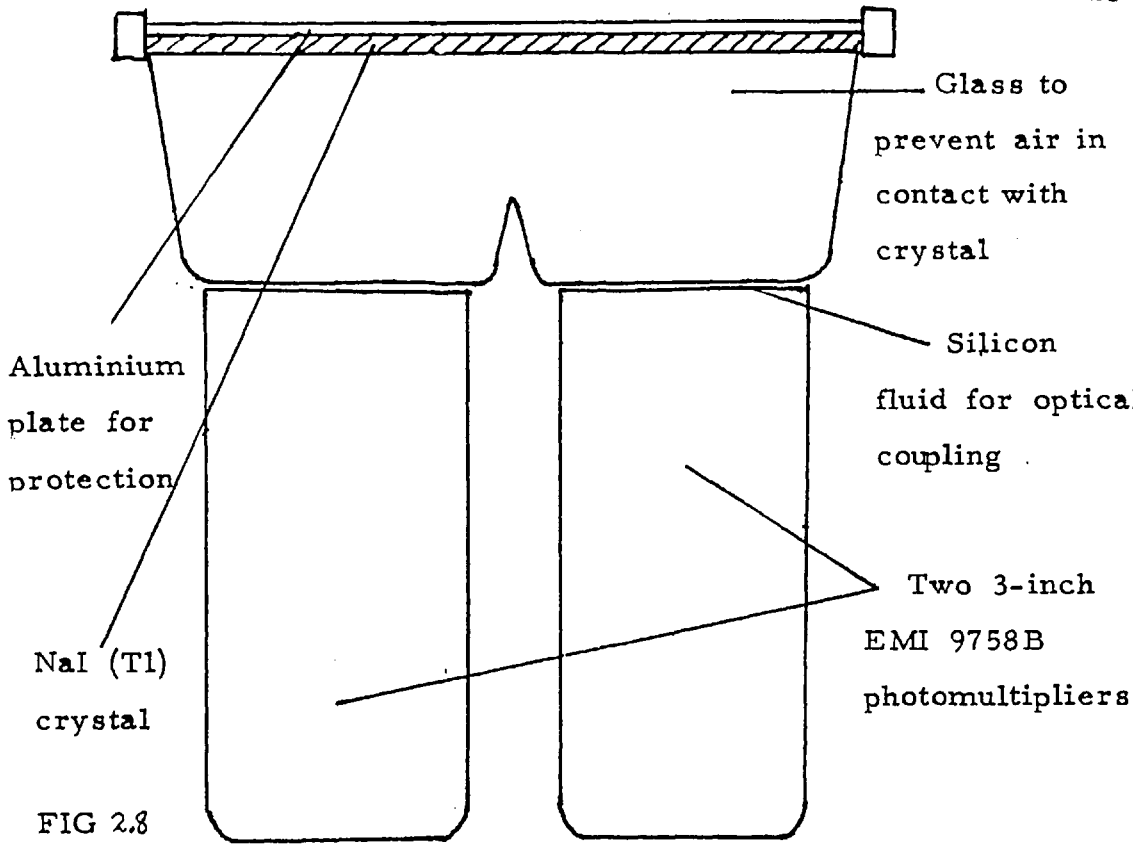

Glass to prevent air in contact with crystal
Silicon fluid for optical coupling
Aluminium plate for protection
Two 3-inch EMI 9758B photomultipliers
NaI (Tl) crystal

FIG 2.8

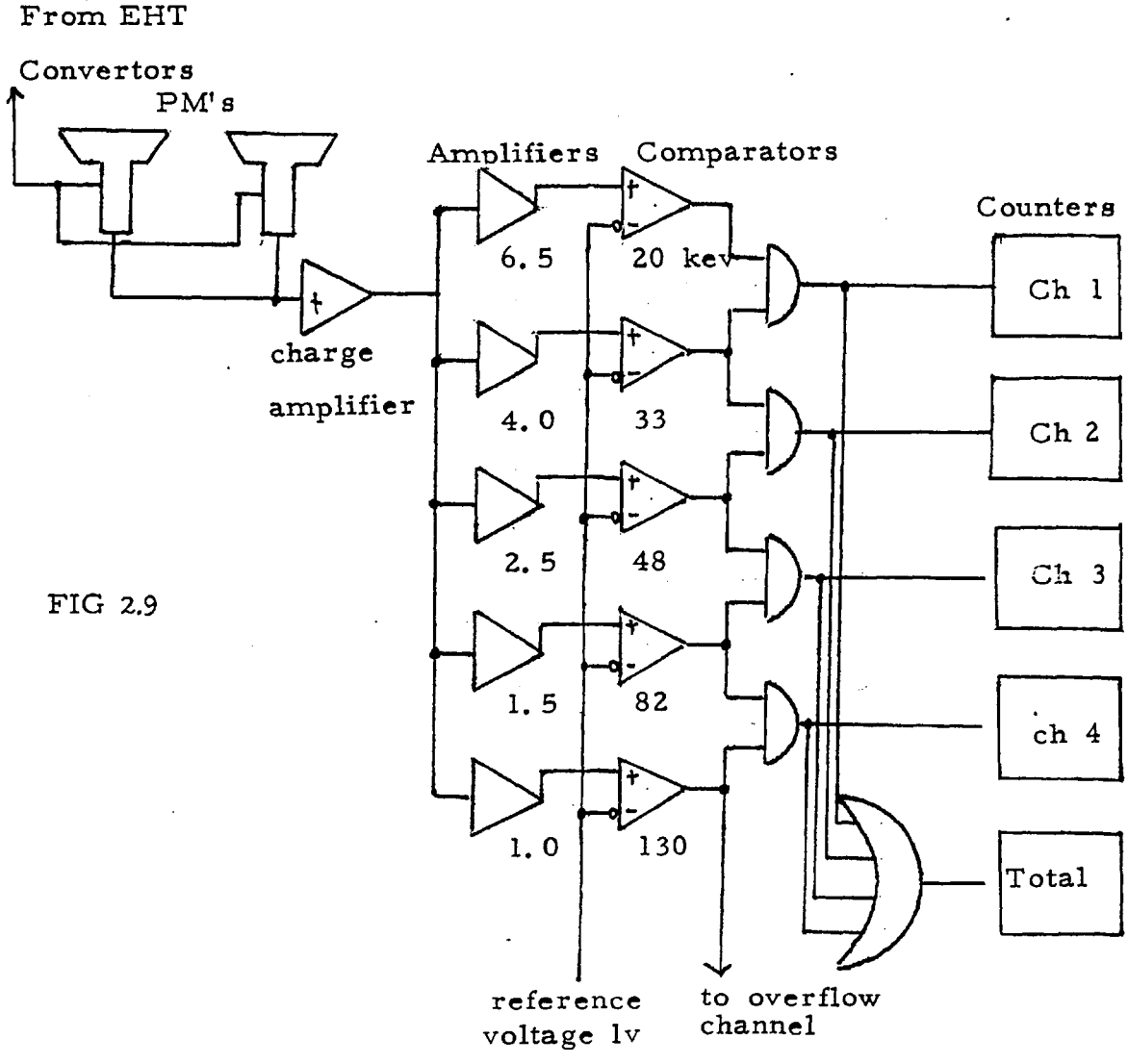

From EHT
Convertors
PM's
Amplifiers
Comparators
Counters
6.5
20 kev
Ch 1
charge amplifier
4.0
33
Ch 2
2.5
48
Ch 3
1.5
82
ch 4
1.0
130
Total
reference voltage 1v
to overflow channel

FIG 2.9

photomultipliers (Fig 2.8). The output from the two photomultipliers is then connected via a charge amplifier to a logical circuit and counters unit (Fig 2.9) such that whenever a photon has energy which falls within the domain of one of the following six channels (Table 2.1), a number is registered in the corresponding counter.

TABLE 2.1

Channel 1	20 - 33 keV
Channel 2	33 - 48 keV
Channel 3	48 - 82 keV
Channel 4	82 - 130 keV
Channel 5	> 130 keV (overflow)
Channel 6	Total

2.4 Tests Performed in the Laboratory

Before the balloon test flight in August 1979 at Mildura ground based experiments were conducted to assess as much as possible the performance of the modulation collimator. The X-ray source Cobalt-57 was used. It has two principle emission energies at 122 and 136 keV of

which the former is dominant in intensity. The entire experimental set up is shown in Fig 2.10.A laser was used to align the collimated source with the detector. With the set up below the following experiments were conducted.

2.4.1 Depth of Modulation and Angular Response

Initially the collimator was removed and counts were taken for

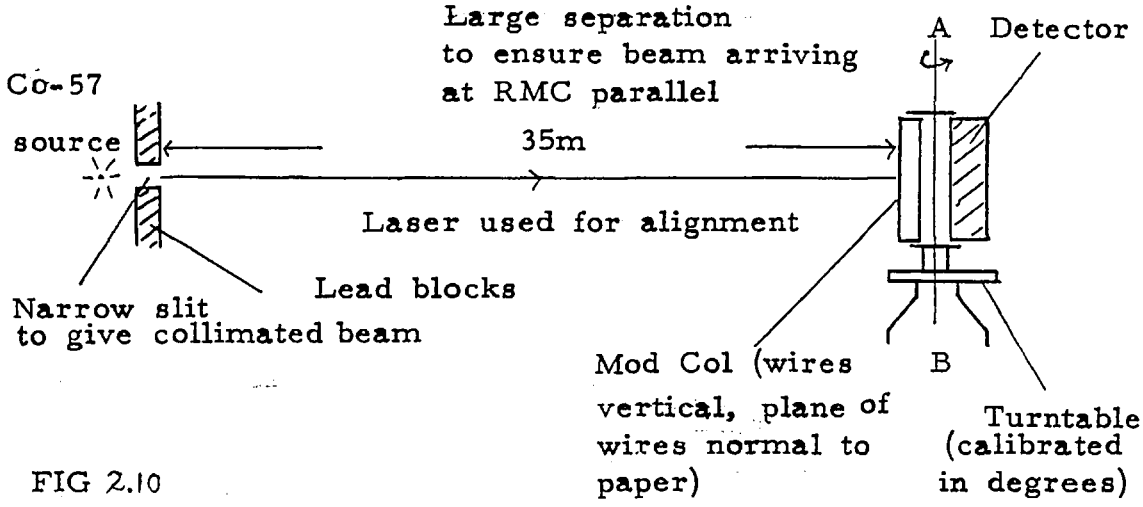


FIG 2.10

the source (1) and the background (2) (400 sec. each). As the background consists of X-rays from the atmosphere plus scattered source X-rays, the background counting was done with a lead obstacle placed at approximately 9 m from the source, rather than with the source removed. The difference (1)-(2) then gives the uncollimated source signal.

The modulation collimator was then mounted with the angle between the plane of the wires and the source

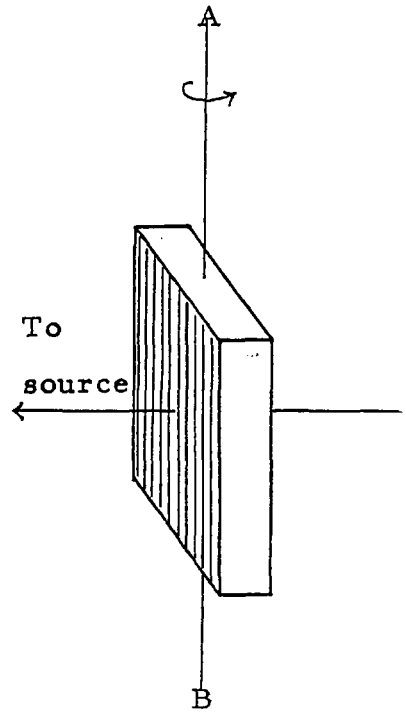


FIG2.11 Enlarged view of the positioning of Mod Col

direction $\theta = \frac{\pi}{2}$. A further background reading (3) was taken, this time for as long as 3000 sec. in order to improve the accuracy of the entire experiment. The obstacle was then removed and small rotations $\theta = \frac{\pi}{2}+\delta\theta$ about the axis AB was performed (see Figs.2.10&2.11) with the aid of a turntable calibrated in degrees. 400 seconds counts were taken for every $\delta\theta \sim 15'$ rotation. From each of these counts the background (3) was subtracted and the resulting source signals were then plotted as a function of the angle of rotation (Fig 2.12).The errors attached were obtained assuming poisson statistics. The separation between consecutive maximum and minimum positions agrees well with the theoretical value of 1°10'.

The difference between the maximum and minimum counts can be expressed as a percentage of the uncollimated source count (1)-(2). The theoretical prediction of this percentage (from now on referred to as the depth of modulation) is, of course, 50%. The experimental estimate turned out to be 37.5 ± 2%. This apparent discrepancy can be accounted for by one or more of the following reasons :

1. Isotropic emission of secondary X-rays from tungsten by the processes of (i) fluorescence, (ii) compton scattering and (iii) electron bremsstrahlung.
2. Incomplete absorption of the primary X-rays by the wires. Approximately ≳95% of X-rays are absorbed by a 1 mm thickness of tungsten. However, the radiation does not traverse the full diameter of the wires in general cases.
3. The presence of irregularities in the wires.

These effects will be investigated in detail in the following two sections.

When the angle θ is substantially different from $\pi/2$ the depth

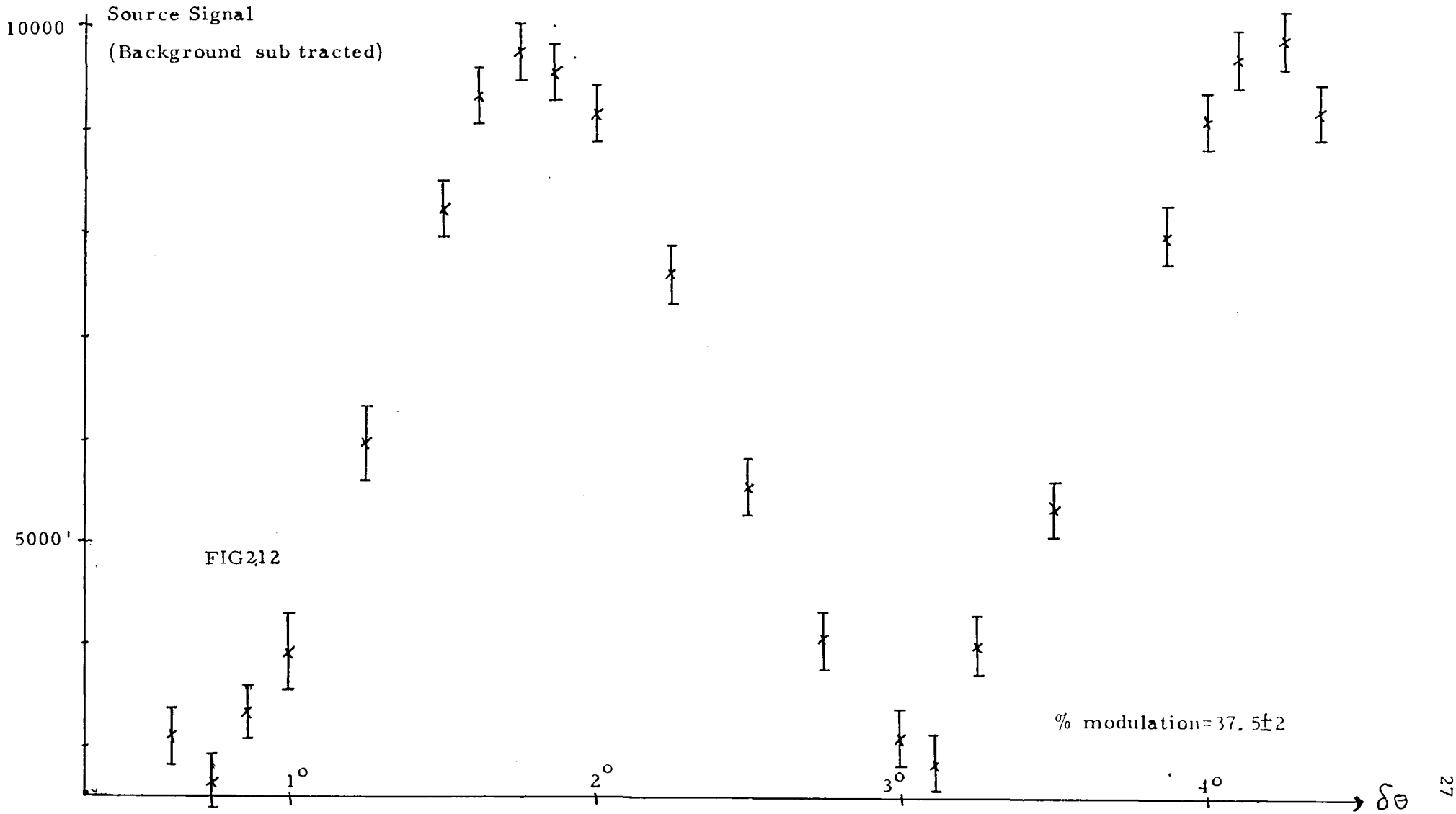

Source Signal
(Background sub tracted)
10000
5000
1°
2°
3°
4°
δθ
% modulation = 37.5±2

FIG 2.12

of modulation is expected to be suppressed by a cosine envelope - the effective area of the detector being the projected area normal to the source direction. To test this the same experiment was repeated for small rotations about an angle $\theta \neq \pi/2$. From the plot (Fig2.13) the depth of modulation was estimated to be 30 ± 5% and the angular half-width 1°3'. Both figures are indeed less than before.

2.4.2 The Effect of Tungsten Fluorescence on Modulation Properties

Photons of energies 122 and 136 keV interact with tungsten through the photo-electric effect (photo-ionization) and compton scattering. From tables the coefficients of such processes are, respectively, $\sim$ 50 cm^{-1} and 4 cm^{-1} at the above-mentioned energies. In photo-ionization, the minimum energy required (k-edge for tungsten) is 69.55 keV, the remaining energy, e.g. 122 - 69.55 = 50.05 keV, goes to the kinetic energy of the electron. In this case the electron can emit up to $\sim$ 50 keV photons by bremsstrahlung, and then up to $\sim$ 70 keV by transition to inner orbits, i.e. fluorescence (although in reality the emission lines are centred at 58 keV).

Turning now to compton scattering, the situation is rather different. Firstly, the process plays a considerably less important role than photo-ionization, as can be seen from the above-mentioned interaction coefficients. Secondly, the standard formula for the frequency of the scattered X-rays,

$$h\nu' = \frac{m}{h\nu(1-\cos\theta) + m} h\nu$$

gives the maximum and minimum possible values of $h\nu'$ (corresponding respectively to forward scattering $\cos\theta = 1$ and backward scattering $\cos\theta = -1$). In fact, for an incident radiation $h\nu$ = 122 keV we have

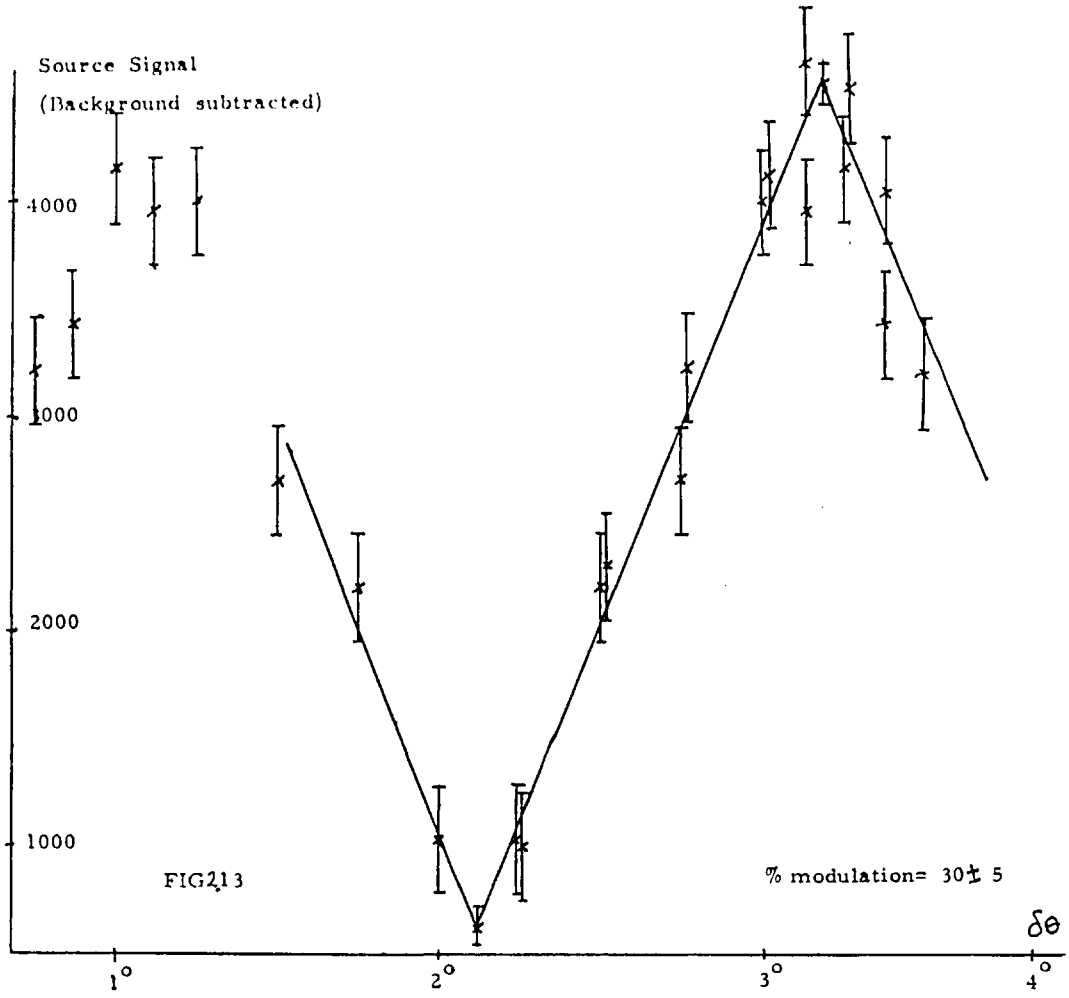


FIG2.13

% modulation= 30± 5

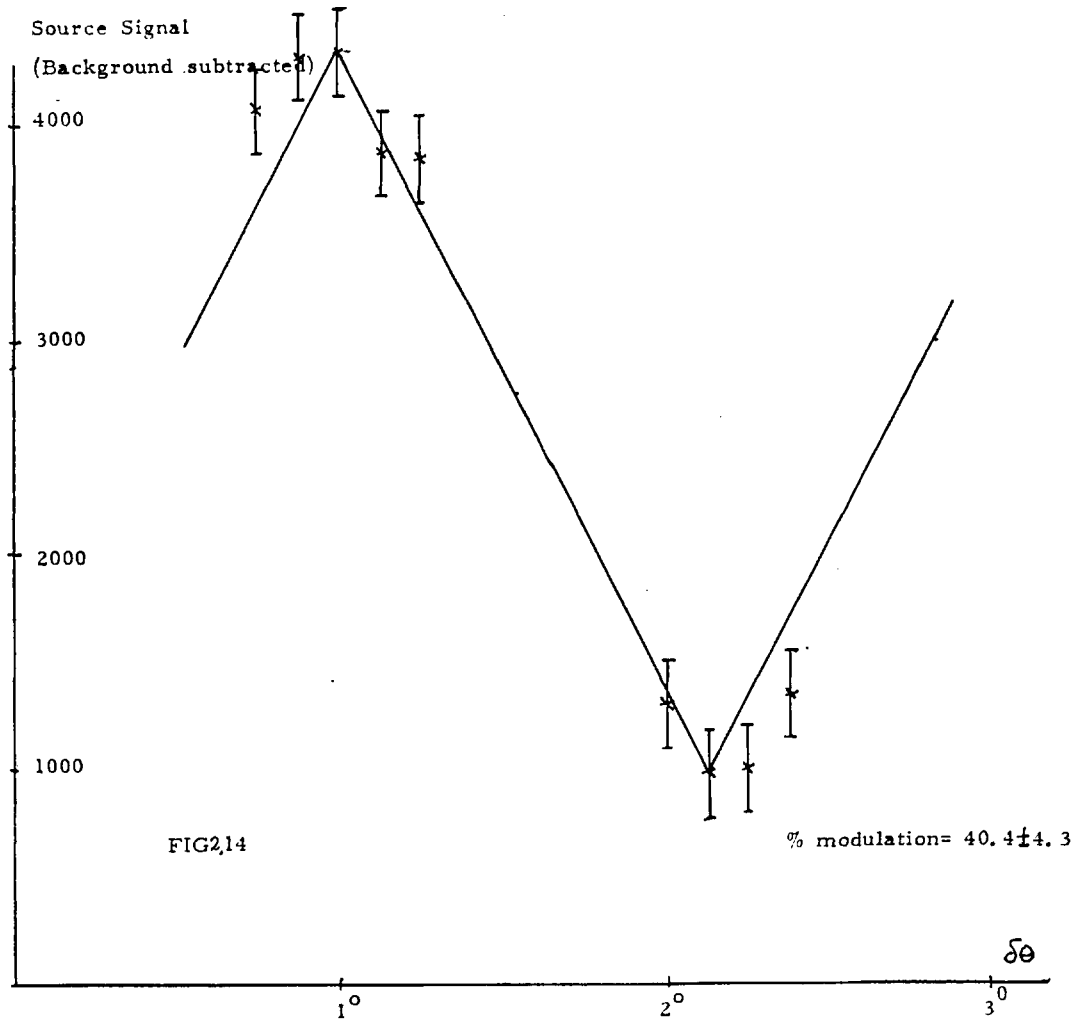


FIG2.14

% modulation= 40.4±4.3

$87.5 \lesssim h\nu' \lesssim 122$ keV, so that photons resulting from compton processes have energies considerably higher than those from photo-ionized electrons. The following experiment attempts to investigate the effects of the latter on the modulation properties. From the above discussion it is clear that a discriminator setting which excludes X-rays of energies $h\nu' \lesssim 65$ keV will serve the purpose. With this rearrangement the experiment was repeated as in 2.4.1, the initial position of the plane of the modulation collimator being normal to the source direction. All results were plotted in Fig. 2.14. The angular half-width was again 1°9' and the depth of modulation $40.4 \pm 4.3\%$. The conclusion is that the modulation properties are not significantly affected by the presence of tungsten fluorescence.

2.4.3 Laser Investigation of Modulation Properties and Angular Response

The effects of wire irregularities are studied by means of visible radiation. The entire set up is shown in Fig 2.15. Light from a laser was focussed and directed to a convex lens of wide aperture

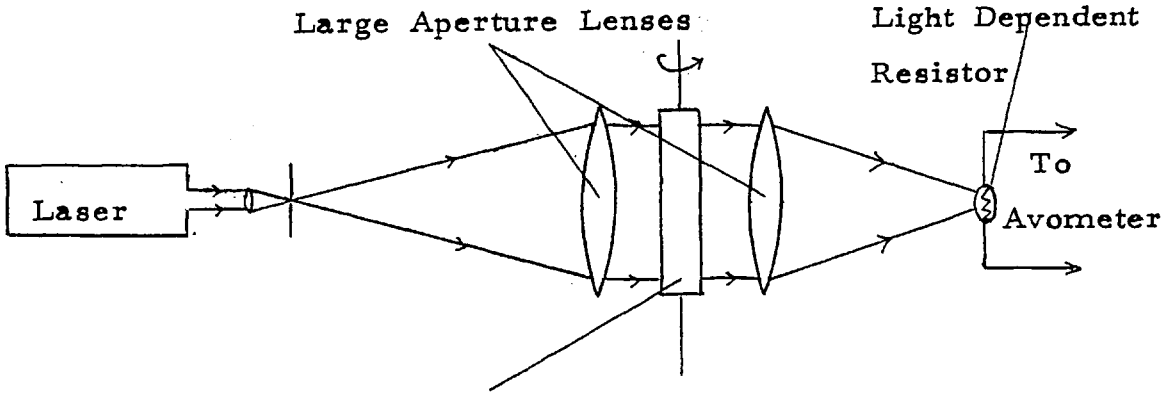


FIG 2.15

(approximately equal to the size of the collimator). The parallel light which emerges from the other side of the lens was then allowed to go through the two wire planes and then refocussed on to the surface of a light dependent resistor by a second lens of a similar aperture.

With the plane of the collimator initially normal to the source direction, the collimator was slowly rotated along the axis AB (Figs 2.10&2.11) with the aid of the turntable. The ohm-meter reading for the resistor moved across successive maxima and minima. A conversion graph gives the corresponding illumination. Using procedures similar to those outlined in previous experiments, the angular response was found to be 1°9' ± ½' and the depth of modulation 48%. Thus the irregularities of the wires do not account for the apparent deterioration of performance in the hard X-ray region. The remaining possibilities are (section 2.4.1) X-ray leakage through the tungsten wires and secondary emission by compton scattering. We showed earlier on (2.4.2) that the energy of the scattered photons falls in a range which has the energy of the primary (incident radiation) as the upper limit. This appears to provide an intrinsic limitation to the use of collimators at hard X-ray energies, where the cross-section for compton scattering no longer remains insignificant w.r.t. that of photo-ionization.

2.5 Modulation Collimator - Flight Configuration

Prior to the balloon test flight the modulation collimator has a coarse lead collimator (rectangular cross section) fixed on top to limit the field of view to 10°. An anticoincidence shield, consisting of a 5 mm thickness of NE 102A plastic scintillator viewed by a 5" photomultiplier (type EMI 9530A), was constructed around the collimator

for the discrimination of charged particle events.

2.6 The Test Flight

The modulation collimator was flown as a result of an extension of a UTIC (University of Tasmania/Imperial College) joint balloon programme. The primary aim, as far as Imperial College is concerned, was a test flight of the prototype 133 cm^2, 20-200 keV crystal phoswich module (in which 12 of these constitute the IC large area detector, to be flown in the autumn of 1980). The University of Tasmania, on the other hand, has the responsibility of maintaining the pointing position throughout the observation. On board the balloon an equatorial mount was adopted (Fig2.16) in which rotations about the RA

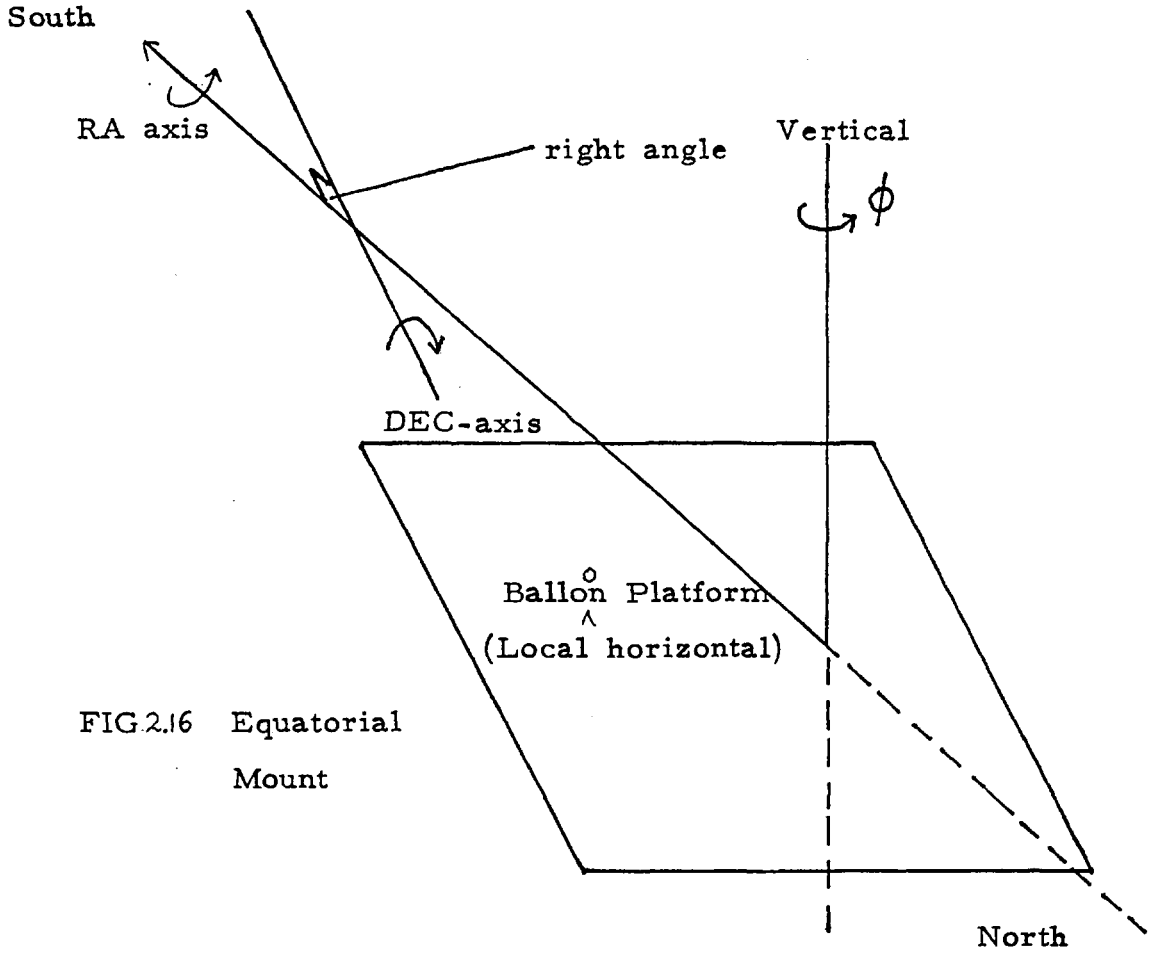


FIG 2.16 Equatorial Mount

and DEC axes allow the instrument to point at the desired position in the sky. The balloon platform was stabilised w.r.t. the local magnetic field by means of two magnetometers and a reaction wheel servo-loop. The original intention was to allow the pointing position to be slightly offset from the source. Counts were then taken (for all channels) once every $\frac{1}{2}$ second for $\frac{1}{2}$ hour, so that modulation is provided as the source transits across the detector due to the earth's rotation. Assuming an amount $\sim$ 3 gm cm^{-2} of atmosphere was present above the detector, the estimated observing time for a 3σ signal from the Crab are as follows :

TABLE 2.2

Energy	Time for 3σ signal
30 keV	5.2 min.
60 keV	17.2 min.
100 keV	4.1 min.

However, after launch it was soon found that the horizontal, i.e. balloon platform, was unsteady. It was rotated through an angle $\phi = \phi(t)$ (where t is the time) about the local vertical so that the NS axis no longer coincides with the true NS direction. The readings of the NS and EW magnetometers on board determine unambiguously the angle ϕ (see Figure2.17)so that the remaining problem is to work out the true RA and DEC in which the instrument is pointing in terms of the (apparent) RA and DEC at $\phi = 0$. A computer programme was written for such a conversion (Appendix). The output (Fig2.18)reveals that the Crab nebula

was in the field of view of the detector for a period of $\sim$ 1 hour, and within an angular distance of $\frac{1}{2}°$ for a period of 4 min.

The important point to note is that the irregular motion of the platform caused drastic modification to the original triangular modulation profile. Any attempt in source location is discouraged by the fact that the inaccuracies of the magnetometer readings introduced large uncertainties $\delta\phi$ in ϕ, so that knowledge of the pointing direction at the 1° precision level was impossible. Moreover, the significance of the above statistical estimate was greatly reduced in the present flight, as the balloon only succeeded in reaching a height where $\sim$ 6 gm cm^{-2} atmosphere remained. Table2.3shows the observed background count rate together with the expected count rate from the crab using the new X-ray measurements from Ariel V (Carpenter et al 1976) and taking into account atmospheric attenuation, detection efficiency ε (Fig 2.7), the area and channel widths of the present device. It can be seen that in each case the signal does not reach a significance of 3σ (where σ is the poisson background fluctuation). Any time variation in the data cannot therefore be justified as due to modulation of the source signal.

TABLE 2.3

Note that the unit of time here is $\frac{1}{2}$ hour, the duration of the observation.

	Observed background count rate	Poisson error σ in background	Predicted count rate from Crab
Channel 1	3×10^4	173	146
Channel 2	3×10^4	173	423
Channel 3	8.4×10^4	290	780
Channel 4	7.5×10^4	275	382

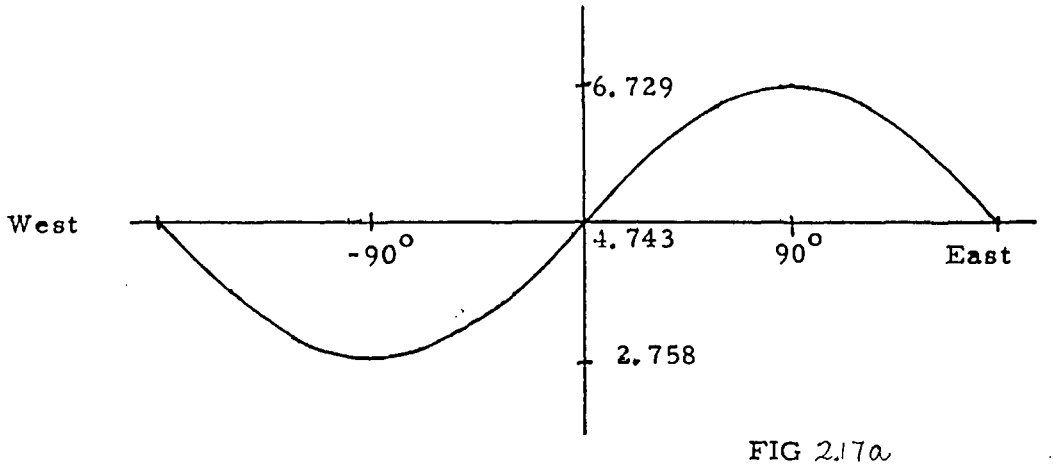


FIG 2.17a
Calibration of NS Magnetometer

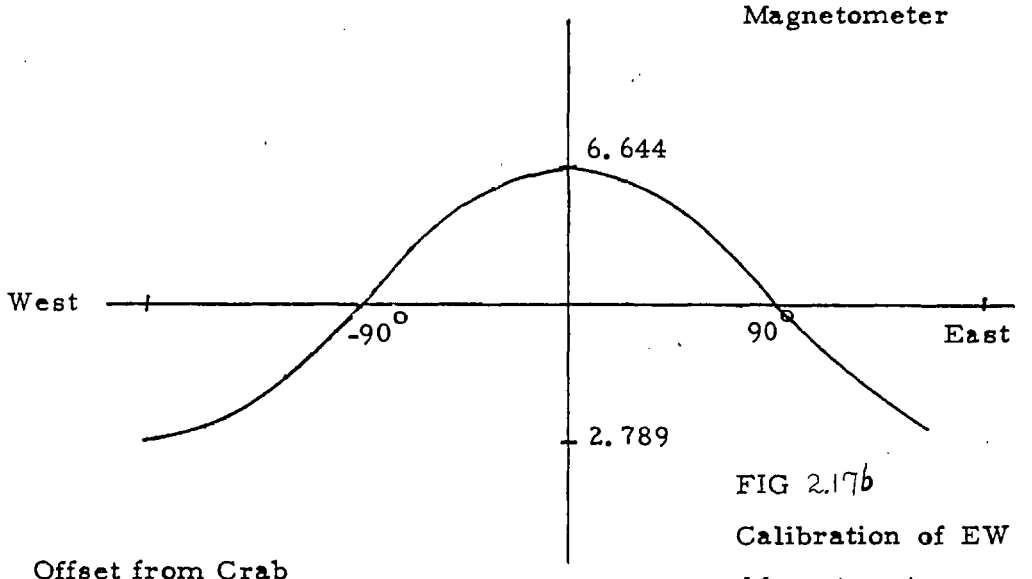


FIG 2.17b
Calibration of EW Magnetometer

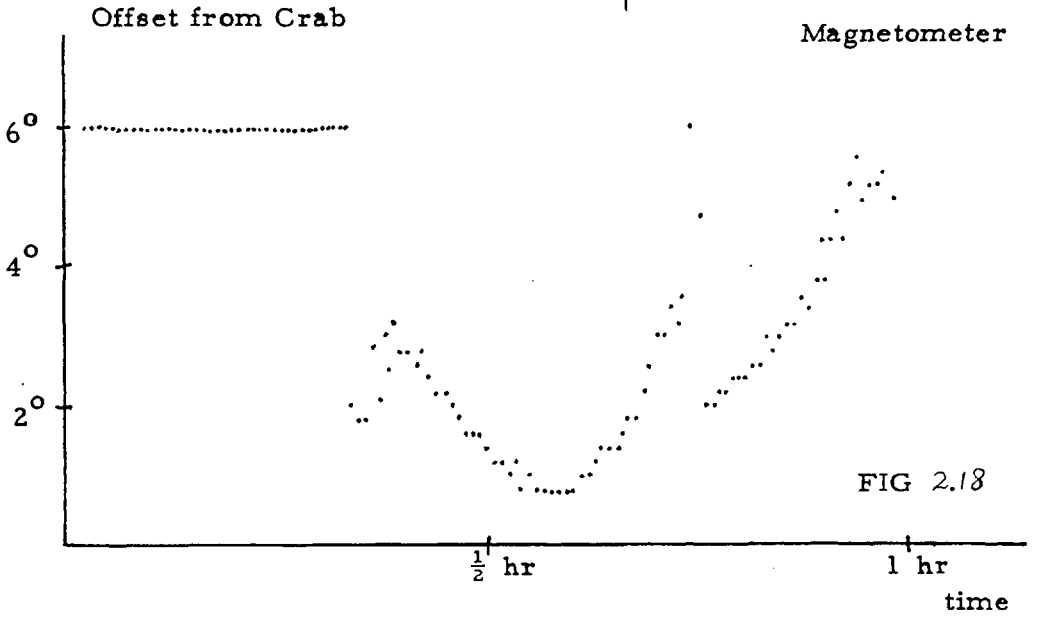


FIG 2.18

CHAPTER 3

ARIEL V HARD X-RAY OBSERVATIONS OF VELA X-1

3.1 Introduction

An approximately 55-day observation of the binary X-ray pulsar Vela X-1 (3U0900-40, RA135.06, DEC-40.36) was performed from February 7th 1979, using the Imperial College high energy X-ray detector on board the Ariel V satellite. Data analysis eventually led to two additional upper limits which strongly suggest a steep cutoff of intensity at hard X-ray frequencies. At lower energies a spectral point, obtained from experiment A data, will also be briefly discussed. Information concerning the X-ray detector, the satellite, and the conventional observing programme is kept to a bare minimum here, as details can be found in previous literature (see e.g. Engel et al (1976), Coe (1977)).

3.2 The Detector

This is a high energy scintillation telescope sensitive to X-ray energies 26 keV - 1.2 MeV. It gives the photon flux for each of the 15 energy channels within this range (e.g. channel 1 : 26-34 keV, see Engel et al (1977)) but the small sensitive area (8 cm^2) limits the accuracy of the observations.

3.3 The Observation

The spin-modulation technique, in which the detector axis is offset by 3° from the satellite spin axis, so that as the satellite spins the source signal is modulated but not the background, was employed. The most important 1st harmonic content (as this accounts for > 90% of the modulated signal) was measured by dividing counts from each spin period into four sectors. For each orbit of the satellite the output from the four sectors was separately accumulated into approximately 12 integration periods (of equal duration) of which 5 would be in eclipse w.r.t. the source. The data in the remaining 7 integration periods was re-binned into 7 orbit sections, the start of the first one always corresponded to the finish of the eclipse. Finally, orbit sections that include radiation-belt contamination or bit errors in the data which can arise in the transmission process, were rejected. The overall procedure excluded $\sim$ 71.5% of the full orbit.

The major problem with the spin-modulation technique is the presence of the anisotropic cosmic ray background modulation (the cosmic rays being anisotropic due to the presence of the earth). To overcome this observations are made with 3° offset on either side of the source so that the phase of the background modulation remains the same but that of the source changes by 180° (Engel and Coe, 1977; Coe, 1976).

However, at the time of the observation Ariel V has already entered its 5th year in orbit, so that the orientation of the satellite was no longer controlled by propane gas jets, but rather by the less reliable magneto-torquors. Measurements at opposing offset positions did not prove to be possible. Rather, the actual observation took the form of a 'horizontal' scan of Vela X-1 (135.06, -40.36) from

RA 153° to RA 130° at a constant declination of -44°±2°. It should now be clear that a somewhat different approach is necessary to remove the modulated background.

3.4 Data Analysis

First of all, ∿ 16% of useful data was removed as they correspond to predicted periods of binary eclipse of Vela X-1 from an extrapolation of Watson et al (1977) (taking into account the max. error in their result). The remaining observation was conveniently divided into 13 positions A to M, the mean pointing positions of these are given by the centre of the squares in Fig.3.1.Within every observing position, data in each orbit section was summed and the method of harmonic analysis was used to give a signal (magnitude, direction and their corresponding errors). It turns out from statistical considerations that the 'optimum' approach was to combine further the signals (and the errors) within energy channels 1-3 (26-56 keV) and 4-6 (56-121 keV). If, in the zeroth order approximation, we assume a constant background

$$b = b_o$$

and if each of these signals is resolved into components parallel to the (local) RA and DEC directions, then one would expect (theoretically at least) the variations of these components with observing position to be something similar to Fig3.2Asince, broadly speaking, the observation took the form of a scan of Vela X-1 at constant DEC. On the other hand, if the background changes slowly with time, we may include a first order approximation term,

$$b = b_o + b_1 t \qquad (3.1)$$

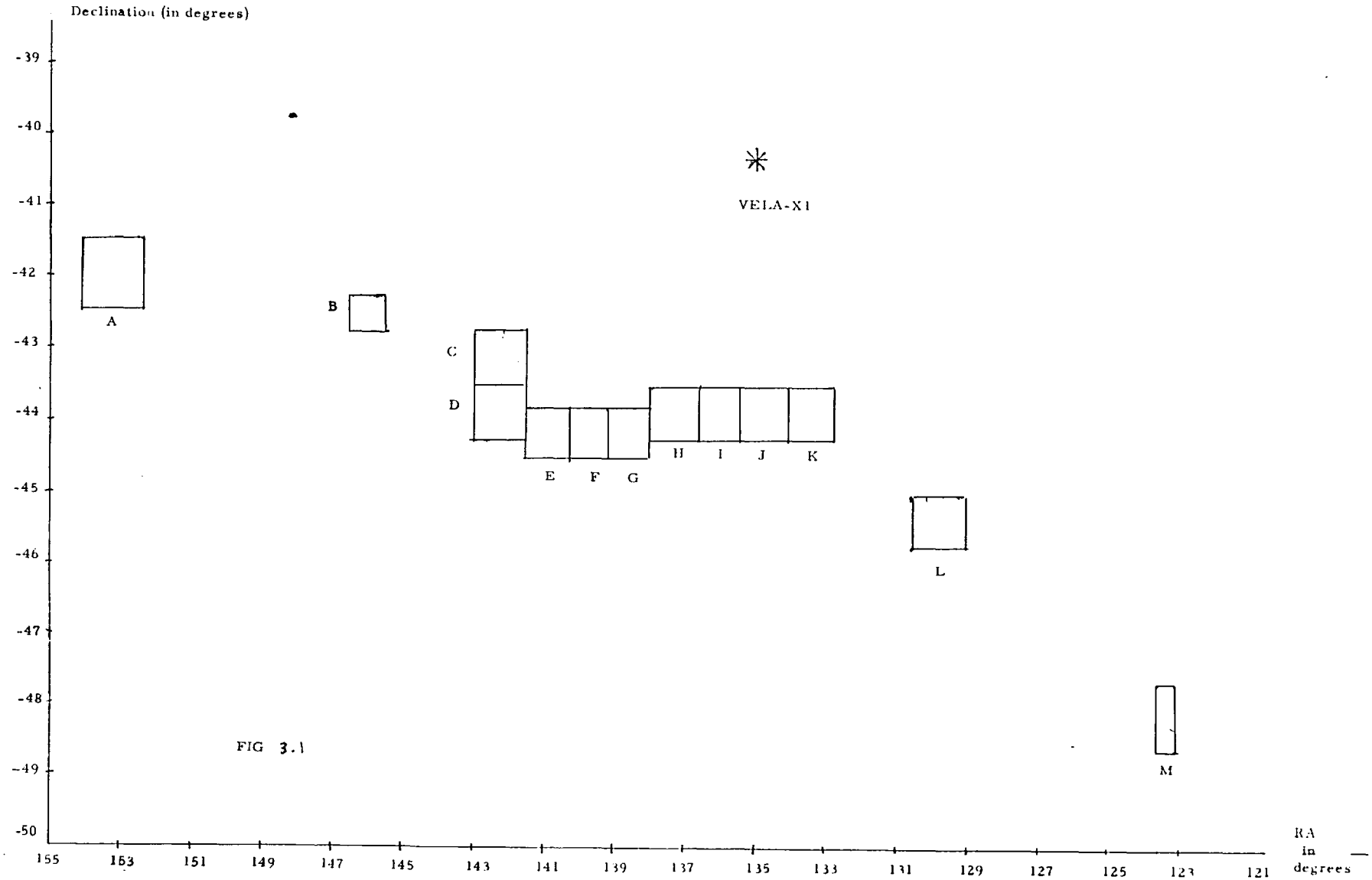

Declination (in degrees)
-39
-40
-41
-42
-43
-44
-45
-46
-47
-48
-49
-50
VELA-X1
A
B
C
D
E
F
G
H
I
J
K
L
M
155
153
151
149
147
145
143
141
139
137
135
133
131
129
127
125
123
121
RA
in
degrees

FIG 3.1

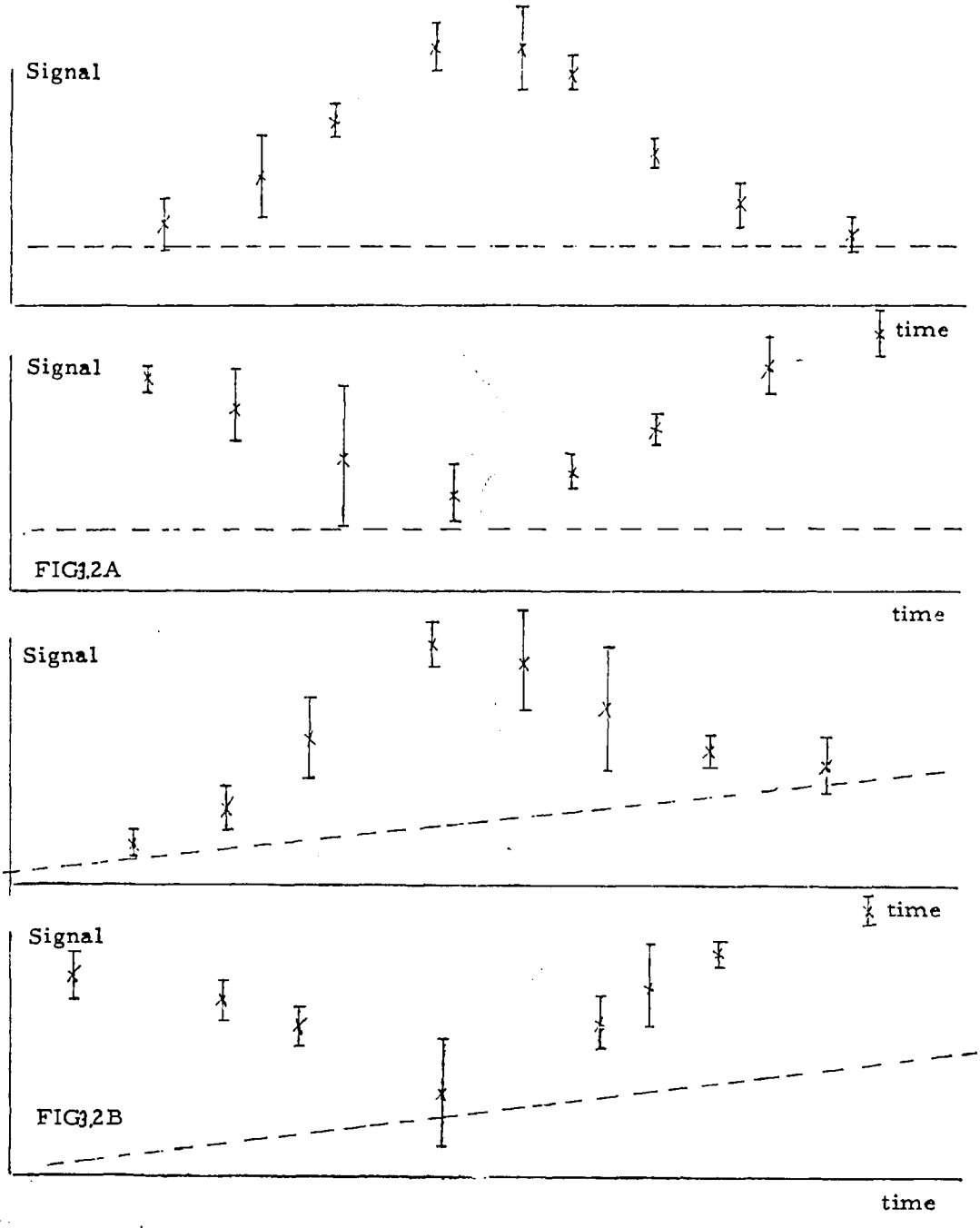


FIG 3.2 Empirical variation of signal with time for present observation. Dotted lines represent asymptotic background. The case of constant background is illustrated in Fig 2A for the RA component of the signal(above) and the DEC component (below). In Fig 2B the same plots are repeated with a small linear change in background.

so that the variations now look like Fig.3.2B When this was done to the real data, the variations for the two energy channels (1-3 and 4-6) for one of the orbit sections were illustrated in Fig.3.3A,3.3B,3.4A,3.4B

The actual values for b_o and b_1 (and their errors) have to be known in order to determine the background. To this end the predicted count rate for each of the 13 positions was calculated by folding the (extrapolated) OSO-8 spectrum at low absorption (Becker et al, 1978) into our detector response matrix (Engel et al, 1977). As illustration, the count rate in energy channels 1-3 is given by

$$\frac{dN}{dt} = \int_{E = 26\ keV}^{56\ keV} I(E)\ A\eta(E)dE$$

where I(E) is the OSO-8 spectral intensity at energy E, A is the area of our detector and η is the detection probability of a photon at energy $E = \hbar\omega$ as given by the matrix (in practice the integral was done numerically and the count rate was found to be $\sim 0.19\ s^{-1}$). The predicted count rate for each position then is given by

$$\frac{dN}{dt} \times \varepsilon(\theta)$$

where θ is the (mean) offset of the position from Vela X-1 and ε is the angular response of the detector (Engel et al, 1977). The results for channels 1-3 (resolved into RA and DEC directions) are given in Figs.3.3C,3.3D and for channels 4-6, Figs. 3.4C,3.4D.

From the empirical plots it is clear that our detector is not expected to obtain appreciable signals (in any energy channels) in the RA direction when the pointing positions are A, J and M. All data from these positions may be taken (empirically) as the background. If we wish to take the 1st order approximation of the background (eqn.3.1), then the slope and the intercept of the best straight line through the signals in those

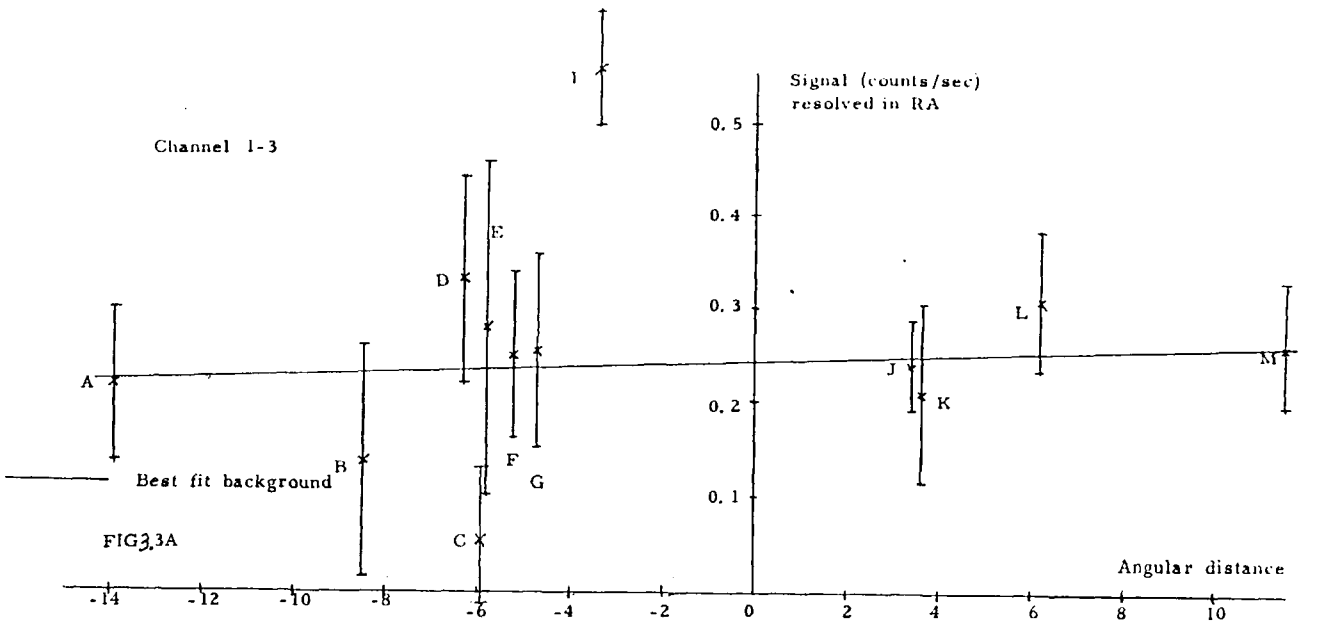


FIG 3.3A

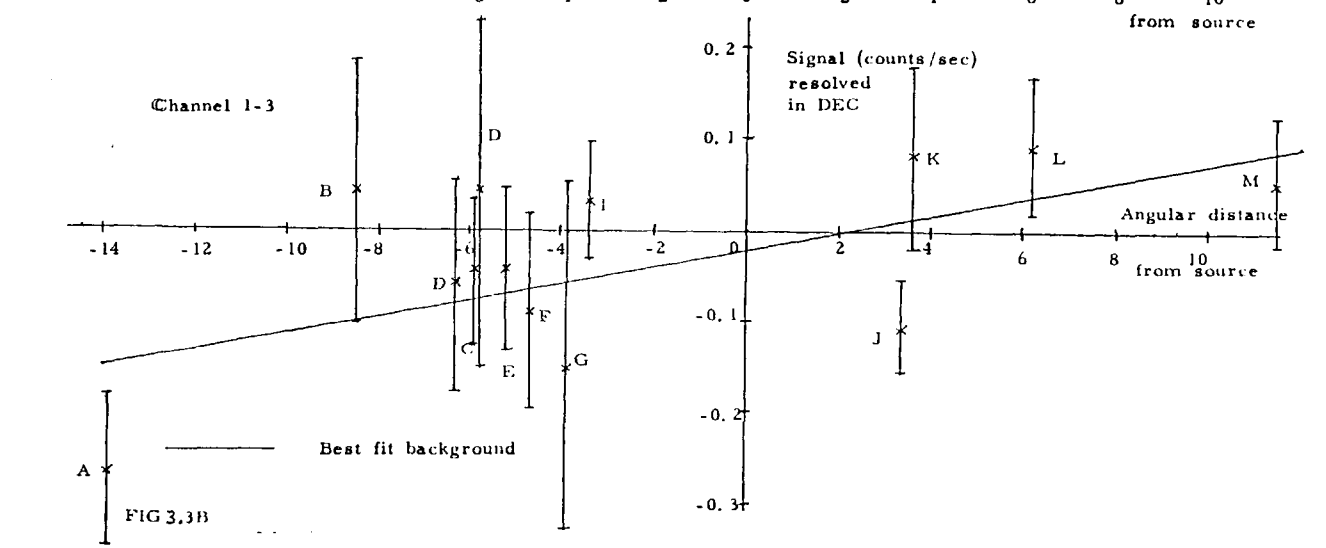


FIG 3.3B

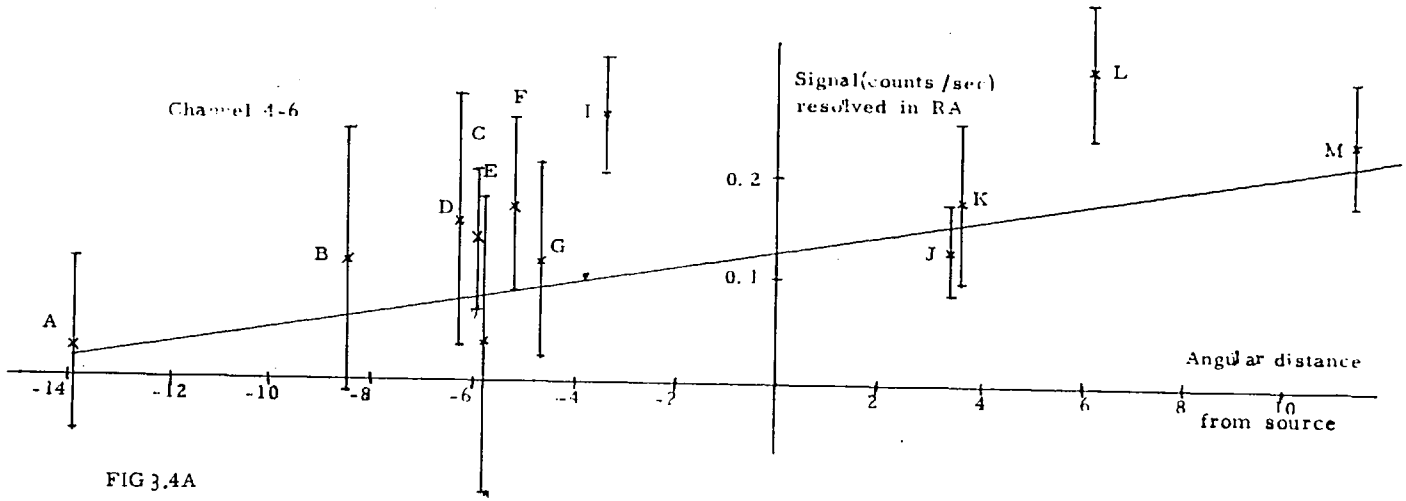


FIG 3.4A

——— Best fit background

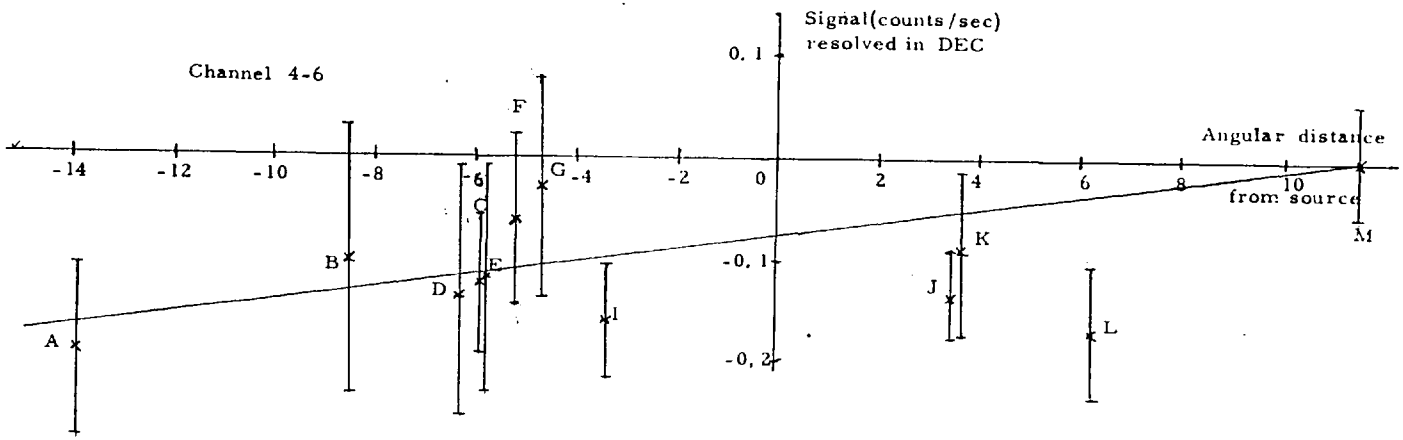


FIG 3.4B

——— Best fit background

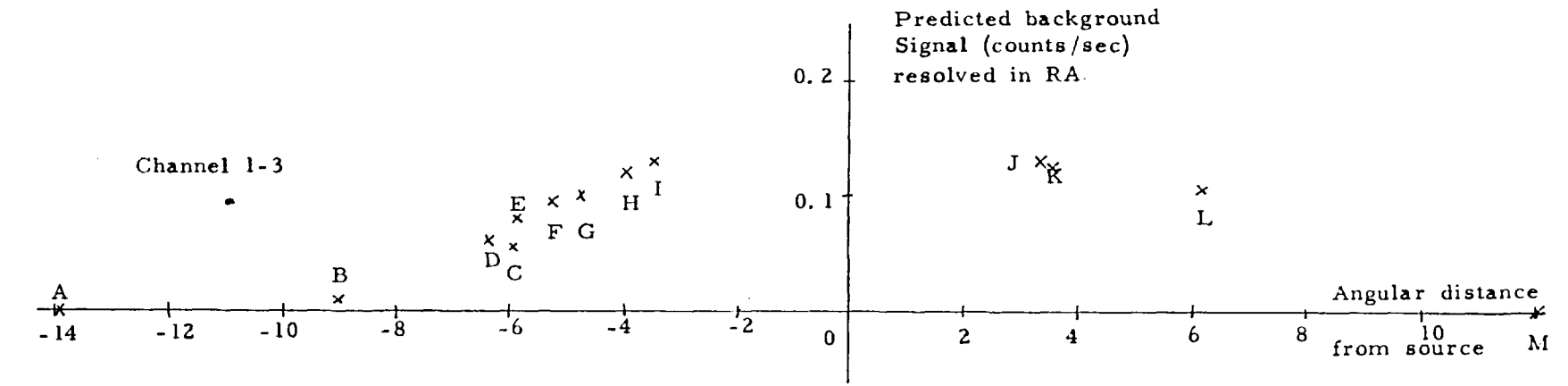


FIG3.3C

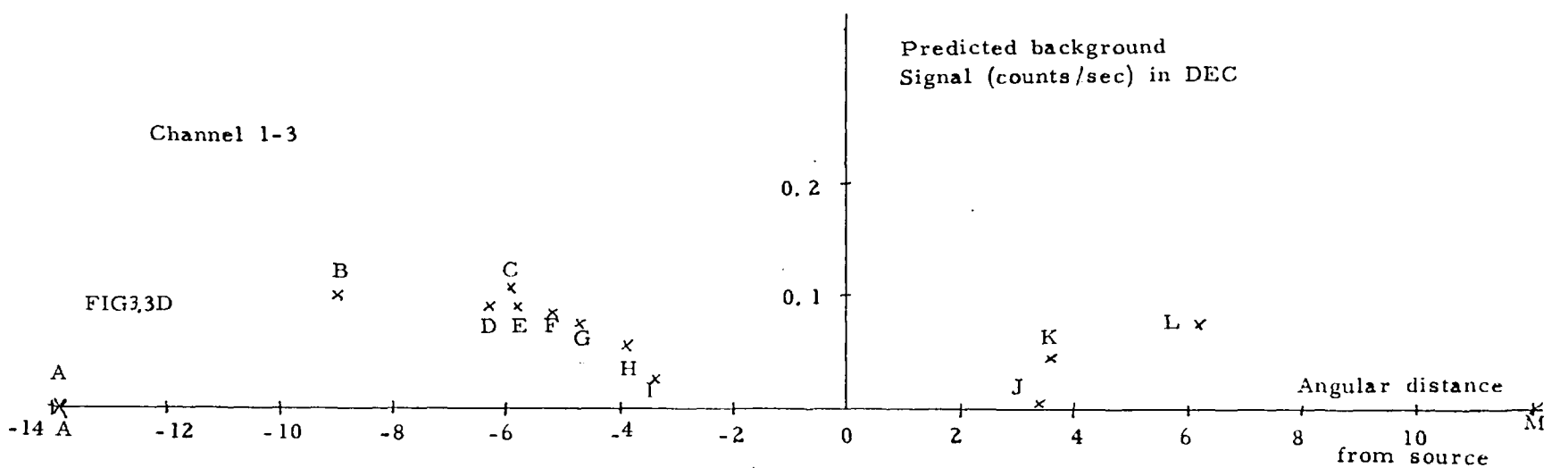


FIG3.3D

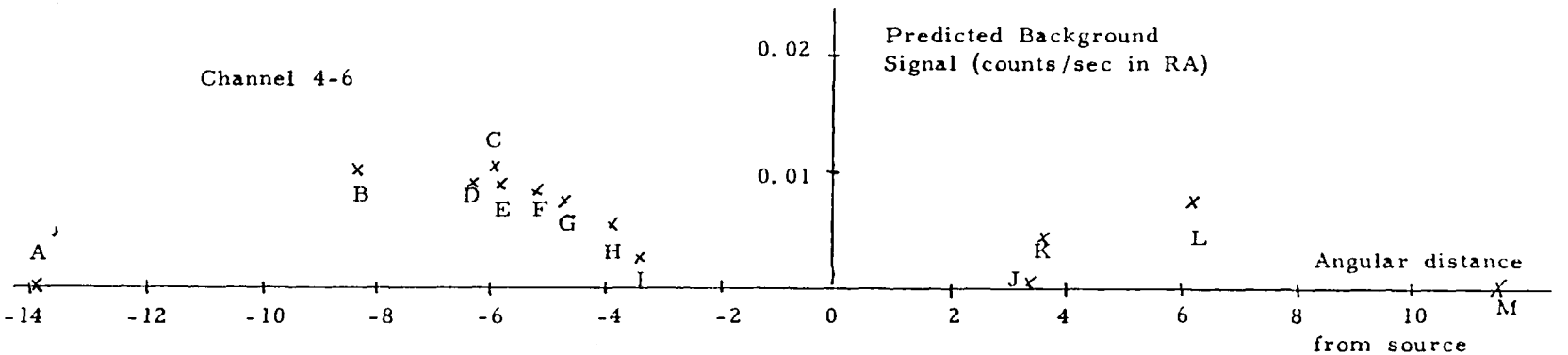


FIG 3.4C

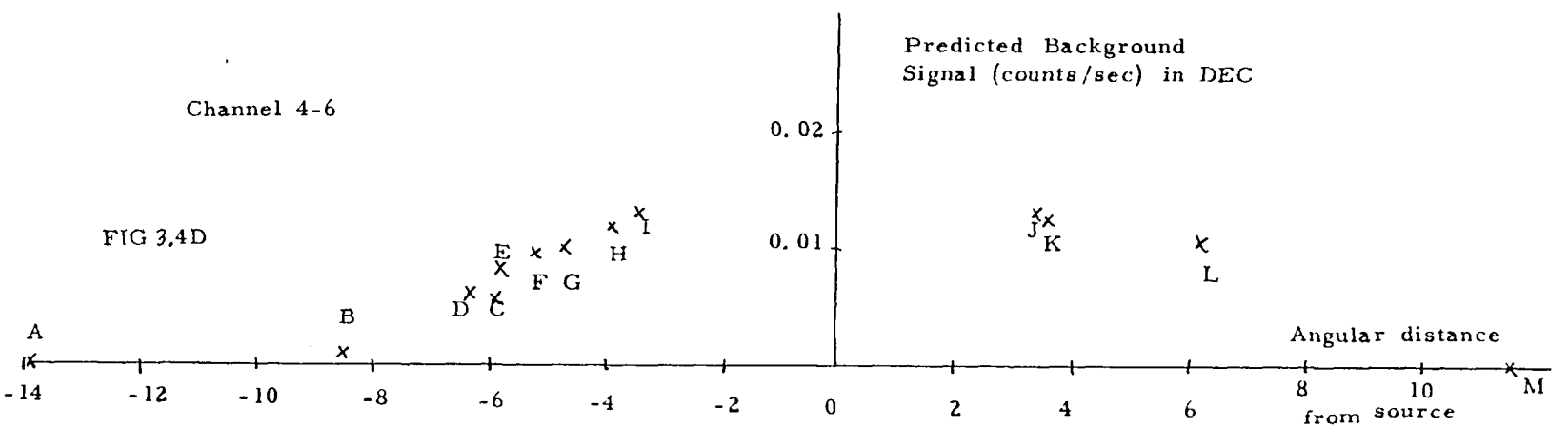


FIG 3.4D

positions will give the values of b_1 and b_o and their errors (strictly speaking, the abscissae does not give the time, but is proportional to the time since the successive observations A → M are in chronological order - a scan at constant DEC). Such straight lines were illustrated for the two energy channels and for a particular orbit section as in Figs.3.3A,3.3B,3.4A,3.4B Similar procedures were applied to the DEC plots, except that the background positions are now A, B and M.

The source signal at each pointing position was then obtained after removal of the predicted background count rate at that position. Care was taken to ensure that errors in both the original data and in the predicted background (the ones drawn in Figs.3.3&3.4 are the best fit straight lines, there are errors in the slope and intercept - b_1 and b_o) are taken into account. Using the angular response function of the detector (Fig.3 Engel et al 1977) it was possible to deduce the actual source signal from the signal in each observing position. The final results from all positions and from all orbit sections were then combined to give a mean source signal and rms error for the two energy channels 1-3 and 4-6. They are, respectively,

$$0.040 \pm 0.036 \ s^{-1}$$

$$0.038 \pm 0.033 \ s^{-1}$$

Earlier on in the chapter it was shown that the (extrapolated) OSO-8 spectrum predicted a count rate of $\sim 0.19 \ s^{-1}$ in energy channels 1-3. Now the same spectrum gives a value 1.3×10^{-3} cm^{-2} keV^{-1} s^{-1} for the specific intensity of Vela X-1 in energy channels 1-3 (26 - 56 keV). Since our present count rate is .04 ± .036 we deduce that our observation gives

$$\frac{0.04 \pm 0.036}{0.19} \times 1.3 \times 10^{-3} = (2.73 \pm 2.45) \times 10^{-4} \text{ cm}^{-2} \text{ keV}^{-1} \text{ s}^{-1}$$

for the spectral intensity of Vela X-1 at 41 keV (the mean energy of channel 1-3). Likewise we deduce a value

$$(2.05 \pm 1.78) \times 10^{-5} \text{ cm}^{-2} \text{ keV}^{-1} \text{ s}^{-1}$$

for the intensity at 88.5 keV (the mean energy of channel 4-6). Since the significance of signals is rather small, they are converted into 2σ upper limits. In addition to these results, a spectral point in the energy range 2.9 - 7.6 keV was obtained from an average of a 36 day observation (roughly between 9 February - mid-March 1979) of Experiment A - the proportional counter (see Coe et al 1976 for details). This together with our two upper limits at high energies is plotted respectively as points A, B, C in Fig 3.5, the OSO-8 spectrum being included for comparison.

3.5 Conclusion

The sharp energy cutoff of the OSO-8 spectrum at E > 40 keV is confirmed by the two upper limits A and B of the present analysis. Boldt et al (1976) suggested that the phenomenon is due to cyclotron resonance of the modified Thomson scattering cross-section in a magnetic field near the poles of a neutron star (see equ. 4.1 Chapter 4). On either side of the cyclotron frequency (i.e. $\omega < \omega_c$ or $\omega > \omega_c$) the Thomson opacity remains low, so that if a value $\hbar\omega_c \sim 40$ keV (which corresponds to a magnetic field $H \sim 3.5 \times 10^{12}$ gauss) is inferred for Vela X-1 then a gradual decrease in the slope of the spectrum is expected around $\hbar\omega \sim 20$ keV and $\hbar\omega \sim 100$ keV. The former is noted in the OSO-8 low energy data. The latter, however, is <u>not</u> suggested by our 2nd upper limit. Cyclotron processes in the extreme magnetic field of pulsars will be the subject of discussion of the next three chapters.

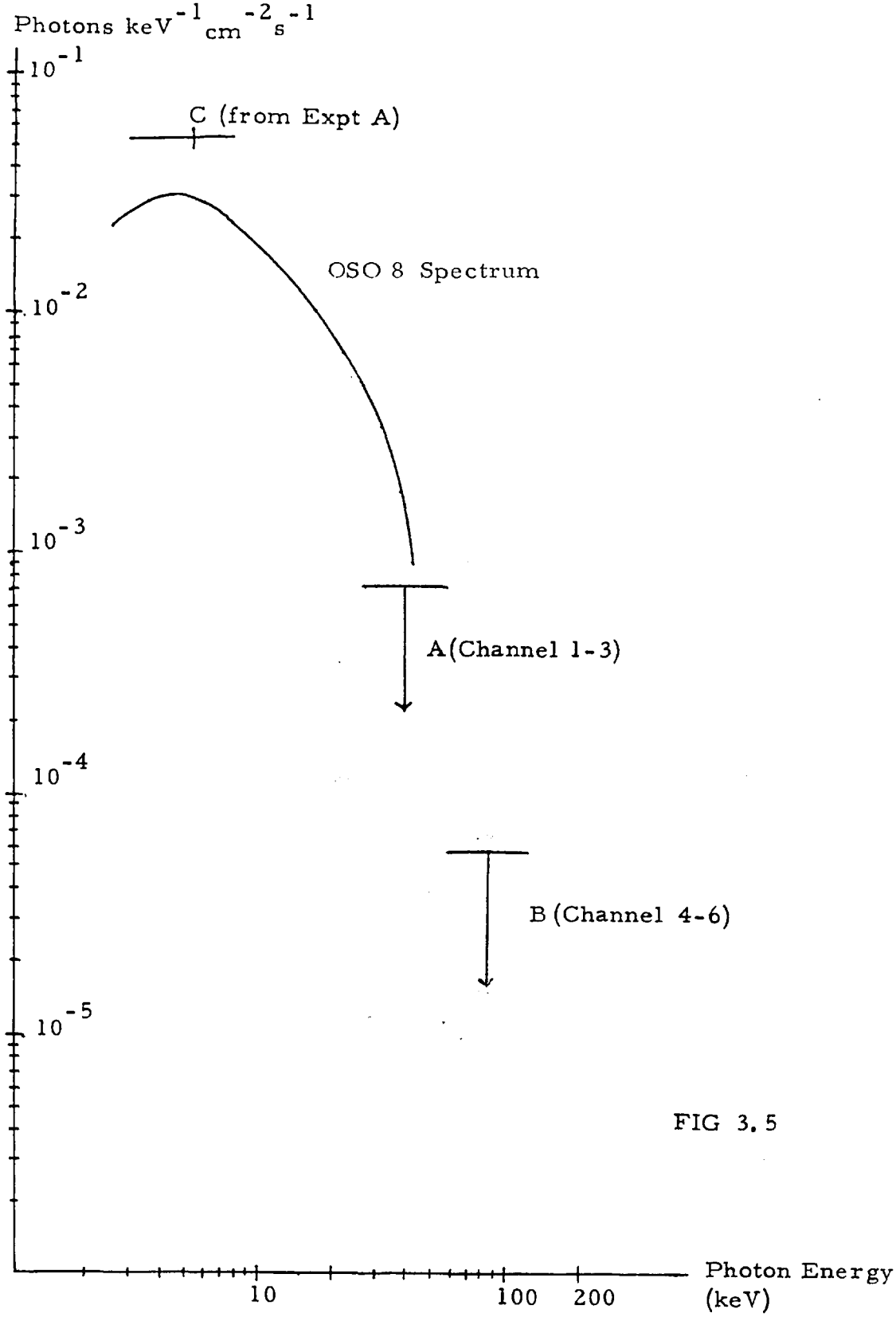

Photons keV^{-1} cm^{-2} s^{-1}
10^{-1}
C (from Expt A)
OSO 8 Spectrum
10^{-2}
10^{-3}
A(Channel 1-3)
10^{-4}
B (Channel 4-6)
10^{-5}
10
100
200
Photon Energy (keV)

FIG 3.5

Note Added in Proof (Chapter 3)

A time-averaged photon number spectrum in a limited range of Hard X-ray energies was provided recently by the MPI Group (Staubert et al, Astrophys. Journal, 239, 1010 (1980)). At low energies (E< 30keV) a gradual cutoff due to absorption was noted. At energies above 30 keV the data was fitted with a thermal bremsstrahlung spectrum with kT$\sim$10 keV

$$N(E) = 10\ E^{-1.4}\ \exp(-\frac{E}{10})$$

where E is the photon energy in units of keV. The count rate at energies 41 and 88.5 keV are respectively 9.15×10^{-4} and 2.7×10^{-6} $keV^{-1}cm^{-2}s^{-1}$ and hence consistent with our 2σ upper limits (see text).

Fits with a Modified Black Body Spectrum* at kT$\sim$10 keV can also be shown to be reasonable for both the high resolution but limited energy range MPI balloon data, and our poor resolution but wide energy range Ariel V data (wide range as we included the Expt A low energy point). At higher energies both sets of data shows a steeper fall off than that suggested by the modified b.b. spectrum. However, the cut-off predicted by Boldt et al 1976 (see text) is even steeper, although the more detailed computations of Nagel (Nagel, W. Astrophys. Journal, 236, 904 (1980)) does indicate a smaller slope for the special case of 'no switching' between the different polarization modes. However (as will be discussed in Chapter 6) doubt is cast on the correctness of the basic cross-sections used in the above paper.

---

* See Felten, J.E., Rees, M.J., 1972, Astron. Astrophys., 17, 226. Also Quenby, J.J. et al, 1979, Proc. Roy. Soc. Lond., A366, 295.

CHAPTER 4

RADIATION PROCESSES IN THE MAGNETIC POLAR REGIONS OF AN ACCRETING BINARY PULSAR

4.1 Introduction to Binary X-ray Sources

The high variability ($\sim$ seconds), large luminosity ($\sim 10^{36}$ - 10^{38} erg sec^{-1}), and the extent of the energy spectrum ($\sim$ 10 - 100 keV) of galactic X-ray sources suggest that they are related to gravitationally collapsed objects, viz. neutron star or black hole. At present there are two known possible sources of energy for radiation. They are :

1. Rotational kinetic energy as a result of a continuous decrease in the angular velocity of the collapsed object (see, e.g. Rose 1973). Examples are the Crab pulsar and Vela X.
2. Gravitational energy as a result of accretion of matter from a companion star on to the collapsed object. This can also give rise to radiation detectable in the X-ray range (Hayakawa et al 1964). We shall subsequently be concerned with the second category, the well-known examples of which being Vela X-1, Her X-1.

If the companion star is small (or if binary motion is very rapid) matter can be transferred to the neutron star by such mechanisms as wind accretion, in which the plasma lost by the companion star is drawn towards the neutron star by its own gravitational field, cools, and is captured.

The plasma in this case may not have sufficient directional angular momentum to form a Keplerian accretion disk. However, if the companion is a red giant or super giant which overflows the Roche critical equipotential of the binary system, then matter flows through the unique gravitational saddle point (1st Lagrangian point, see Kopal 1959) and eventually forms an accretion disk round the compact object (Prendergast and Burbidge, 1968). Soft X-rays of energy < 1 keV are then expected to come predominantly from the accretion disk and not from the star (Gorenstein et al 1976). The inner edge of the disk occurs when the pressure of the dipolar magnetic field becomes equal to the pressure at the mid-plane of the disk

$$\frac{B^2_{\text{dipole}}}{8\pi} = P_{\text{disk}}$$

(Pringle and Rees 1972) where $B \sim 10^{11} - 10^{13}$ gauss for a neutron star. The plasma then enters the magnetosphere as a result of an instability of the boundary (Lamb et al 1973), moves along the field lines towards the magnetic poles of the star (Yahel 1979). Some radiation generation or re-processing takes place throughout the region of fall but it is in these polar regions immediately above the star's surface - regions of size $\sim$ one-tenth the size of the neutron star (Gnedin and Sunyaev 1973) - that most of the gravitational to thermal energy conversion takes place (perhaps via a shock) and hard X-ray temperatures are generated. If the pulsar rotation axis is not aligned with the dipolar axis, these polar 'hot spots' will appear and disappear from the earth's field of view as the star rotates, thus constituting the standard model of X-ray binary pulsars.

4.2 Experimental Evidence of the Association of Strong Magnetic Field with Pulsars

It is estimated that the gravitational energy released as a result of the electron 'freely falling' from infinity to the surface of the star does not render the electrons relativistic, the energy has to come from other sources (such as from protons in a shock near the surface of the star). Theoretical models thus disagree widely on the temperature of the electron component (largely responsible for radiation) of the plasma. However, the situation appears more hopeful on the experimental side. If we assume that cyclotron bremsstrahlung (i.e. bremsstrahlung in an intense external magnetic field - the dominant emission mechanism - see later for reason) is an efficient process so that the temperature of the X-ray spectrum essentially gives a measure of the temperature of the electron distribution, then there is considerable evidence that the motion of electrons is only mildly relativistic - i.e. $\sim$ 10 - 100 keV (Mészáros 1978). In a magnetic field H $\sim 4.10^{12}$ gauss such electrons are quantum mechanical (or strictly speaking, relativistic q.m.) in nature, since the energy levels of an electron in a magnetic field are discrete (Landau levels) and, for a typical pulsar field H $\sim 4.10^{12}$ gauss the first available non-zero energy state is already $\sim$ 60 keV. Transitions between such quantized energy levels give rise to cyclotron emission and absorption lines at integral multiples of the cyclotron frequency (as opposed to ordinary cyclotron harmonics, which also occurs at the same frequencies).

The first experimental report of a cyclotron line feature is from the MPI Munich group (Trümper et al 1977) on the binary X-ray pulsar Her X-1. The discovery was supported by a number of confirmatory observations (Evans et al 1980, Lewin 1978) on the same source. Apart

from Her X-1, spectral features of a similar type have also been reported from the sources 4U0115+63 (Wheaton et al 1979) and 4U1626-67 (Pravdo et al 1979).

Our present objective is to develop a model for the matter radiation transport in the accretion column near the polar regions. As stated earlier, the gravitational potential energy is converted into random thermal energy in a shock region near the surface of the star, which is partially dissipated in the form of radiation, predominantly due to collisional and radiative de-excitation of the electrons. Radiative transition rate for electrons which occupy only the lower Landau levels have been calculated (see Chiu et al 1969 for cyclotron emission, Daugherty et al 1978 for absorption). Nagel (1980) showed that in the accretion column this is much greater than the electron-ion collision rate. The conventional cyclotron emission-reabsorption processes can thus be treated as scattering of off-shell electrons, i.e. compton scattering, whereas it is the electron bremsstrahlung coefficients which should be used for resonant emission and absorption. Apart from interaction with matter, the radiation is also capable of creating e^+e^- pairs as it propagates through the magnetized vacuum (vacuum polarization). The next three sections are devoted to a review of the above underlined interactions, the overall result of which is an optical depth and dispersion of the medium which depends on the polarization of the photon in an essential way.

4.3 Compton Scattering

Cross sections for compton scattering in an external magnetic field was first calculated in the weak field and non-relativistic limit by Canuto et al (1971) who obtained results for two linear polarization modes

$$\sigma_1 = \sigma_{Th} \{ \sin^2\theta + \tfrac{1}{2} \cos^2\theta \left[\left(\frac{\omega}{\omega+\omega_c}\right)^2 + \left(\frac{\omega}{\omega-\omega_c}\right)^2 \right] \}$$

$$\sigma_2 = \tfrac{1}{2} \sigma_{Th} \left[\left(\frac{\omega}{\omega+\omega_c}\right)^2 + \left(\frac{\omega}{\omega-\omega_c}\right)^2 \right] \qquad (4.1)$$

where the polarizations 1 and 2 are chosen such that, when the radiation is propagating transverse to the magnetic field ($\theta = \pi/2$), the first configuration (commonly referred to as the O-mode by plasma physicists) has electric field $\underline{E}$ aligned with $\underline{H}$, whereas the second configuration has $\underline{E} \perp \underline{H}$. As can be seen from the formulae, in the low frequency limit (in which the radiation can be treated as classical) the Thomson opacity is low for soft X-rays of type-2 polarization propagating normal to the magnetic field. However, as $\omega \to \omega_c$, σ_2 resonates while σ_1 remains at the classical value of σ_{Th} for perpendicular propagation.

In a pulsar field $H \sim 4.10^{12}$ gauss the first Landau level has energy 60 keV, the non relativistic and weak field limit of Canuto et al (1971) is modified by effects of quantum electrodynamics. The exact Compton cross-section was first calculated by Herold (1979) and is exceedingly complicated. This is due to the fact that the virtual electron state (electron propagator) in a magnetic field has no simple mathematical structure. Chapter 5 presents a revised calculation which makes use of a greatly simplified form of the electron propagator for 10 - 100 keV electrons which occupy only the first few Landau levels. The result is a reasonable expression (eqn.16, Chapter 5) although the full physical implications of which is still to be explored. However, significant deviations from Herold's final result were found, especially at low frequency. It was also clearly recognised that σ_1 resonates for perpendicular propagation, in contrast to the predictions of the early non-relativistic calculation.

4.4 Cyclotron Bremsstrahlung

Earlier calculations of the bremsstrahlung coefficients in a strong external magnetic field have been unsatisfactory (for details, see Chapter 6). Chapter 6 shows again how the simplified electron propagator leads to a more comprehensible expression for the emission coefficient. In addition, particular emphasis is put on the integration over the possible range of momentum transfer during a single collision with the ion. Typical behaviour of the differential cross-section for the two linear polarization modes was considered for forward and backward electron scattering. (The high $\underline{B}$ effectively renders the electron motion one dimensional.) It was found that the previously predicted behaviour at low frequencies (Lodenquai et al 1974) for the two modes is only correct in the limit of weak field and large momentum transfer. In the extreme quantum limit of strong magnetic field and low momentum transfer, the ordinary mode 1 for perpendicular propagation goes above the $\underline{B} = 0$ result at low ω while mode 2 still goes to zero. At higher frequencies resonances are present irrespective of the polarization, although it was previously thought that there was no 'O'-mode resonance.

4.5 Vacuum Polarization

The plasma through which the radiation propagates is a dispersive medium because of its polarized nature. For low frequencies the cold plasma dispersion theory applies so that for example the second mode (2) does not propagate normal to the field. At higher frequencies the radiation polarizes the medium by creation of electron-positron pairs. Classically the magnetized vacuum displays a birefringence (Adler 1971, Mészáros and Ventura 1978, 1979) with refractive index

$$n \sim 1 + \delta \sin^2\theta, \quad \delta = \frac{1}{45\pi} \alpha \left(\frac{B}{B_{cr}}\right)^2 \sim 2.6 \times 10^{-6} B_{13}^2$$

This may be compared with similar dispersive terms in the plasma

$$\left(\frac{\omega_p}{\omega}\right)^2 = \frac{4\pi e^2 n}{m\omega^2} = 1.4 \times 10^{-7} n_{20} (\hbar\omega/\text{keV})^{-2}$$

$$\left(\frac{\omega_p}{\omega_H}\right)^2 = \frac{4\pi n m c^2}{B^2} = 10^{-9} n_{20} B_{12}^{-2}$$

where ω_p = plasma frequency, ω_H = electron gyro-frequency. For a field $B \sim 4.10^{12}$ gauss, an expected plasma density $n \sim 10^{21}$ cm^{-3} and keV photons, the effect of medium polarization on the photon is via the vacuum and not the plasma. It is hoped that future investigations will incorporate the simplified electron propagator (Section 4.3) in the calculation of vacuum polarization in the high B, QED limit. Any experimental agreement with predictions sensitive to the results of such a calculation will provide additional confirmation of the vacuum polarization. To date the experimental verification depends entirely on coulomb field induced scattering.

4.6 Overall Radiation Transport

Further research in this field will undoubtedly include the above modified cross-sections in a comprehensive photon transport model in order to compare with current and future observations. It appears appropriate to start with a cylindrical uniform high B and T region with some model of possible optically thin 'edges'. 'O' and 'E' modes of propagation and energy changes in the photon distribution function should be considered. Both a diffusion equation approach (Gnedin and Pavlov 1974) and an integral equation (Pomraning 1973) should be attempted with a dispersion relation between k and ω due to vacuum polarization. A number of partial treatments are available in the literature, but no comprehensive model. Further, predictions already made

which depend on the absence of resonance in the 'O' mode together with mode switching in the boundaries (Nagel 1980) are likely to be drastically modified by the use of the revised cross-section.

CHAPTER 5

A NEW APPROXIMATION FOR THE HIGH MAGNETIC FIELD COMPTON CROSS-SECTION*

5.1 Introduction

As mentioned previously, the present chapter is devoted primarily to the search of an analytical expression for the compton scattering cross section in an intense magnetic field. A previous calculation was performed (Herold 1979). As discussed in Chapter 4, the electrons near the surface of a neutron star are mildly relativistic and do not occupy more than the 1st few Landau levels, so that it is possible to re-construct the intermediate virtual state which exists during the transient period of radiative or coulomb interaction, and to arrive at a simpler and more complete expression of the cross-section. Although not explicitly apparent, the same assumption concerning the energy of the electrons is essential in the more sophisticated calculation of the cross-section, the reasons being :

i) The incident and recoiled electron may be confidently taken to be at the ground state (i.e. state with energy $E = (p_z^2c^2 + m^2c^4 + 2j\varepsilon^2)^{\frac{1}{2}}$, $\varepsilon^2 = \frac{H}{H_{cr}} mc^2$, $j = 0$) only if the perpendicular motion of the electron is barely relativistic.

ii) The cross-section was evaluated in the frame $p_z = 0$ and may be

---

* Work also accepted for publication in 'Astrophysics and Space Science'.

taken to be a correct approximation for the more complicated expression for finite p_z only if p_z is small.

The quantum mechanics of electrons in the absence of radiation was discussed in Johnson et al (1949). However, the author feels that certain conceptual difficulties need to be resolved before one can confidently turn to a more detailed presentation of the compton cross-section.

5.2 Symmetry Properties of the Motion of a Charged Particle in a Uniform Magnetic Field

The canonical formalism leads most naturally to quantization. The lagrangian for motion in a uniform, time independent magnetic field is

$$L = \tfrac{1}{2} m \underset{\sim}{v}^2 - \frac{e}{c} \underset{\sim}{A}.\underset{\sim}{v}$$

From this we compute the canonical momentum

$$\underset{\sim}{p} = \frac{\partial L}{\partial \underset{\sim}{v}} = m \underset{\sim}{v} - \frac{e}{c} \underset{\sim}{A} = \underset{\sim}{\pi} - \frac{e}{c} \underset{\sim}{A}$$

where $\underset{\sim}{\pi} = m\underset{\sim}{v}$ is the physical (kinetic) momentum of the electron. The hamiltonian is

$$H = \underset{\sim}{p}.\underset{\sim}{v} - L = \frac{1}{2m} (\underset{\sim}{p} + \frac{e}{c} \underset{\sim}{A})^2 = \frac{\pi^2}{2m} = \tfrac{1}{2} m \underset{\sim}{v}^2$$

and may clearly be identified as the total energy E (since H is time-independent, E is a conserved quantity). We can choose the z-axis to be the direction of the magnetic field. In addition there is also the freedom of choosing the gauge in which $\underset{\sim}{A}$ can be written as

$$\underset{\sim}{A} = \tfrac{1}{2} (-Hy, Hx, 0)$$

Hence
$$H = \frac{1}{2m} [(p_x - \frac{m\omega_c}{2} y)^2 + (p_y + \frac{m\omega_c}{2} x)^2 + p_z^2] \qquad \omega_c = \frac{eH}{mc} \qquad (5.1)$$

In this setting we can do quantization simply by taking the canonical

momentum $\underset{\sim}{p} \rightarrow -i\hbar$ grad. The non-relativistic Schrödinger eq. is

$$H\psi = i\hbar \frac{\partial \psi}{\partial t} \tag{5.2}$$

This equation is expected to be invariant under all symmetry transformations related to the motion in a uniform magnetic field, viz. gauge transformation, space reflection, time reversal, rotation about z axis and translation in the xy plane. It was found that indeed all above operations leave (5.2) unchanged (see e.g., Rose, M.E., 1961) except the last one. This can be demonstrated as follows. A spatial translation is generated by the operator $\underset{\sim}{p}$. This means, e.g., that if there is a translation by an amount a in the x-direction

$$H \rightarrow H' = e^{\frac{-ip_x a}{\hbar}} H e^{\frac{ip_x a}{\hbar}}$$

$$= \frac{1}{2m} \{(p_x - \tfrac{1}{2} m\omega_c y)^2 + [p_y + \tfrac{1}{2} m\omega_c (x-a)]^2 + p_z^2 \}$$

$$\psi \rightarrow \psi' = \psi$$

so that (5.2) is clearly not invariant.

This apparent paradox may be resolved by the observation that the canonical translation generated by $\underset{\sim}{p}$ does not actually correspond to a physical translation. A physical translation (in its real sense) involves a change in position but no change in physical (kinetic) momentum. Here, however, a translation in the x-direction clearly changes $\pi_y = mv_y$ (this is related to the fact that $\underset{\sim}{p}$ is not the physical momentum). We suggest that the correct procedure is to perform a gauge transformation of the 1st kind (i.e. on the hamiltonian only) after the canonical translation. In the above case the generator for the additional gauge transformation we introduce is $\Lambda = \frac{eH}{2c} y$ so that the full generator for physical translation in the x-direction is

$$P_x = p_x + \frac{eH}{2c} y = \frac{eH}{c} \left(\frac{y}{2} + \frac{p_x}{m\omega_c}\right) = m\omega_c y_o \tag{5.3}$$

As we shall see shortly, y_o is the operator corresponding to a measurement of the y-coordinate of the guiding centre of the electron.

By the same token we deduce that

$$P_y = -m\omega_c x_o = -m\omega_c\left(\frac{x}{2} - \frac{p_y}{m\omega_c}\right) \tag{5.4}$$

is the corresponding generator in the y-direction. In this way we see that physical translations in the x- and y- directions are effectively generated by the y- and x-coordinate of the guiding centre of the electron. Notice that in this context translations in the x and y directions are no longer commuting operations. This is due to the fact that the operators x_o and y_o do not commute (again a fact which we shall discuss shortly).

5.3 Absorption and Emission of Photon

It is well known that a freely moving electron is incapable of absorbing or emitting a photon, due to the fact that the energy and momentum conservation equations are incompatible.

$$\underset{\sim}{p}' = \underset{\sim}{p} + \hbar\underset{\sim}{k} \qquad \frac{\underset{\sim}{p}'^2}{2m} = \frac{\underset{\sim}{p}^2}{2m} + \hbar\omega$$

In the presence of a magnetic field the process is no longer forbidden. In the Feynman diagram appropriate for the process (Fig. 5.1) the line in between two vertices represent a 'virtual state'. Depending on which procedure one would like to adopt (i.e. time-ordering or covariant perturbation) this implies that either energy conservation does not hold at the two vertices or the mass of the virtual state $m^2 \neq E^2-p^2$. However, some caution should be taken here because this is only describing 'free-free' transition for electrons in a magnetic field. So far nothing is said about the possibility of transitions between bound states (i.e. Landau levels). What follows is a demonstration of how this process is also allowed. Momentum and energy conservation can be reconciled within the scope of an uncertainty principle.

To this end it is advantageous to perform the following canonical

transformation to the hamiltonian(5.1)before quantization.

$$x = x_o + x_1 \qquad y = y_o - y_1$$

$$p_x = \tfrac{1}{2}m\omega_c(y_o + y_1) \qquad p_y = \tfrac{1}{2}m\omega_c(-x_o + x_1)$$

Here (x_o, y_o), (x_1, y_1) are conjugate variables.

The hamiltonian then becomes

$$H = \tfrac{1}{2}m\omega_c^2 \ (x_1^2 + y_1^2) \tag{5.5}$$

Since the remaining conjugate pair x_o, y_o do not appear in the hamiltonian we deduce that they are constants of the motion. Moreover we can write

$$H = E = \tfrac{1}{2}m\omega_c^2 \ [(x - x_o)^2 + (y - y_o)^2]$$

The trajectory in the xy-plane is thus a circle centred at (x_o, y_o).

The conjugate variables x_o and y_o can also be written as

$$\begin{aligned} x_o &= \frac{x}{2} - \frac{p_y}{m\omega_c} = x - \frac{\pi_y}{m\omega_c} \\ y_o &= \frac{y}{2} + \frac{p_x}{m\omega_c} = y + \frac{\pi_x}{m\omega_c} \end{aligned} \tag{5.6}$$

(cf. eqns 5.3&5.4)

Consider now the absorption of a photon. Energy conservation gives (neglecting z-direction) $E_f = E_i + \hbar\omega$ or

$$\frac{\underset{\sim}{\pi}_f^2}{2m} = \frac{\underset{\sim}{\pi}_i^2}{2m} + \hbar ck \tag{5.7}$$

where i = initial, f = final and $k = |\vec{k}|$. Quantum mechanically the initial and final energies (and hence the energy of the photon) are well-defined. This is due to the fact that the conjugate variables (x_1, y_1) in the hamiltonian(5.5)satisfy the commutation relation

$$[x_1, y_1] = \frac{i\hbar}{H}$$

so that we have a situation similar to the harmonic oscillator

$$E_n = (n + \tfrac{1}{2})\ \hbar\omega_c$$

(These are the well-known Landau levels). Next we turn to momentum

conservation

$$\underset{\sim}{\pi}_f = \underset{\sim}{\pi}_i + \hbar\underset{\sim}{k} \tag{5.8}$$

or

$$\pi_x^f = \pi_x^i + \hbar k_x$$

$$\pi_y^f = \pi_y^i + \hbar k_y$$

To cast these into time independent expressions we make use of eqn (5.6) to deduce a translation of the guiding centre

$$\frac{x_o^i - x_o^f}{\lambda^2} = k_y \qquad (5.9a) \qquad \frac{y_o^f - y_o^i}{\lambda^2} = k_x \qquad (5.9b)$$

where $\lambda^2 = \frac{\hbar}{m\omega_c} = \frac{\hbar c}{eH}$. This type of eqn. appears both in the present work (see later) and in a previous work on absorption cross section (Daugherty, J.K., Ventura, J., 1978). The crucial point is to realize that(5.7)&(5.8) are formally identical with the equations for a free electron, so that an exact knowledge of the translation of the guiding centre is fundamentally incompatible with energy conservation.

This apparent paradox is resolved by noting that in the quantum limit the conjugate variables x_o and y_o also obey a commutation relation

$$[x_o, y_o] = i\lambda^2$$

where $\lambda^2 = \frac{\hbar c}{eH}$ (this was first pointed out by M.H. Johnson and B.A. Lippmann, 1949). It means that there exist uncertainties in the x- and y- coordinates of the guiding centre such that $\Delta x_o \Delta y_o \gtrsim \frac{\lambda^2}{2}$. For a field 4×10^{12} gauss the quantity $\lambda \approx 10^{-10}$ cm ≈ radius of the 1st Landau orbit (non-relativistically). Equations(5.9)are then expected to hold only up to an uncertainty $\sim \frac{1}{\lambda}$. For a field 4×10^{12} gauss this quantity (in energy units) is $\frac{\hbar c}{\lambda} \approx 150$ keV which is of the same order as the energy separation of the Landau levels. Our interpretation is that it is precisely the large uncertainties associated with the initial and final guiding centres of the electron which allows the momentum equations(5.9)to hold alongside with the (exact) energy equation(5.7),thus giving rise to a photon of well-defined frequency.

The final point we wish to mention here is that equations(5.9)are

effectively describing a mechanism by which the momentum of the absorbed photon can finally be taken up by the source of the magnetic field (in our particular case, the neutron star). If we assume that the time of radiation Δt is large compared with the electron gyroperiod (this must be the case for sharp resonant radiation, because of the uncertainty principle $\Delta E \Delta t \sim \hbar$) the only net effect is a current $\underset{\sim}{j} = e\underset{\sim}{v}$ due to an overall translation in the mean position of the electron (guiding centre). The net impulse $\underset{\sim}{J}$ due to the $\underset{\sim}{j} \wedge \underset{\sim}{B}$ force on the electron is

$$J = \int F dt = \int \frac{-ev}{c} H dt = \frac{-eH}{c} \Delta r = \frac{-eH}{c} \frac{\hbar c}{eH} k = -\hbar k$$

By the principle of conservation of momentum of the entire system (electron + source of field) we then deduce that the source of the magnetic field suffers a reaction impulse $\hbar k$, which is precisely the momentum of the absorbed photon. In our particular situation, the source of the magnetic field is the massive neutron star - the broadening due to recoil is therefore negligible.

The conclusion of this discussion is that, despite large uncertainties implied by equations like(5.9),the frequencies of radiation associated with the system are expected to be well-defined, apart from the small uncertainties due to radiation damping and thermal motion in the z-direction.

5.4 The Calculation

Fig5.2shows how the compton scattering S-matrix may be expanded as a perturbation series in fine structure constant α (double lines indicate electron in bound states). The nth order term in the expansion consists of Feynman graphs of 2n vertices. We shall only be concerned with the zero order approximation, which consists of the two graphs (Fig5.3). In

this context the effects of the magnetic field on the photon via vacuum polarization is at least of 1st order (see Fig5.2 again) and can be ignored. Such effects have been considered elsewhere in the literature (see e.g. Ventura, J., 1979a, b; Mészáros, P. and Ventura, J., 1978,1979).

Lowest order perturbation theory can be justified only if the radiation energy density is much less than the magnetic energy density (i.e. the electromagnetic interaction can indeed be regarded as a perturbation). In the vicinity of the neutron star we can assume a radiation flux of 10^{37} ergs^{-1} (Lamb, F.K., Pethick, C.J., Pines, D., 1973) from an active emission region of 10^{15} cm^3 (Y.N. Gnedin, R.A. Sunyaev, 1973). This gives radiation energy density $\sim 10^{17}$ erg cm^{-3}, which is indeed << magnetic energy density = $\frac{B^2}{8\pi} \sim 10^{24}$erg cm^{-3} for a field H $\sim 10^{12}$ gauss.

Using the standard prescription of quantum electrodynamics we now write the formal expression for the S-matrix for compton scattering (units $\hbar$ = c = 1 are used)

$$S = \tfrac{1}{2}ie^2 \int \bar{\psi}_f(\underset{\sim}{x}') \not{A}(\underset{\sim}{k}',\underset{\sim}{x}') \, iS_F(\underset{\sim}{x}'-\underset{\sim}{x}) \not{A}(\underset{\sim}{k},\underset{\sim}{x}) \, \psi_i(\underset{\sim}{x}) d^4\underset{\sim}{x}' \, d^4\underset{\sim}{x}$$

$$+ \text{ (cross term)} \qquad (5.10)$$

where f = final, i = initial and $\underset{\sim}{x}' = (x',y',z',t')$, $\underset{\sim}{x} = (x,y,z,t)$ are 4-coordinates. $\not{A} = \gamma^\mu A_\mu$ where the γ's are Dirac matrices and

$$A_\mu(\underset{\sim}{k},\underset{\sim}{x}) = \varepsilon_\mu e^{-i\underset{\sim}{k}\cdot\underset{\sim}{x}} \qquad \text{(absorbed photon)}$$

$$A'_\mu(\underset{\sim}{k}',\underset{\sim}{x}') = \varepsilon'_\mu e^{i\underset{\sim}{k}'\cdot\underset{\sim}{x}'} \qquad \text{(emitted photon)}$$

ε's are polarization vectors and $\underset{\sim}{k} = (\omega, \vec{k})$ etc. In this convention the 1st term corresponds to the 1st Feynman diagram in Fig 5.3. The 2nd term (i.e. cross term) can be obtained from the first merely by the replacement $\underset{\sim}{k} \to -\underset{\sim}{k}'$ and $\underset{\sim}{\varepsilon} \to \underset{\sim}{\varepsilon}'$ and corresponds to the 2nd diagram in Fig. 5.3.

5.5 The Electron Propagator

$iS_F(\underset{\sim}{x}' - \underset{\sim}{x})$ in (5.10) is the virtual state, i.e. electron propagator, in a strong magnetic field. This has been calculated exactly (see, e.g R. Kaitna and P. Urban, 1964) but the expression is notoriously difficult to work with. Approximations are therefore inevitable. One such attempt (Canuto, V., Chiu, H.Y., Fassio-Canuto, L., 1969) uses the series expansion of the electron 2-point function in the presence of interaction

$$iS_F'(p) = \frac{i}{\not{p}-m} + \frac{i}{\not{p}-m}(-iV)\frac{i}{\not{p}-m} + \ldots$$

or $$S_F'(p) = \frac{1}{\not{p}-m-V}$$

However, this reasoning is incorrect because the electron is in the bound states of a classical potential.

The method adopted is as follows. Using the time-ordering approach we first write down the electron propagator formally as a sum of eigenstates in the energy representation. The degenerate degrees of freedom - spin s and, e.g. x-component of orbit centre, α, are respectively summed and integrated. The x-momentum p is integrated.

$$iS_F(\underset{\sim}{x}'-\underset{\sim}{x}) = \sum_{m,n}\sum_{s,s'}\int \{b,b^+\}\,\psi_m(p',s',\alpha',\underset{\sim}{x}')\,\bar{\psi}_n(p,s,\alpha,\underset{\sim}{x})$$

$$\frac{d\alpha d\alpha'}{2\pi\lambda^2}\,dp dp' \quad + \text{(positron term)}$$

We then postulate the following anticommutation relation between b^+ and b, the creation and annihilation operators for an electron in a strong magnetic field. $\delta = 2\pi\delta$

$$\{b,b^+\} = \lambda\,\delta(p-p')\,\delta(\alpha-\alpha')\delta_{ss'}\,\delta_{mn}$$

This gives

$$iS_F(\underset{\sim}{x}'-\underset{\sim}{x}) = \sum_n \sum_s \int \psi_n(p,s,\alpha,\underset{\sim}{x}')\, \bar{\psi}_n(p,s,\alpha,\underset{\sim}{x})\, \frac{d\alpha}{2\pi\lambda}\, \bar{d}p$$

$$+ \text{(positron term)} \qquad \bar{d}p = \frac{dp}{2\pi} \qquad (5.11)$$

At this point we make use of the assumption that electrons are only mildly relativistic (section 5.1), so that for a field strength $\sim 10^{12}$ gauss they do not occupy any energy levels higher than the first few. In this regime we can confidently make the following simplifications.

a) In (5.10) the initial and final states are taken to be the ground states with zero transverse energy n = 0. The cross-section is not drastically affected if we choose, in addition, to work in the rest frame of the initial electron. ψ_f and ψ_i may now be completely specified by the labelling $\psi_i = \psi_i(E=m, p=0,b)$, $\psi_f = \psi_f(E'=E_o', p',a)$. b and a are the initial and final x-coordinates of the guiding centre of the electron.

b) In (5.11) the summation over n is taken only from n = 0 to n = 2.

c) All but the highest order contribution in the positron term in (5.11) (corresponding to the time ordering t' < t) may be ignored.

Using the relativistic solutions ψ given by Johnson and Lippman, equation 54 (Johnson, M.H., Lippmann, B.A., 1949) we may now proceed to calculate the electron propagator relevant to the present approximation.

Define the matrices M_+ and M_- (electron projection operators)

$$M_{\pm}(q) = \frac{\not{q}+m}{2m}\, \frac{1+\gamma_5 \not{s}}{2}, \qquad s = \pm 1$$

where $\underset{\sim}{q} = (\varepsilon,0,0,q_z = q)$ and the two spin-vectors $\underset{\sim}{s}$ are determined by $\underset{\sim}{s}.\underset{\sim}{p} = 0$ and $\underset{\sim}{s}^2 = -1$. In the weak field limit $H \ll H_{cr}$ we can simply take $\varepsilon = m$ (so that $M_{\pm}(\underset{\sim}{q}) = M_{\pm}(q)$) since there are no resonances involved. Calculation of n = 0 in (5.11) is easy, and leads to the expression

$$\frac{1}{2\pi\lambda}\ e^{i\varepsilon_o(t-t')}\ \theta(t'-t)\ e^{-\frac{1}{4\lambda^2}[(x-x')^2+(y-y')^2]}\ e^{\frac{i(x'y-xy')}{2\lambda^2}}$$

$$x \int M_-(q)\ e^{iq(z'-z)}dq \quad .$$

where $\varepsilon_j = (q^2 + m^2 + 2j\varepsilon^2)^{\frac{1}{2}}$ $(\varepsilon^2 = \frac{H}{H_{cr}} m^2)$ is the energy of the propagator.

Calculation of n = 1, 2 involves the use of the identity

$$\int e^{-a^2} H_m(a+b)\ H_n(a+c)da = 2^n\sqrt{\pi}\ m!\ c^{n-m}\ L_m^{n-m}(-2bc) \text{ where } m \leq n.$$

Here H_m is the Hermite polynomial and L_m^{n-m} is the generalized Laguerre polynomial (see Gradshteyn, I.S., Ryzhik, I.M., 1965).

The sum of all three terms n = 0,1,2 gives the required expression

$$iS_F(\underset{\sim}{x}'-\underset{\sim}{x}) = \frac{1}{2\pi\lambda}\ \theta(t'-t)\ e^{-\frac{\xi}{2}}\ e^{\frac{i(x'y-xy')}{2\lambda^2}}$$

$$\{(I_o+I_1+I_2)\int M_-(q)\ e^{iq(z'-z)}dq + (J_1+J_2)\int M_+(q)\ e^{iq(z'-z)}dq\} \tag{5.12}$$

where $\xi = \frac{1}{2\lambda^2}[(x-x')^2 + (y-y')^2]$

and $I_o = e^{i\varepsilon_o(t-t')}$

$I_1 = (1-\xi)\ e^{i\varepsilon_1(t-t')}$ $\qquad J_1 = e^{i\varepsilon_1(t-t')}$

$I_2 = \frac{1}{2}(\xi^2 - 4\xi + 2)\ e^{i\varepsilon_2(t-t')}$ $\qquad J_2 = (1-\xi)\ e^{i\varepsilon_2(t-t')}$

The positron field contribution to the electron propagator can be calculated along exactly similar lines, and will not be repeated here.

5.6 The S-Matrix

The approximate electron propagator(5.12)is sufficiently simple to be used in the evaluation of the entire S-matrix (5.10).This involves 8 integrations over the space-time coordinates of the initial and final

electron. Consider initially the 1st term of (5.10). The z,z' integrations are trivial, and merely give the term

$$\int M_{\pm}(q)\ \delta(q+k_3)\ \delta(q+k_3'-p')\ dq$$
$$= M_{\pm}(\omega\cos\theta)\ \delta(\omega'\cos\theta'+p'-\omega\cos\theta)$$

where the photon 4-momentum k_μ : $k_o = k^o = \omega$, $k^1 = -k_1 = \omega\sin\theta\cos\phi$, $k^2 = -k_2 = \omega\sin\theta\sin\phi$, $k^3 = -k_3 = \omega\cos\theta$.

Particular attention is now drawn to the t integrations, as it involves time-ordering $\theta(t'-t)$ and gives rise to energy denominators $\frac{1}{m+\omega-\varepsilon_j}$. This gives infinite resonances when the energy of the absorbed photon equals the difference between the energy E = m of the initial electron and ε_j (j=0,1,2) of the electron propagator. As $q = k_z = \omega\cos\theta$ the condition for resonance is

$$\omega = [(\omega\cos\theta)^2 + m^2 + 2j\varepsilon^2]^{\frac{1}{2}} - m \qquad (5.13)$$

and thus varies with the 'pitch angle' θ.

Coming to the (x,y) & (x',y') integrations, we first calculate the contributions of the I_o and J_1 terms of the electron propagator (5.12) to the entire S-matrix. This is particularly simple, but (for reasons which will become clear shortly) in (5.12) we would like to replace ξ by $\mu\xi$ where μ is an arbitrary variable. This leads to the result

$$\frac{8\pi^2\lambda}{\mu+1}\exp-[\frac{a^2+b^2}{2\lambda^2} + \frac{2}{\mu+1}(k_2'-ik_1')a + \frac{\mu\lambda^2k_1'^2}{(\mu+1)^2} + \frac{\mu+2}{(\mu+1)^2}\lambda^2k_2'^2 - \frac{2i\lambda^2k_1'k_2'}{(\mu+1)^2}]$$

$$\exp\frac{\lambda^2}{4}[\frac{a+b}{\lambda^2} + \frac{2k_2'}{\mu+1} + i(\frac{\mu-1}{\mu+1}k_1'-k_1)]^2\ \delta(k_2'-k_2+\frac{a-b}{\lambda^2})$$

The I_o and J_1 contributions are then obtained by setting $\mu = 1$. Recall that b and a are respectively the initial and final x-coordinates of the electron. The physical significance of the δ-function has already been discussed in detail (section 5.3). The absence of the corresponding relation in the y-direction is due to the uncertainty principle - we

have chosen to work with eigenstates of x_o.

The I_1 and J_2 (equation 5.12) contribution to the S-matrix involves an extra factor $(1 - \xi)$. This simply gives $(1 + 2\frac{\partial}{\partial\mu})$ operating at the previous contribution. Similarly, the I_2 contribution gives $(2\frac{\partial^2}{\partial\mu^2} + 4\frac{\partial}{\partial\mu} + 1)$. All derivatives are finally evaluated at $\mu = 1$.

The final expression for the S-matrix (5.10) after taking into account similar calculations for the positron contribution to the electron propagator (5.12) then takes the form

$$S = \bar{u}_f(p', s = -1)\ [\not{\epsilon}'(sM_1 + pM_2)\not{\epsilon} + \not{\epsilon}(s'M_1' + p'M_2')\not{\epsilon}']\ u_i(p=0, s=-1) \qquad (5.14)$$

where the $\bar{u}$ and u are ordinary Dirac spinors and

$$s = A\left[\frac{1}{\varepsilon_o - m - \omega} + \frac{1}{\varepsilon_1 - m - \omega}\,\zeta + \frac{1}{\varepsilon_2 - m - \omega}\,\tfrac{1}{2}\zeta^2\right]$$

$$p = A\left[\frac{1}{\varepsilon_1 - m - \omega} + \frac{1}{\varepsilon_2 - m - \omega}\,\zeta\right]$$

where $A = 4\pi^2\lambda\ \exp\ \left[-\frac{a^2+b^2}{2\lambda^2} + (k_2' - ik_1')a + \frac{\lambda^2 k_1'^2}{4} + \frac{3}{4}\lambda^2 k_2'^2 - \frac{i\lambda^2 k_1' k_2'}{2}\right]$

$$\times \exp\ \frac{\lambda^2}{4}\left[\frac{a+b}{\lambda^2} + k_2' - ik_1\right]^2\ \delta(k_2' - k_2 + \tfrac{a-b}{\lambda^2})\ \delta(k_3 - p_3' - k_3')\ \delta(E_o' + \omega' - m - \omega)$$

and $\zeta = \frac{1}{2}[\lambda^2 k_2'^2 + \lambda^2 k_1 k_1' + i\lambda^2 k_2'(k_1 - k_1') + (a-b)(k_2' - ik_1')]$

The matrices M_1 and M_2 are

$$M_1 = \begin{pmatrix} 0 & 0 & 0 & 0 \\ 0 & 1 & 0 & \frac{-k_3}{2m} \\ 0 & 0 & 0 & 0 \\ 0 & \frac{k_3}{2m} & 0 & \frac{-\omega}{2m} \end{pmatrix}, \qquad M_2 = \begin{pmatrix} 1 & 0 & \frac{k_3}{2m} & 0 \\ 0 & 0 & 0 & 0 \\ \frac{-k_3}{2m} & 0 & \frac{-\omega}{2m} & 0 \\ 0 & 0 & 0 & 0 \end{pmatrix}$$

The 2nd term in (5.14) is obtained trivially from the 1st by the replacement $\underset{\sim}{k} \to -\underset{\sim}{k}'$ and $\underset{\sim}{\varepsilon} \to \underset{\sim}{\varepsilon}'$ (crossing symmetry).

5.7 The Cross Section

Two more steps remain in front - the square modulus of the S-matrix ($\propto$ transition probability) and the summation of photon polarizations. $|S|^2$ can be expanded in a straightforward but tedious manner. Alternatively we may rewrite $S = \bar{u}_f \, X \, u_i$ so that

$$|S|^2 = \mathrm{Tr}[X(u_i\bar{u}_i)\ \bar{X}\ (u_f\bar{u}_f)]$$

where $\bar{X} = \gamma^o\ X^+\ \gamma^o$ (Bjorken, J.D. and Drell, S.D., 1964). However, this technique does not seem to be particularly helpful here.

The δ-functions which enforce the 3 overall conservation laws in magnetic compton scattering must now be removed from $|S|^2$ by appropriate integrations. Energy-momentum δ-functions may be removed by integrating over the final state phase-space element of the electron and photon.

$$\int \frac{d^3k'}{2\omega'}\, dp'\ \delta(E_o'+\omega'-m-\omega)\,\delta\ (p'+k_z'-k_z)$$

p' integration sets $E_o' = [(k_z-k_z')^2 + m^2]^{\frac{1}{2}}$ and we are left with

$$\int \frac{k'^2 dk' d\Omega'}{2\,\omega'}\ \ \delta(E_o'+\omega'-m-\omega)$$

The technique here is to make use of the expression for E_o' above to deduce

$$E_o'\omega' d(E_o'+\omega') = [E_o'+\cos\theta'(\omega'\cos\theta'-\omega\cos\theta)]\ k'dk'$$

so that the phase space element becomes

$$\int \frac{E_o'k' d(E_o'+\omega') d\Omega'}{2[E_o'+\cos\theta'(\omega'\cos\theta'-\omega\cos\theta)]}\ \delta(E_o'+\omega'-m-\omega)$$

Integration is then straightforward, giving

$$\int \frac{E_o'\omega' d\Omega'}{2[m+\omega(1-\cos\theta\cos\theta')-\omega'(1-\cos^2\theta')]}$$

but with energy conservation

$$(\omega\cos\theta-\omega'\cos\theta')^2 + m^2 = (m+\omega-\omega')^2 \qquad (5.15)$$

The remaining δ-function may be removed trivially by integrating over the final state orbit centre a. In this way $|S|^2$ involves a basic exponential $\exp[\frac{-\lambda^2}{2}(\omega^2 sin^2\theta+\omega'^2 sin^2\theta')]$ multiplying into a sum of terms involving products of energy denominators and the terms r, r^2, r^*, $(r^*)^2$ where $r = \frac{1}{2}\lambda^2\omega\omega'\sin\theta\sin\theta' \; e^{i(\phi-\phi')}$. Since it is very complicated and of little relevance it will not be quoted here. However, drastic simplifications will happen when we finally integrate over the azimuthal angles ϕ and ϕ'.

Photon polarizations must now be dealt with. The polarization ought to be averaged over the initial state and summed over the final state. We have chosen to work in the Coulomb gauge ($\varepsilon^o = 0$) and hence the sum formula

$$\sum_{\varepsilon} \varepsilon_i \, \varepsilon_j^* = \delta_{ij} - \frac{k_i k_j}{k^2}$$

Azimuthal dependence of the cross section now takes the form $f(\phi'-\phi)$ (this can be anticipated simply from the symmetry of the process, and thus serves as a check to the calculation). More specifically $f(\phi'-\phi) \sim e^{im(\phi'-\phi)}$ where m is an integer. Such phase dependences are of no importance and may be removed by integrating over ϕ'. The final form of the compton cross section of an electron in a strong magnetic field then emerges as a function of the remaining angles θ,θ' and in units of the fine structure $\alpha^2 = (\frac{e^2}{\hbar c})^2$.

$$\int \frac{d\sigma}{d\Omega'} \, d\phi'$$

$$= \frac{2m+\omega-\omega'}{2\omega} \frac{\omega'}{m+\omega(1-\cos\theta\cos\theta')-\omega'\sin^2\theta'} \, e^{\frac{-\lambda^2}{2}(\omega^2\sin^2\theta+\omega'^2\sin^2\theta')}$$

$$\{(1+\cos^2\theta)(1+\cos^2\theta')\ [(\frac{\omega}{\varepsilon_1+m+\omega} - \alpha\mu)^2\ (\alpha_1^2+\alpha_2^2q^2) +$$

$$(\frac{\omega'}{\varepsilon_1'+m-\omega'} + \alpha\nu)^2\ (\alpha_1'^2+\alpha_2'^2q^2)] + \sin^2\theta\sin^2\theta'[(\frac{\omega}{\varepsilon_1+m+\omega} + \alpha\mu)^2$$

$$(\alpha_o^2+\alpha_1^2q^2+\tfrac{1}{4}\alpha_2^2q^4) + (\frac{-\omega'}{\varepsilon_1'+m-\omega'} + \alpha\nu)^2\ (\alpha_o'^2+\alpha_1'^2q^2+\tfrac{1}{4}\alpha_2'^2q^4)$$

$$+ 2(\frac{\omega}{\varepsilon_1+m+\omega} + \alpha\mu)\ (\frac{-\omega'}{\varepsilon_1'+m-\omega'} + \alpha\nu)\ \alpha_o\alpha_o']\} \qquad (5.16)$$

where $\alpha = \frac{\omega\cos\theta-\omega'\cos\theta'}{2m+\omega-\omega'}$, $\mu = \frac{\omega\cos\theta}{2\varepsilon_1}$, $\nu = \frac{-\omega'\cos\theta'}{2\varepsilon_1'}$

$$q = \tfrac{1}{2}\lambda^2\omega\omega'\sin\theta\sin\theta', \quad \alpha_i = \frac{1}{\varepsilon_i-m-\omega}, \quad \alpha_i' = \frac{1}{\varepsilon_i'-m+\omega'}$$

$$\varepsilon_i^2 = (\omega\cos\theta)^2 + m^2 + 2i\varepsilon^2, \quad \varepsilon_i'^2 = (\omega'\cos\theta')^2 + m^2 + 2i\varepsilon^2$$

Care must be taken as the expression for the cross section takes the present form(5.16) only when energy-momentum conservation(5.15) is enforced (this is due to the procedures used in integrating over final state phase space). Thus, of the four variables ω, θ, ω', θ' only 3 are independent. The low frequency limit ($\omega \to 0$) of(5.15) is a much simpler equation.

$$\omega' = 2\omega\ \sin^2\theta'$$

The low frequency and weak field limit of the above result (i.e. $\frac{\omega}{m} << 1$ and $\frac{H}{H_{cr}} << 1$) gives the magnetic Thomson cross section (Canuto, V. et al 1971)

$$\sigma = \int \frac{d\sigma}{d\Omega'}\, d\Omega' = \sigma_{Th}\ \{\sin^2\theta + \tfrac{1}{2}(1+\cos^2\theta)[(\frac{\omega}{\omega+\omega_c})^2 + (\frac{\omega}{\omega-\omega_c})^2]\ \} \qquad (5.17)$$

where $\sigma_{Th} = \frac{8\pi}{3}\frac{\alpha^2}{m^2}$ is the ordinary Thomson cross section.

It can be seen that for perpendicular propagation of the incident radiation, i.e. $\theta = \pi/2$, the cross-section for the O-mode photons (which correspond to the 1st term in σ) remains at the classical value $\sigma = \sigma_{Th}$ for all frequencies. However, the present relativistic calculation

reveals that there is departure from this behaviour at sufficiently high frequencies. In fact, as $\omega \to \omega_c$ the term $\alpha_1^2 q^2$ in (5.16) implies that $\sim$ 0.25% of the total compton resonance is due to resonances in the O-mode configuration.

5.8. Compton Resonances

The compton cross section shows infinite resonance structures when the condition (5.13) is satisfied. This is not so in reality because of the presence of damping mechanisms, the least of which is natural line broadening due to the finite lifetimes τ of the initial and final states. No calculation of such lifetimes is currently available, but an order of magnitude estimate of τ can be obtained from the synchrotron transition rate for the decay n=1 $\to$ n=0 (Daugherty, J.K., Ventura, J., 1978). This gives an energy width

$$\delta E \sim \frac{\hbar}{\tau} = \alpha\left(\frac{H}{H_{cr}}\right)^2 mc^2$$

For $H = 0.1\ H_{cr} = 4.414 \times 10^{12}$ gauss

$\delta E = 3.6 \times 10^{-2}$ keV.

Figs 5.4&5.5 show how the total cross section

$$\sigma = \int \frac{d\sigma}{d\Omega'}\, d\Omega'$$

varies with ω for the two incoming angles $\theta = 0^\circ$ and 30°, assuming a line-width given by the above estimate. On the same graphs (broken lines) we have also plotted the results of a similar calculation (Herold H., 1979). The difference between the two approximations used is marked in the low frequency regime. Polar diagram for scattering (variation of differential cross section w.r.t. θ and θ') is shown in Fig 5.6. Here the discrepancy between the two calculations is marked in the case for which the incoming angle $\theta \simeq 90^\circ$. This is because in the previous calculation the polar diagram was constructed only for the case in which the photon polarizations are parallel to the incoming plane.

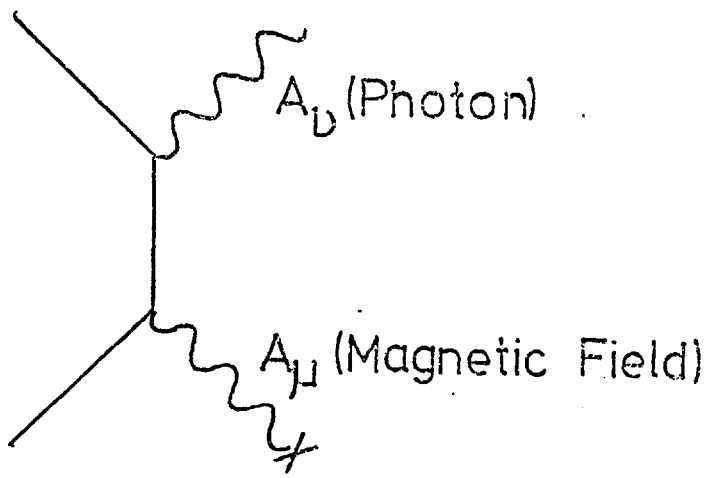
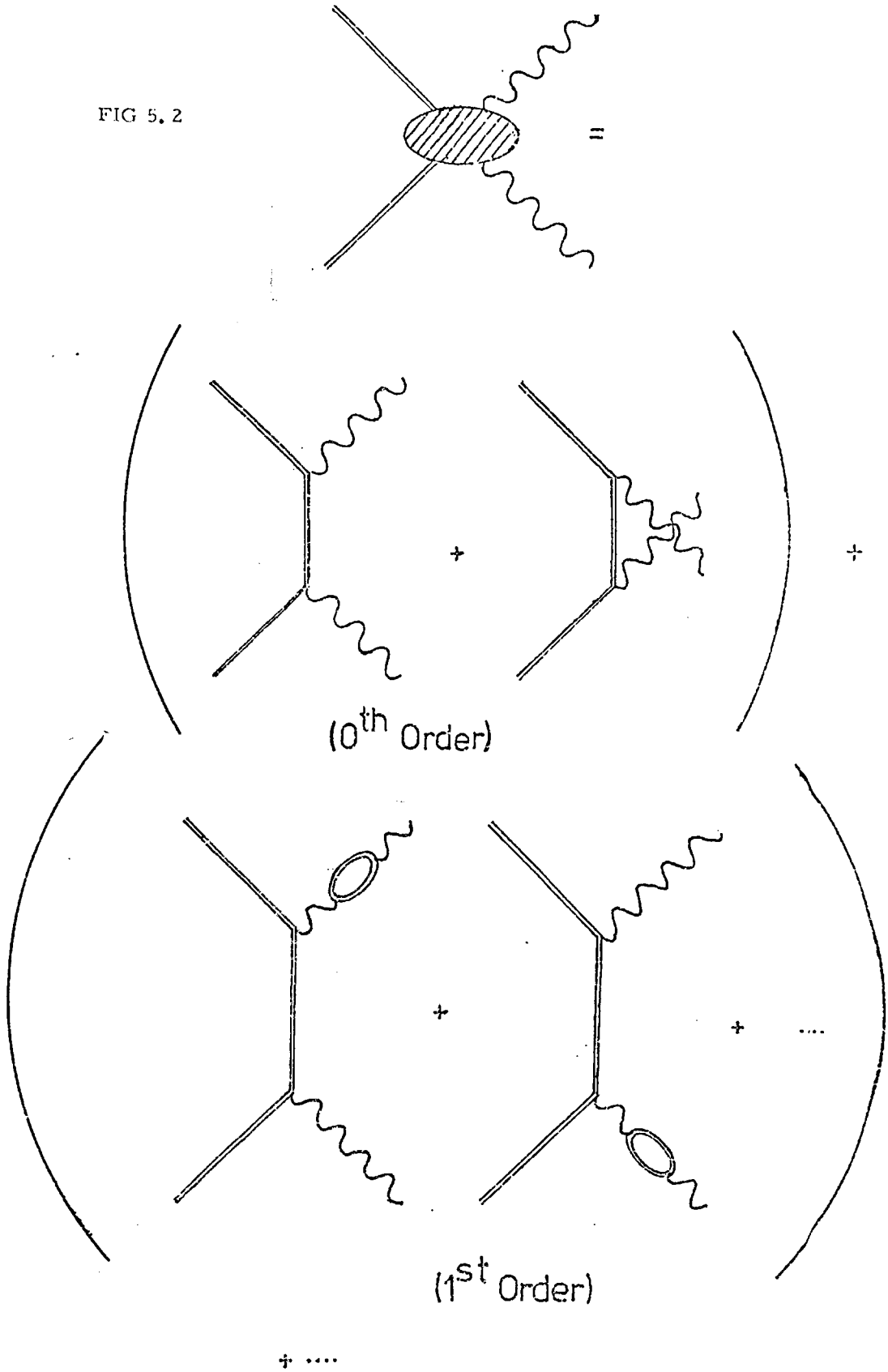


FIG 5. 1

FIG 5.2



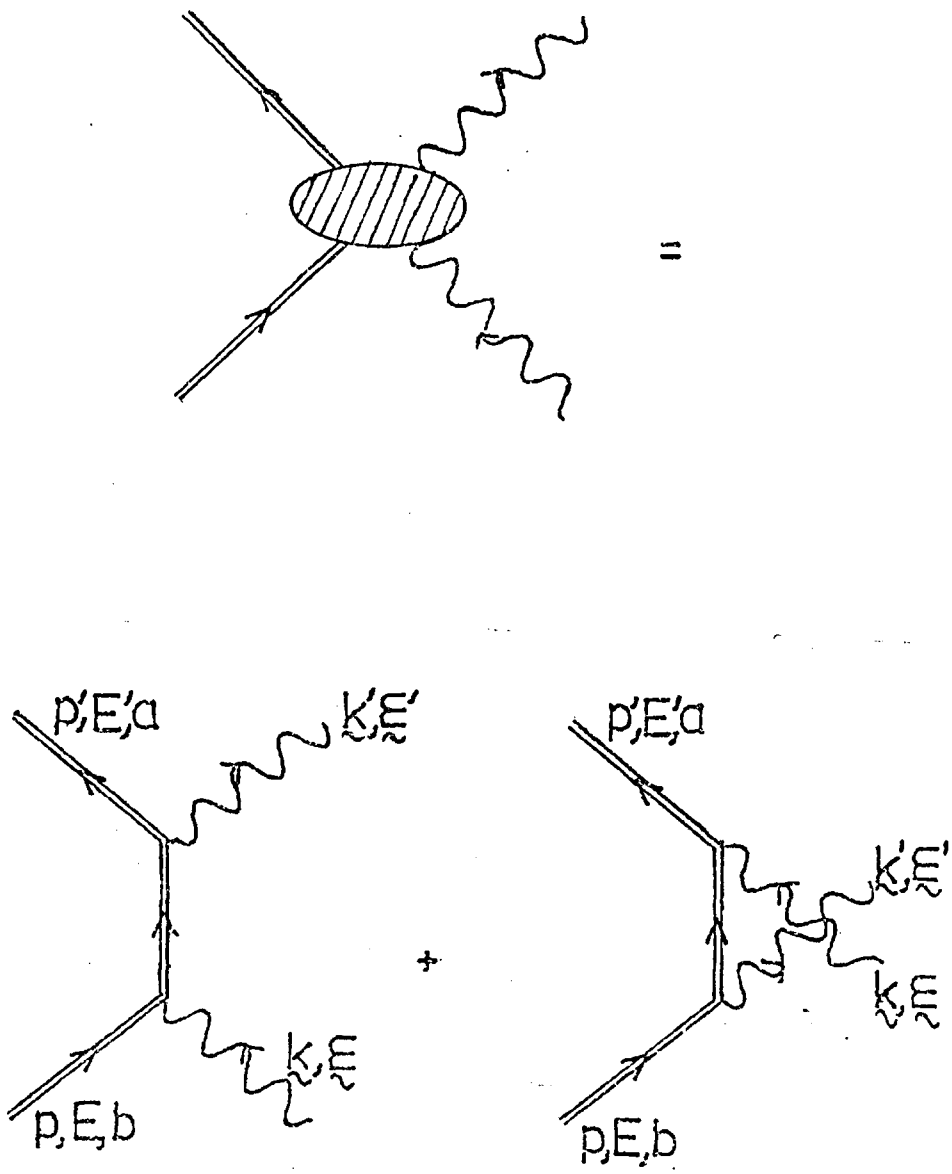


FIG 5. 3

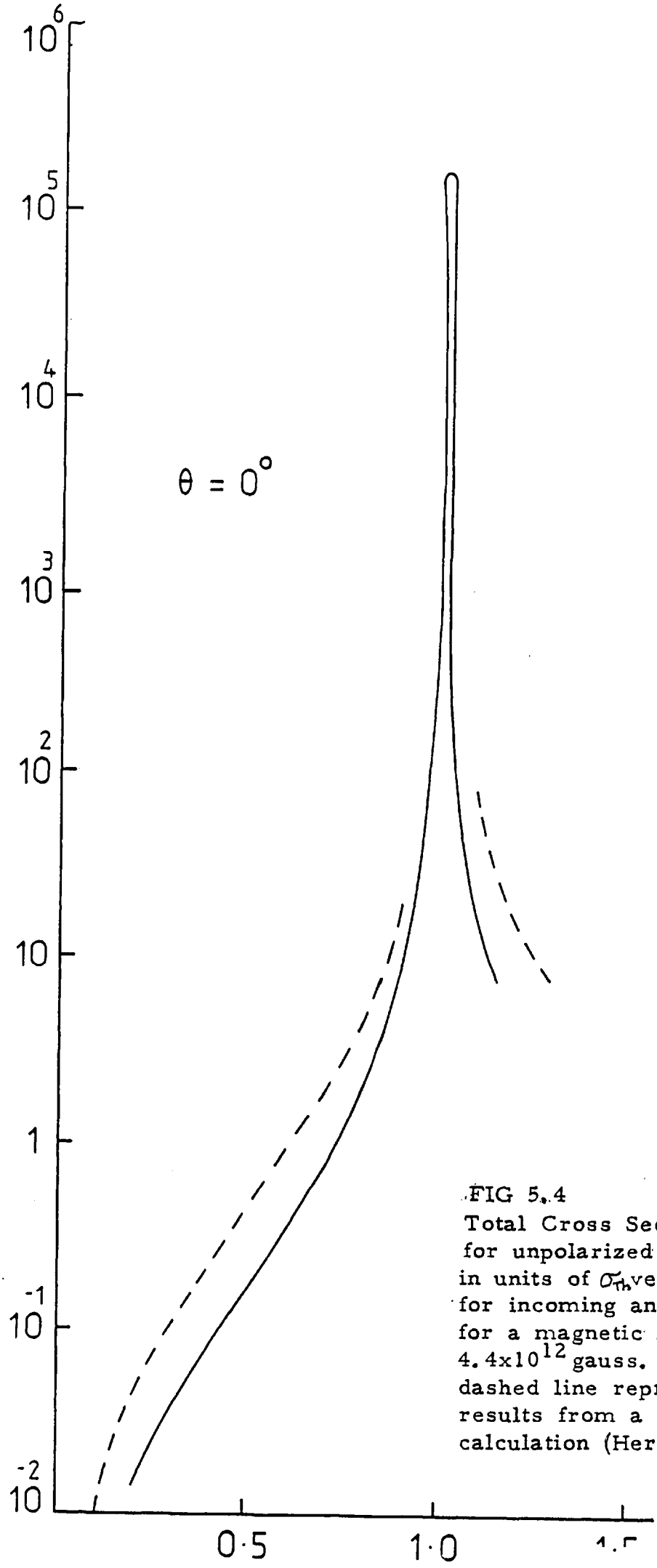


FIG 5.4
Total Cross Section $\sigma = \int \frac{d\sigma}{d\Omega'} d\Omega'$ for unpolarized radiation in units of σ_{Th} versus ω/ω_c for incoming angle Θ and for a magnetic field H= 4.4×10^{12} gauss. The dashed line represents results from a previous calculation (Herold 1979).

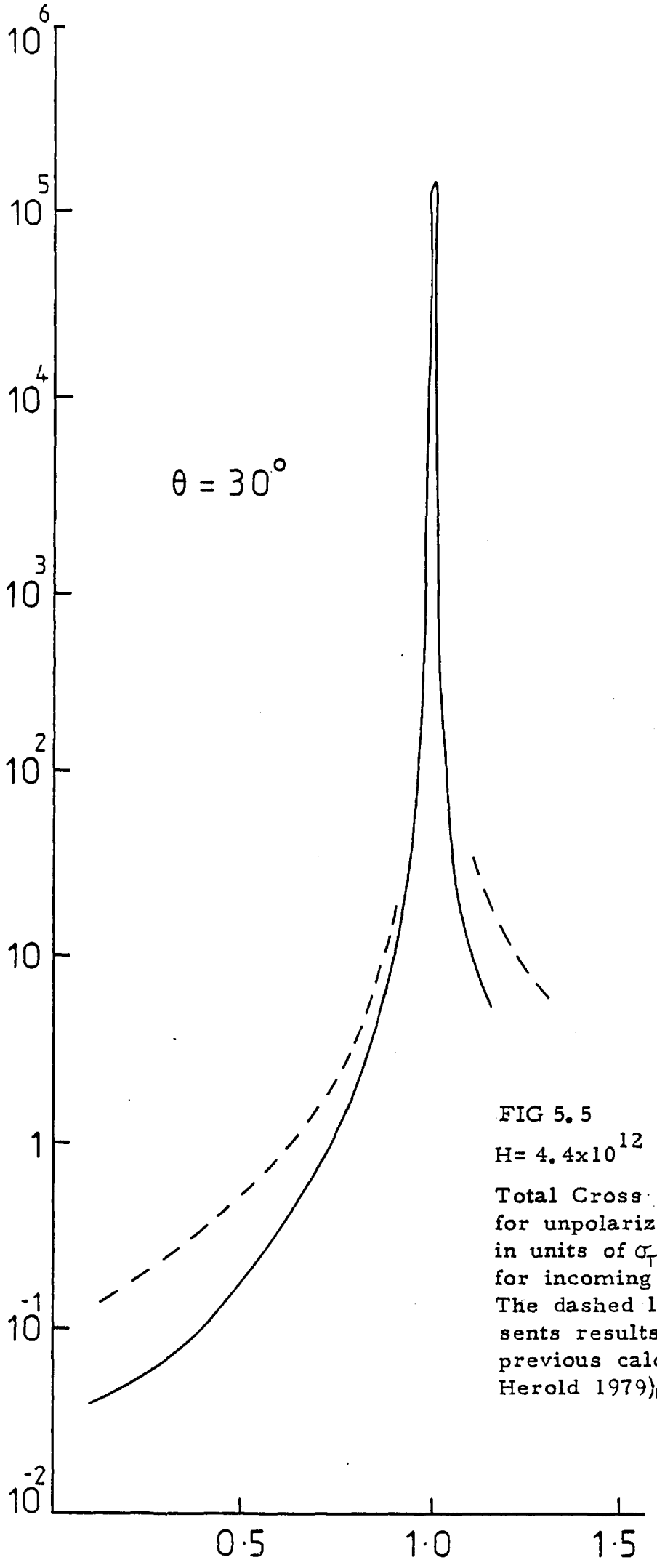


FIG 5.5

$H = 4.4 \times 10^{12}$ gauss

Total Cross Section $\sigma = \int \frac{d\sigma}{d\Omega'} d\Omega'$ for unpolarized radiation in units of σ_{Th} versus ω/ω_c for incoming angle $\theta = 30°$ The dashed line represents results of a previous calculation(Herold 1979).

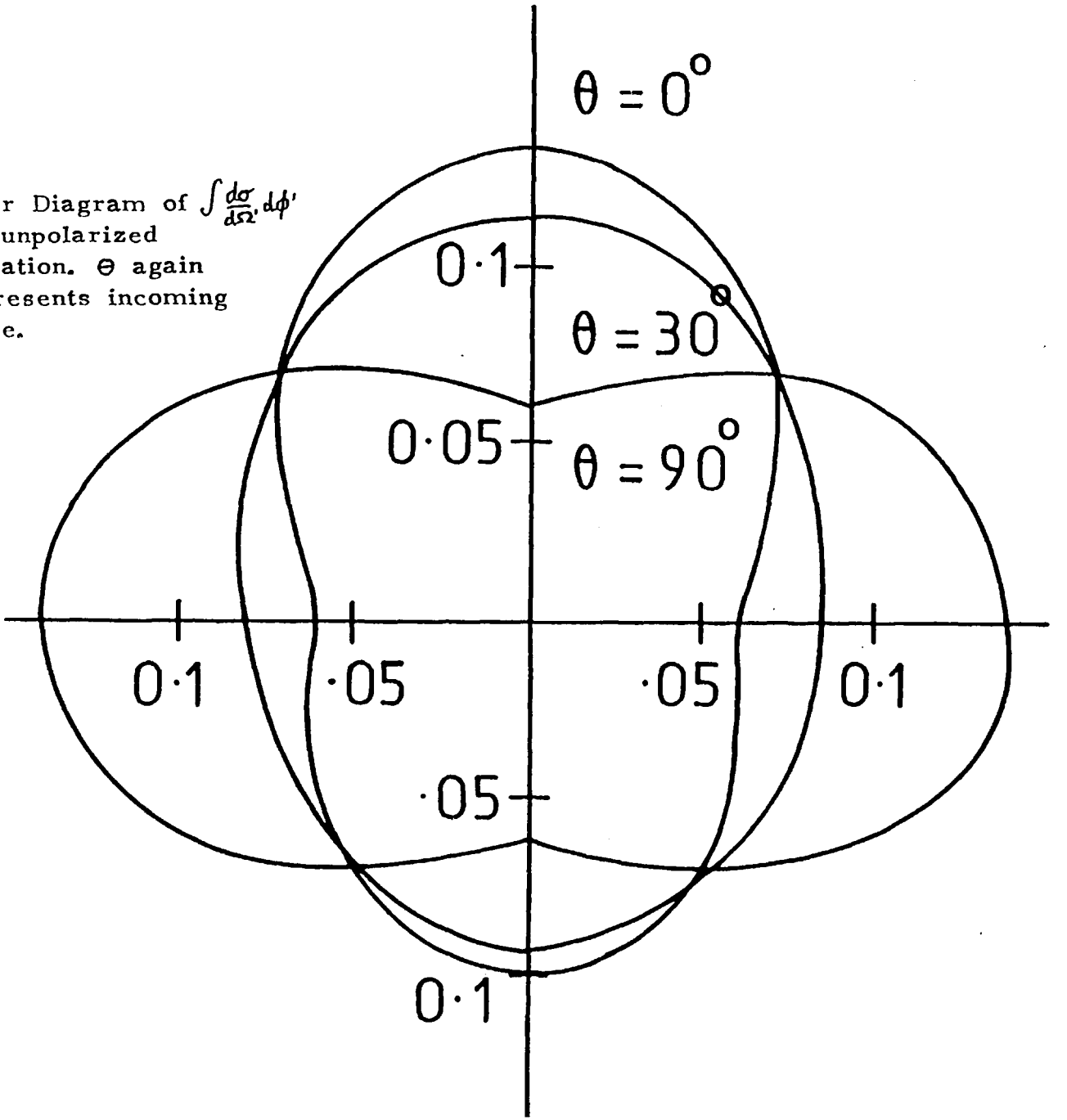


FIG 5.6 Polar Diagram of $\int \frac{d\sigma}{d\Omega'} d\phi'$ for unpolarized radiation. Θ again represents incoming angle.

CHAPTER 6

A REVISED CALCULATION OF THE BREMSSTRAHLUNG CROSS SECTION IN THE HIGH MAGNETIC FIELD OF PULSARS*

6.1 Introduction

As mentioned in Chapter 4, the present chapter deals with the emission of radiation by electron bremsstrahlung in an intense magnetic field. Earlier works have been done on the subject (see e.g. Canuto et al 1969), Lodenquai et al 1974, Virtamo et al 1975, Pavlov and Panov 1976). Regrettably, none of them appears to be satisfactory. The works by Canuto et al, Lodenquai et al were in error, as pointed out by Pavlov and Panov. However, as will be justified later on in our discussion (6.2), a non-trivial mistake was also discovered in the last work. The present work is therefore devoted to the search for a correct analytic expression of the bremsstrahlung transition rate (or cross-section). Use will be made of the simplified electron propagator for mildly relativistic electrons (Chapter5).

---

* Also accepted for publication in 'Astrophysics and Space Science'.

6.2 The S-Matrix

In the vicinity of the neutron star we assume a radiation flux of 10^{37} erg^{-1} (Lamb et al 1973) from an active emission region of 10^{15} cm^3 (Gnedin and Sunyaev 1973) with plasma no. density 10^{20}–10^{21} cm^{-3}. This gives the mean coulomb interaction energy density $\sim 2.10^9$ erg cm^{-3} and a radiation energy density $\sim 10^{17}$ erg cm^{-3}. Both are << magnetic energy density = $\frac{B^2}{8\pi} \sim 10^{24}$ erg cm^{-3} (for a field H $\sim 10^{12}$ gauss) so that lowest order perturbation theory (Fig 6.1) can be used for the calculation of the S-matrix. In units of $\hbar = c = 1$ this is

$$S = \tfrac{1}{2} ie^2 \int \bar{\psi}_f(\underline{x}') \not{A}(\underline{k},\underline{x}') iS_F(\underline{x}'-\underline{x}) \not{A}(\underline{x}) \psi_i(\underline{x}) \, d^4\underline{x} \, d^4\underline{x}' \qquad (6.1)$$

where f denotes final, i initial and $\underline{x}' = (x',y',z',t')$, $\underline{x} = (x,y,z,t)$ are 4-coordinates. $\not{A} = \gamma^\mu A_\mu$ where the γ's are Dirac matrices and

$$A_\mu(\underline{k},\underline{x}') = \varepsilon_\mu e^{i\underline{k}\cdot\underline{x}'} \qquad \text{(emitted photon)}$$

$$A_\mu(\underline{x}) = \frac{Ze}{r}, \ \mu = 0 \qquad \text{(Coulomb interaction)}$$

the ε's are polarization vectors and $\underline{k} = (\omega,\vec{k})$ etc. (In addition we choose to work in the rest frame of the proton, so that there is only a static coulomb interaction between the electron and the proton). In this convention the first term of (6.1) corresponds to the first Feynman diagram in Fig 6.1. The second term (i.e. cross term) can be obtained from the first merely by the replacement $\underline{k} \to -\underline{k}'$, $\underline{\varepsilon} \to \underline{\varepsilon}'$ and corresponds to

the second diagram of Fig.6.1.

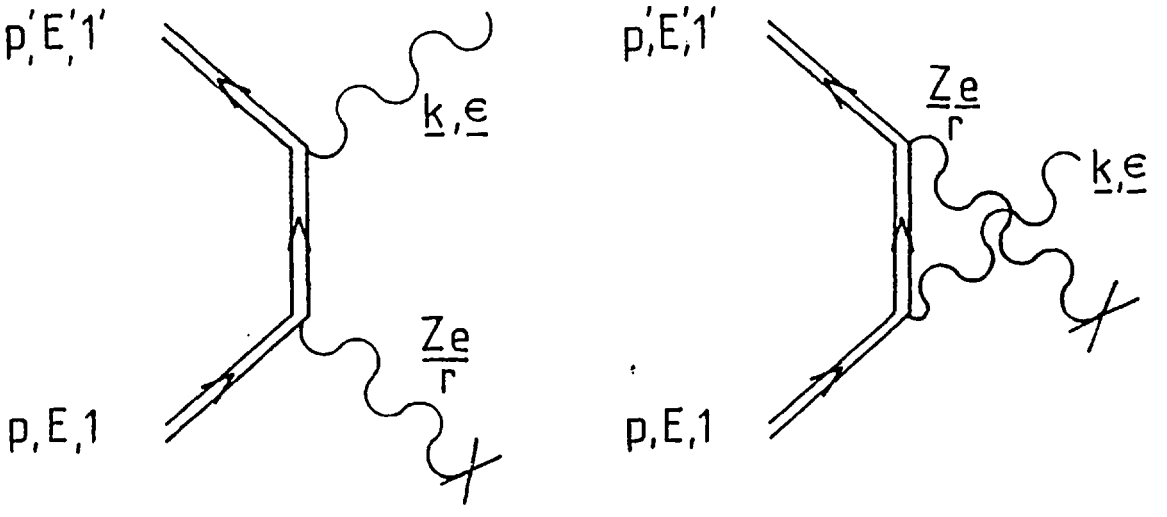


FIG 6.1

As already explained in section 6.1 we are interested in mildly relativistic electrons and hence the following transitions :

Case (1) $\psi_i = \psi_i(E_1, p_z = p, \ell, s = \pm 1)$
$\psi_f = \psi_f(E_0', p_z' = p', \ell', s' = -1)$

Case (2) $\psi_i = \psi_i(E_0, p_z = p, \ell, s = -1)$
$\psi_f = \psi_f(E_0', p_z' = p', \ell', s' = -1)$

where $E_j = (p_z^2 + m^2 + 2j\epsilon^2)^{\frac{1}{2}}$, $(\epsilon^2 = \frac{H}{H_{cr}} m^2)$ is the energy of the state, ℓ is the angular momentum quantum no. and s is the spin. (These relativistic energy states are given in eqns (54) and (45) of Johnson and Lippmann (1949)). The second case corresponds to continuum soft X-ray emission which is accompanied by no transitions between Landau levels. In this section we calculate the S-matrix for states with the (degenerate) angular momentum labels $\ell = \ell' = 0$. Generalisation to

include transitions between finite ℓ's is rather trivial, and will be discussed in the next section.

The term $iS_F(\underline{x}'-\underline{x})$ in (6.1) is the virtual state, i.e. electron propagator in a strong magnetic field. For a mildly relativistic electron which can occupy no more than the first few Landau levels, it was shown that (Lieu 1980)

$$iS_F(\underline{x}'-\underline{x}) = \frac{1}{2\pi\lambda^2}\,\theta(t'-t)\,e^{-\frac{\xi}{2}}\,e^{\frac{i(x'y-xy')}{2\lambda^2}} \times\left\{(I_0+I_1+I_2)\int M_-(q_f)\,e^{iq_f(z'-z)}\,dq_f + (J_1+J_2)\int M_+(q_f)\,e^{iq_f(z'-z)}\,dq_f\right\} \tag{6.2}$$

where $\xi = \frac{1}{2\lambda^2}\left[(x-x')^2+(y-y')^2\right]$

and $I_0 = e^{i\varepsilon_0(t-t')}$ $\qquad J_1 = e^{i\epsilon_1(t-t')}$

$I_1 = (1-\xi)\,e^{i\epsilon_1(t-t')}$ $\qquad J_2 = (1-\xi)\,e^{i\epsilon_2(t-t')}$

$I_2 = \frac{1}{2}(\xi^2-4\xi+2)\,e^{i\epsilon_2(t-t')}$

where $\varepsilon_j = (q^2 + m^2 + 2j\varepsilon^2)^{\frac{1}{2}}$ is the energy of the propagator.

To proceed to actual computation we first perform the 8 space-time integrations $\int d^4\underline{x}\, d^4\underline{x}'$ in (6.1). The t,t' integrations give rise to energy denominators for the particular time ordering $\theta(t'-t)$. These are, respectively, α_j and α_j' for the two diagrams of Fig 6.1, where

$$\alpha_j = \frac{2m}{2\omega(m-p'\cos\theta)-\omega^2\cos^2\theta-2j\epsilon^2}$$

$$\alpha_j' = \frac{2m}{2(1-j)\epsilon^2-\omega^2\cos^2\theta-2\omega(m-p\cos\theta)} \tag{6.3}$$

Among these coefficients, α_1 and α_0 are responsible for the resonances in the cross section. When the z-momenta p and p' are <u>small</u> they have approximately the same resonance frequency at $\omega = \omega_c$.

The spatial integrations are most easily done if we analyse

the $\frac{1}{r}$ potential into its Fourier components

$$\frac{1}{4\pi r} = \int \frac{e^{i\vec{q}\cdot\vec{r}}}{q^2} d^3\vec{q}$$

The spectral component $e^{i\vec{q}.\vec{r}}$ has an intensity $\frac{1}{q^2}$, which must be summed over all components in $\int \frac{d^3q}{q^2}$ immediately after the spatial integrations are complete. The procedures adopted by Pavlov and Panov (1976) is incorrect as the summation was done after they obtained the transition probability $|S|^2$.

z,z' integrations now give rise to momentum conservation $\delta(p' + k_z - p - q_z)$.

Coming to the (x,y), (x',y') integrations, it is convenient to define a parameter ζ as

$$\zeta = \exp\left\{-\frac{\lambda^2}{2}\left[(q_x^2+q_y^2)+(k_x^2+k_y^2)-(q_x-iq_y)(k_x+ik_y)\right]\right\} \times \delta(E-E'-\hbar\omega)$$

In this notation the contributions from the I_o and J_1 terms of the electron propagator (2) to the first diagram of Fig 6.1 for the two transitions we are interested in (cases 1 and 2 outlined earlier) are, respectively

$$-4i\pi^2\lambda(k_x+ik_y)\zeta$$

and (6.4a)

$$4\pi^2\zeta$$

Similarly, the I_1 and J_2 terms give

$$2i\pi^2\left[2\lambda(q_x+iq_y)-\lambda^3(q_x+iq_y)(k_x^2+k_y^2)\right]\zeta$$

$$2\pi^2\lambda^2(q_x+iq_y)(k_x-ik_y)\zeta \qquad (6.4b)$$

and the I_2 contribution gives

$$\frac{1}{2} i\pi^2 \lambda^3 (k_x - i k_y)(q_x + i q_y)^2 \left[4 - \lambda^2 (k_x^2 + k_y^2)\right] \zeta$$

$$\frac{1}{2} \pi^2 \lambda^4 (k_x - i k_y)^2 (q_x + i q_y)^2 \zeta \qquad (6.4c)$$

Results for the second diagram of Fig 6.1 can be obtained from the ones above by the replacement $\vec{k} \to -\vec{k}$ and $\vec{q} \to -\vec{q}$.

As explained earlier on, we must now integrate over all possible values of $\vec{q}$, the momentum transfer during coulomb collision with the ion.

The q_z integration is trivial, as it merely involves

$$\int \frac{dq_z}{q^2 + q_z^2} \delta(p' + k_z - p - q_z) = \frac{1}{q^2 + a^2}$$

where $q^2 = q_x^2 + q_y^2$ and $a = p' + k_z - p$ is the amount of z-momentum the electron acquired from the ion. The only remaining δ- function is the one in energy space in (6.4). It is a well-recognised fact that in bremsstrahlung process the electron plays a role in energy conservation and the ion in momentum conservation.

More explicitly, the energy conservation in (6.4) implies that

$$(p^2 + m^2 + 2j\varepsilon^2)^{\frac{1}{2}} = (p'^2 + m^2)^{\frac{1}{2}} + \hbar\omega \qquad (6.5)$$

where $j = 1, 0$ depending on whether we are in case (1) or case (2). From this we can solve for p', momentum of the final state electron

$$p'^2 = \left[(p^2 + m^2 + 2j\varepsilon^2)^{\frac{1}{2}} - \hbar\omega\right]^2 - m^2 \qquad (6.6)$$

Thus, for a given value of the initial momentum $p_z = p$, there are two values of p' having opposite signs w.r.t. each other. The one which bears the same sign as p corresponds to forward scattering. The one which bears the opposite sign corresponds to backward scattering (max. momentum transfer).

q_x and q_y integrations prove to be the most difficult part of the entire calculation. Unfortunately, the final cross section is rather sensitive to the way in which these integrations are done. The simplest integral involves

$$\int \frac{\zeta}{q_x^2 + q_y^2} \, dq_x \, dq_y$$

which becomes, if we extract only the relevant information from ζ

$$\int \frac{e^{-\frac{\lambda^2}{2}(q_x^2+q_y^2)} \, e^{\frac{\lambda^2}{2}(q_x - iq_y)(k_x + ik_y)}}{q^2 + a^2} \, dq_x \, dq_y$$

Firstly, the sinusoidal component $e^{\frac{i\lambda^2}{2}(q_x k_y - q_y k_x)}$ has a minimum period of $\frac{4\pi}{\lambda^2 k}$, whilst the half-width of the gaussian is $\sim \frac{\sqrt{2}}{\lambda}$. For a pulsar field $H \sim 4 \times 10^{12}$ gauss and photon energy $\hbar\omega \lesssim 50$ keV the minimum ratio of the former to the latter is ~ 30. This means that the sinusoidal component effectively stays at unity throughout the finite range of the gaussian. The remaining integral we express in polar coordinates

$$\int_0^{2\pi} \int_0^{\infty} \frac{e^{-\frac{\lambda^2 q^2}{2}} \, e^{\frac{\lambda^2 \beta q}{2}}}{q^2 + a^2} \, q \, dq \, d\phi$$

where $\beta = k_x \cos\phi + k_y \sin\phi$. Expanding the exponential, we get

$$\int_0^{2\pi} d\phi \int_0^{\infty} q \, dq \, \frac{e^{-\frac{\lambda^2 q^2}{2}}}{q^2 + a^2} \left(1 + \frac{\lambda^2 \beta q}{2} + \cdots\right)$$

If we calculate the $(2n-1)^{th}$ term of the q- integration ($n = 1,2,\ldots$), e.g.

$$n=1 \qquad \int_0^\infty q\,dq\, \frac{e^{-\frac{\lambda^2 q^2}{2}}}{q^2+a^2} = \frac{1}{2}\, e^{\frac{\lambda^2 a^2}{2}}\, E_1\left(\frac{\lambda^2 a^2}{2}\right)$$

$$n=3 \qquad \frac{\lambda^2\beta^2}{2!4}\int q^3\,dq\, \frac{e^{-\frac{\lambda^2 q^2}{2}}}{q^2+a^2} = \frac{\lambda^2\beta^2}{2!4}\left[1-\frac{\lambda^2 a^2}{2}\, e^{\frac{\lambda^2 a^2}{2}}\, E_1\left(\frac{\lambda^2 a^2}{2}\right)\right]$$

and so on. Here $E_1(z)$ is an exponential integral function defined as

$$E_1(z) = \int_z^\infty \frac{e^{-t}}{t}\, dt$$

For large λa, $e^{\frac{\lambda^2 a^2}{2}}\, E_1\left(\frac{\lambda^2 a^2}{2}\right) \sim \frac{2}{\lambda^2 a^2}$. Thus the first term $\sim \frac{2}{\lambda^2 a^2} \to 0$, the 3rd term $\sim \lambda^2\beta^2$, the 5th term $\sim \lambda^4\beta^4.\lambda^2 a^2$. Hence the summation over odd values of n is divergent for large λa. It can be shown that the series for even n also exhibits the same behaviour.

To resolve this difficulty one has to notice that in allowing λa and the upper limit of the q- integration to be ∞ one has implicitly assumed that the theory remains valid for indefinitely large momentum transfer between the electron and the ion. For a given magnetic field strength there should always exist an upper bound for q beyond which the Born approximation breaks down and the Coulomb interaction can no longer be considered as a perturbation.

The momentum transfer q is related to the impact parameter b by the relation $q.b \sim \hbar$ (p.248, Heitler, 1954). For electrons in a magnetic field there exists a minimum uncertainty $\sim \lambda = \left(\frac{\hbar c}{eH}\right)^{\frac{1}{2}}$ in the position of the guiding centre due to the commutation relation

$$[\hat{x}_o, \hat{y}_o] = i\lambda^2$$

between the measurements $\hat{x}_o, \hat{y}_o$ of the x and y coordinates of the guiding centre (Johnson and Lippmann 1949). Since the radius of the electron orbit carries no uncertainty (because the energy levels are well-defined) there is the same uncertainty λ in locating the position of the electron on the orbit. For a given magnetic field this immediately sets a lower bound to the impact parameter $b_{min} \sim \lambda$ and hence an upper bound to the momentum transfer $p_{max} \sim \frac{\hbar}{\lambda}$ since the electron cannot aim at the ion to a precision better than λ. In our present notation the q-integration is thus modified to

$$\int_0^{2\pi} \int_0^{\lambda^{-1}} \frac{e^{-\frac{\lambda^2 q^2}{2}} e^{\frac{\lambda^2 \beta q}{2}}}{q^2 + a^2} \, q \, dq \, d\phi$$

where also $a \lesssim \frac{1}{\lambda}$. It can be shown that the spurious terms introduced by the cutoff are divergent and carry the opposite sign to the original divergent quantities. The above integral is finite. To order $\lambda^2\omega^2$ the result is

$$\pi \, e^{\frac{\lambda^2 a^2}{2}} \left[E_1\left(\frac{\lambda^2 a^2}{2}\right) - E_1\left(\frac{1 + \lambda^2 a^2}{2}\right)\right]$$

and is therefore independent of β.

In the limit of low momentum transfer $\lambda a << 1$ it can be seen that the first term diverges logarithmically as $\ell n(\frac{\lambda^2 a^2}{2})$. This leads one to suspect, as before, that there must exist a minimum value for the momentum transfer corresponding to a maximum value for the impact parameter. The latter is usually taken to be the Debye shielding length (Brussard et al 1962)

$$\lambda_D = \left(\frac{\varepsilon_o kT}{ne^2}\right)^{\frac{1}{2}}$$

For electron temp. kT $\sim$ 10 keV and plasma no. density $n \sim 10^{21}\,cm^{-3}$, λ_D $\sim 5.5 \times 10^{-6}$ cm (this is >> radius of the first Landau orbit $\sim 10^{-10}$ cm,

so that there is no additional quantum effects due to degeneracy of the plasma). However, Pavlov and Panov (1976) argued that in an extreme situation when we have (1) a sufficiently tenuous plasma and (2) high frequencies ($\omega >> \omega_p$), the max. impact parameter should not be determined by λ_D, but by the distance $\lambda_\omega \sim (\frac{kT}{m\omega^2})^{\frac{1}{2}}$ that the electron traverses during one period of oscillation of the em-wave. If we write

$$\frac{\omega}{\omega_p} = 2.67 \times 10^3 \, n_{20}^{-\frac{1}{2}} \, (\hbar\omega/keV)$$

then it is clear that the plasma radiation system in the polar region of X-ray pulsars certainly possesses the second characteristic (2) outlined above but not the first (1), since a plasma of no. density $n \sim 10^{20-21}$ cm^{-3} cannot be regarded as tenuous. The question remains open, therefore, as regards which lower impact parameter one should use in our particular situation. However, for a field $H \sim 4.10^{12}$ gauss and electron temp. kT $\sim$ 10 keV, $\lambda_\omega = 4.4 \times 10^{-11}$ cm $<< \lambda_D$. It can only be safer to choose to work with the larger one.

It remains to multiply all γ-matrices in (6.1) together to form the S-matrix. If we choose to work in the Coulomb gauge $\varepsilon_o = \varepsilon^o = o$ so that $\not{\varepsilon} = \gamma^\mu \varepsilon_\mu = \gamma^i \varepsilon_i$, this is straightforward and we give only the final results.

Case 1 $\quad j = 1 \longrightarrow j = 0 \;,\; S = +1 \longrightarrow S = -1$

$$S = [(-\alpha' + \alpha_I + \alpha\beta^2)\, 4\alpha_1 + (\alpha - \alpha_I - \alpha'\beta^2)\, 4\alpha_0' - 4\beta^2\alpha'\alpha_1] \times I(\varepsilon_1 + i\varepsilon_2) - (2\beta\alpha_1 + 4\beta\alpha_0' + 4\beta^3\alpha_1)\, I\, \varepsilon_3 \qquad (6.7a)$$

$$j = 1 \longrightarrow j = 0 \;,\; S = -1 \longrightarrow S = -1$$

$$S = 4(\beta\alpha_1 + \beta\alpha_0' + \beta^3\alpha_1)\, I(\varepsilon_1 + i\varepsilon_2) + 2[2(\alpha' + \alpha_I)\alpha_1 + 2(\alpha + \alpha_I)\alpha_0' + \alpha'\beta^2\alpha_1]\, I(\lambda\omega\sin\theta)\, \varepsilon_3 \qquad (6.7b)$$

Case 2

$$j = 0 \rightarrow j = 0 \ , \quad S = -1 \rightarrow S = -1$$

$$S = \left\{ \left[(\alpha_I + \alpha') + \frac{\alpha \xi^2}{2m^2} \right] 4\alpha_0 + \left[(\alpha + \alpha_I) + \frac{\alpha' \xi^2}{2m^2} \right] 4\alpha_0' \right\} I \, \xi_3 \qquad (6.7c)$$

where $$\alpha = \frac{p}{2m} \ , \ \alpha' = \frac{p'}{2m} \ , \ \alpha_I = \frac{p' + \omega \cos\theta}{2m} \ , \ \beta = \frac{\sqrt{2}\,\xi}{2m} \qquad (6.8)$$

$$I = \frac{1}{2} e^{\frac{\lambda^2 a^2}{2}} \left[E_1\left(\frac{\lambda^2 a^2}{2}\right) - E_1\left(\frac{1 \mp \lambda^2 a^2}{2}\right) \right] e^{-\frac{\lambda^2 \omega^2 \sin^2\theta}{2}} \qquad (6.9)$$

and α_i, α_i' are defined as in (6.3).

6.3 Bremsstrahlung Cross Section

The cross section for electron bremsstrahlung emission in an external magnetic field is now obtained by taking $|S|^2$ and summing over all available density of states. The final state phase space element of the electron and the emitted photon is

$$2\pi\lambda^2 \sum_{j'} \sum_{\ell'} \int \frac{d^3k}{2\omega} \, dp' \, \delta(E - E' - \hbar\omega)$$

The δ-function which enforces overall energy conservation between the electron and photon may be removed by integrating over p'. Using the fact that $dp' = \frac{E'dE'}{p'}$ the phase-space element then simplifies to

$$2\pi\lambda^2 \sum_{j'} \sum_{\ell'} \frac{E'}{p'} \int \frac{d^3k}{2\omega}$$

but with energy conservation (6.5).

The summation sign $\sum_{j'}$ above is only there for the sake of formality, since we know that there is only one final state j' = 0. Summation over all available angular momentum states ℓ' of the final

electron is now essential. The density of states factor $2\pi\lambda^2$ is due to previous authors (J. Virtamo et al 1975) whose argument is as follows. The eigenvalue of the distance R from the z-axis of the guiding centre of an electron with angular momentum ℓ is $R = (2\ell+1)^{\frac{1}{2}}\lambda$. If we assume that the degenerate ℓ-levels are occupied with equal probability then the no. of electrons in the ℓ-state is proportional to the area $2\pi RdR = 2\pi\lambda^2 d\ell$. In the present normalisation of quantum states the constant of proportionality may be taken to be unity.

Coming now to $\sum_{\ell'}$, we make use of the fact that states with finite ℓ are related to the $\ell = 0$ ones by the relation

$$\psi(E_j, p, \ell) = (2^{\ell}\ell!)^{-\frac{1}{2}}\left(\frac{x-iy}{\lambda}\right)^{\ell}\psi(E_j, p, \ell=0)$$

(see eqn.45 Johnson et al 1949). Careful examination of eqn(6.1) for the S-matrix reveals that, for the first term, the result of the integration involving $\psi_f(\ell' \neq 0)$ simply equals $\frac{i}{\lambda}(2^{\ell'}\ell'!)^{-\frac{1}{2}}\left(\frac{\partial}{\partial K_x} - i\frac{\partial}{\partial K_y}\right)^{\ell'}$ operating on the expressions in(6.4) which we obtained before the q-integration. The result for the second term in(6.1) may then be obtained by the replacement $\vec{k} \to -\vec{k}$, $\vec{q} \to -\vec{q}$. In any case the above procedures introduce essentially two types of integrals

$$\int_0^{2\pi}\int_0^{\lambda^{-1}} \lambda^m (k_x \pm i k_y)^m \frac{e^{-\frac{\lambda^2 q^2}{2}}}{q^2+a^2}\, q\, dq\, d\phi \qquad (6.10a)$$

$$\int_0^{2\pi}\int_0^{\lambda^{-1}} \lambda^m (q_x \pm i q_y)^m \frac{e^{-\frac{\lambda^2 q^2}{2}}}{q^2+a^2}\, q\, dq\, d\phi \qquad (6.10b)$$

In the first integral the factor $\lambda^m(k_x \pm ik_y)^m$ can be taken outside. To order $\lambda\omega$ only the terms with m = 0,1 remain. The second integral vanishes for all values of m except m = 0. In either cases the integrals are no different from the ones that we just dealt with.

Using the same method, the initial state must also be

averaged over all possible angular momentum ℓ (and all possible energies E_j, j = 0,1). In passing we stress that the entire summation procedure must be done after we have taken the square modulus of the S-matrix, i.e.

$$2\pi\lambda^2 \sum_j \sum_\ell \sum_{\ell'} |S|^2$$

It turns out that, if we accept the m = 0,1 terms in (6.10) as the only non-vanishing terms (to order $\lambda\omega$) then it is not necessary to consider any transitions other than the following ones : $\ell = 0$, $\ell' = 0$; $\ell = 0$, $\ell' = 1$; $\ell = 1$, $\ell' = 0$; $\ell = 1$, $\ell' = 1$.

Finally, we include a factor $\frac{m}{p} = \frac{1}{v}$ for the incident electron flux, since the normalisation is over 1 electron and 1 ion per unit volume of space. We present below $\sigma_{\parallel}$ and $\sigma_{\perp}$ respectively, the cross sections for two independent polarisations (direction of the electric field) of the emitted radiation.

$$\vec{\varepsilon}_{\parallel} = \omega\cos\theta\cos\phi\, \underline{i} + \omega\cos\theta\sin\phi\, \underline{j} - \omega\sin\theta\, \underline{k}$$

$$\vec{\varepsilon}_{\perp} = \omega\sin\phi\, \underline{i} - \omega\cos\phi\, \underline{j}$$

The ε's are perpendicular to each other and to the photon wave vector $\vec{k}$. The reason they are designated $\vec{\varepsilon}_{\parallel}$ and $\vec{\varepsilon}_{\perp}$ is that, when the propagation direction $\vec{k}$ is normal to the magnetic field (i.e. $\theta = \frac{\pi}{2}$) the electric field of the two configurations are respectively parallel and perpendicular to the magnetic field. When integrated over the azimuthal direction ϕ_k of radiation, the cross sections are

$$\frac{d\sigma_\perp}{d\theta} = \int \frac{d\sigma_\perp}{d\Omega_k}\, d\phi_k$$

$$= \frac{1}{137} Z^2 e^4 \frac{m^2}{|pp'|} \lambda^2 I^2 \omega\, d\omega \{16[(\delta\alpha_1 + \gamma\alpha_0' - \beta^2\alpha'\alpha_1)^2 + (\beta(\alpha_1 + \alpha_0') + \beta^3\alpha_1)^2] + 8\lambda^2\omega^2 \sin^2\theta [(\delta\alpha_1 + \gamma\alpha_0' - \beta^2\alpha'\alpha_1)^2 + (\beta(\alpha_1 + \alpha_1') + \beta^3\alpha_1)^2 + (\gamma^2 + \beta^2)\alpha_0'^2]\}$$

$$\frac{d\sigma_\parallel}{d\theta} = \int \frac{d\sigma_\parallel}{d\Omega_k}\, d\phi_k$$

$$= \cos^2\theta \frac{d\sigma_\perp}{d\theta} + \frac{1}{137} \frac{Z^2 e^4}{2\pi} \frac{m^2}{|pp'|} \lambda^2 I^2 \omega\, d\omega \sin^2\theta \{[(2\beta\alpha_1 + 4\beta\alpha_0' + 4\beta^3\alpha_1)^2 + (4(\alpha' + \alpha_I)\alpha_1 + 4(\alpha + \alpha_I)\alpha_0' + 2\beta^2\alpha'\alpha_1)^2 + 8(\sigma\alpha_0 + \mu\alpha_1')^2 + 8\mu^2\alpha_0'^2] \lambda^2\omega^2 \sin^2\theta + [8(\beta\alpha_1 + 2\beta\alpha_1' + 2\beta^3\alpha_1')^2 + 8[2(\alpha' + \alpha_I)\alpha_1 + 2(\alpha + \alpha_I)\alpha_1' + \beta^2\alpha'\alpha_1]^2 + 32(\beta\alpha_0' + \beta^3\alpha_0)^2 + 32[(\alpha' + \alpha_I)\alpha_0 + (\alpha + \alpha_I)\alpha_0']^2 + 16(\sigma\alpha_0 + \mu\alpha_0')^2\}$$

where $\delta = -\alpha' + \alpha_I + \alpha\beta^2$ $\qquad \gamma = \alpha - \alpha_I - \alpha'\beta^2$

$\sigma = (\alpha_I + \alpha') + \alpha\beta^2$ $\qquad \mu = (\alpha_I + \alpha) + \alpha'\beta^2$

I and the α's are defined as in (6.3), (6.8) and (6.9).

6.4 Discussion

The most natural way of checking the validity of the two enormously complicated expressions above is to see whether they go over to some simple and familiar relations in the appropriate limit. In a previous paper (Lodenquai et al 1974) it was argued that for low frequency (classical) radiation emitted perpendicular to the magnetic field, $\sigma_\parallel \to \sigma_\parallel$ (H = 0) (i.e. free electron bremsstrahlung) and $\sigma_\perp \to 0$. This is because in the first case we have essentially a free electron accelerating along the magnetic field whilst emitting radiation (since

the electric field of the radiation $\underline{E}//\underline{H}$). In the second situation the motion of the electron is no longer unrestricted, (since the direction of motion is transverse to the magnetic field) and hence $\sigma_\perp \to 0$ in the low frequency limit.

Careful examination of our present result indeed reveals that, for $\hbar\omega \to 0$ all terms in the expression for $\frac{d\sigma_\perp}{d\theta}$ go to zero. However, the surviving terms in $\frac{d\sigma_{\parallel}}{d\theta}$ give

$$\lim_{\omega\to 0} \frac{d\sigma_{\parallel}}{d\theta} = \frac{3}{137} Z^2 e^4 \lambda^2 e^{\lambda^2 a^2} \left[E_1\left(\frac{\lambda^2 a^2}{2}\right) - E_1\left(\frac{1+\lambda^2 a^2}{2}\right)\right]^2 \frac{d\omega}{\omega}$$

which does not, at first sight, resemble free electron bremsstrahlung since the characteristic quantum length λ depends on the magnetic field H.

A critical review of the argument leading to $\sigma_{\parallel} \to \sigma_{\parallel}(H = 0)$ is also illuminating. Although in this situation the electron is accelerating freely along the magnetic field, such an acceleration is (by definition) due to coulomb interaction with the positive charge. It should now be clear that the previous argument cannot be adequate as it stands because it ignores completely the presence of the fourth body, viz. the positively charged ion. In ordinary bremsstrahlung the initial and final momenta of the electron may be in certain specified directions, but there is in general momentum transfer in all three directions during the transient period of (coulomb) collision with the ion. Indeed, the similarity between the magnetic and non-magnetic processes depends crucially on the resemblance of the electron trajectory to the conventional hyperbolic Rutherford-type orbit. There are two cases :

1. Strong Magnetic Field. Low momentum transfer, i.e. $\lambda a \ll 1$. Strong magnetic field implies short time scale $\delta t \sim \frac{1}{\omega_c} \sim \frac{1}{H}$. Low momentum transfer implies low energy transfer δE. Hence $\delta E \delta t \to \hbar$ and

we are in the extreme quantum limit. In fact, if we make the small λa approximation $E_1(\frac{\lambda^2 a^2}{2}) \sim \ell n(\frac{\lambda^2 a^2}{2})$ the cross section reduces to

$$\frac{d\sigma_{II}}{d\theta} = \frac{3}{137} Z^2 e^4 \lambda^2 \left(\ell n \frac{\lambda^2 a^2}{2}\right)^2 \frac{d\omega}{\omega}$$

and does not in any way approach the classical free field bremsstrahlung. In this limit momentum transfer in the transverse direction is greatly inhibited by the presence of the strong magnetic field.

2. Weak magnetic field. Large momentum transfer. Since this is the exact opposite of case (1) we are in the familiar classical limit. In the limit of $\lambda a \gg 1$ we can use the expansion $E_1(\frac{\lambda^2 a^2}{2}) \sim (\frac{\lambda^2 a^2}{2})^{-1} e^{-\frac{\lambda^2 a^2}{2}}$ and the cross section reduces to

$$\frac{d\sigma_{II}}{d\theta} = \left(\frac{12 Z^2}{137} e^4 \frac{1}{a^2} \frac{d\omega}{\omega}\right) \frac{1}{\lambda^2 a^2}$$

which $\to 0$ as $\lambda a \to \infty$. This is not a surprising result since a max. momentum cutoff $\lambda p_{max} \sim 1$ is inherent in the present formalism (section 6.2). In fact, the extreme limit of this situation can only be $\lambda a \sim 1$ and then

$$\frac{d\sigma_{II}}{d\theta} = (.08) \times 12 \left(\frac{1}{137} Z^2 e^4 \frac{1}{a^2} \frac{d\omega}{\omega}\right) = \frac{1}{137} Z^2 e^4 \frac{1}{a^2} \frac{d\omega}{\omega} \qquad (6.11)$$

The extra factor of 0.08 is due to the fact that $E_1(\frac{\lambda^2 a^2}{2}) \neq (\frac{\lambda^2 a^2}{2})^{-1} e^{\frac{-\lambda^2 a^2}{2}}$ at $\lambda a \sim 1$. In any case the final result is (apart from a factor of $\frac{2}{\pi}$) identical to the well-known Bethe-Heitler cross section (eqn.17, p.245, Heitler, 1954). The original anticipation of Lodenquai et al (1974) is therefore fulfilled in the limit of weak field and large momentum transfer provided that the meaning of large momentum transfer in the present context of perturbation theory is properly realised.

As we depart from the low frequency limit, the cross section for both " and ⊥ modes exhibit resonances near the cyclotron frequencies. In this regime the classical picture of radiation is no longer adequate because the wavelength near the cyclotron frequency is of the same order as the radius of the first Landau orbit. Resonant emission of radiation (photons) is due to transition of the electron between adjacent Landau levels $j = 1$ and $j = 0$, and occurs whenever the energy denominators α_1^{-1}, $(\alpha_o')^{-1}$ in (6.3) vanish. Assuming a pulsar magnetic field $H \sim 0.1\, H_{cr} = 4.10^{12}$ gauss, an initial electron momentum $p_z = -140$ keV/c (corresponding to an electron with longitudinal kinetic energy ~ 10 keV moving down the field line) and a natural line width of $\delta E = 3.6 \times 10^{-2}$ keV (Lieu, 1980), the following graphs were plotted.

Fig 6.2 $\frac{d\sigma_{"}}{d\theta}$ and $\frac{d\sigma_{\perp}}{d\theta}$ (in units of $r_o^2 = (\frac{e^2}{m})^2$, $r_o \simeq$ classical electron radius) vs frequency of radiation Λ (in KeV) for the case of forward scattering of electron (see eqn (6.6)) and perpendicular propagation of photon ($\theta = \frac{\pi}{2}$). It can be seen that both modes resonate at the cyclotron frequency, in disagreement with a previous work on cyclotron line formation (Nagel 1980) which assumes that only the " mode resonate. The rise of the " mode at low frequencies is due to the well-known $\frac{1}{\omega}$ infra-red divergence (see eqn (6.11)). It is removed by a careful consideration of the cross section for bremsstrahlung of soft photons $\hbar\omega < \delta E$ where δE is the energy resolution of the detector. We are not concerned with this extreme low frequency limit. (N.B. the same behaviour of $\frac{d\sigma_{"}}{d\theta}$ and $\frac{d\sigma_{\perp}}{d\theta}$ as $\omega \to 0$ is expected for the case of oblique propagation $\theta \neq \pi/2$).

Figs 6.3&6.4 Plots of the total cross section $\frac{d\sigma}{d\theta}$ for unpolarised radiation propagating at $\theta = 0$, $\frac{\pi}{4}$, and for forward scattering of electron. A small splitting of the cyclotron line is due to the slight difference in resonance frequencies of α_1 and α_o'. Such a phenomenon is much more pronounced in fig 6.5.

Fig 6.5 Total cross section $\frac{d\sigma}{d\theta}$ for $\theta = 0$ is given for the case of backward scattering of the electron (max. momentum transfer, see eqn (6.6)). The most important implication of Fig.3-5 is that, if bremsstrahlung is indeed one of the mechanisms responsible for cyclotron line formation in the accretion column of binary X-ray pulsars (Nagel, 1980), then one would not in general expect a unique, narrow emission or absorption line feature near the cyclotron frequency.

Fig 6.6 Polar diagram for monochromatic, unpolarised radiation at energy $\hbar\omega = 25$ keV. It can be seen that the emission is predominantly in the direction of the magnetic field.

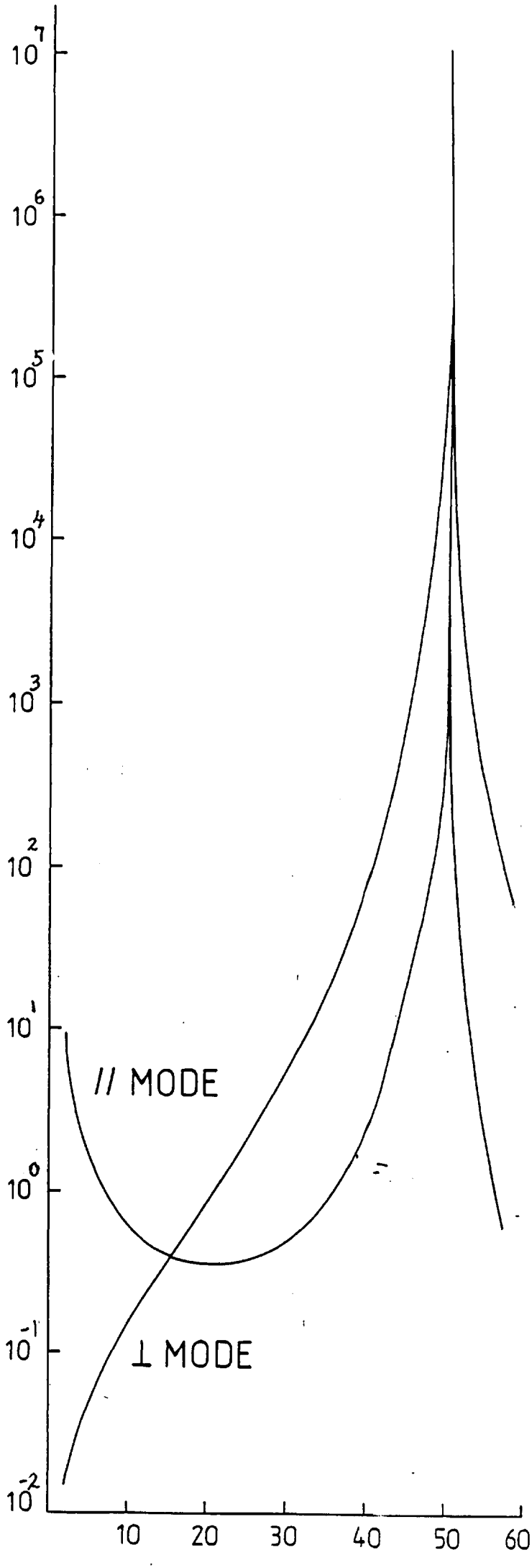


FIG 6.2
For key to diagram see text (p.96)

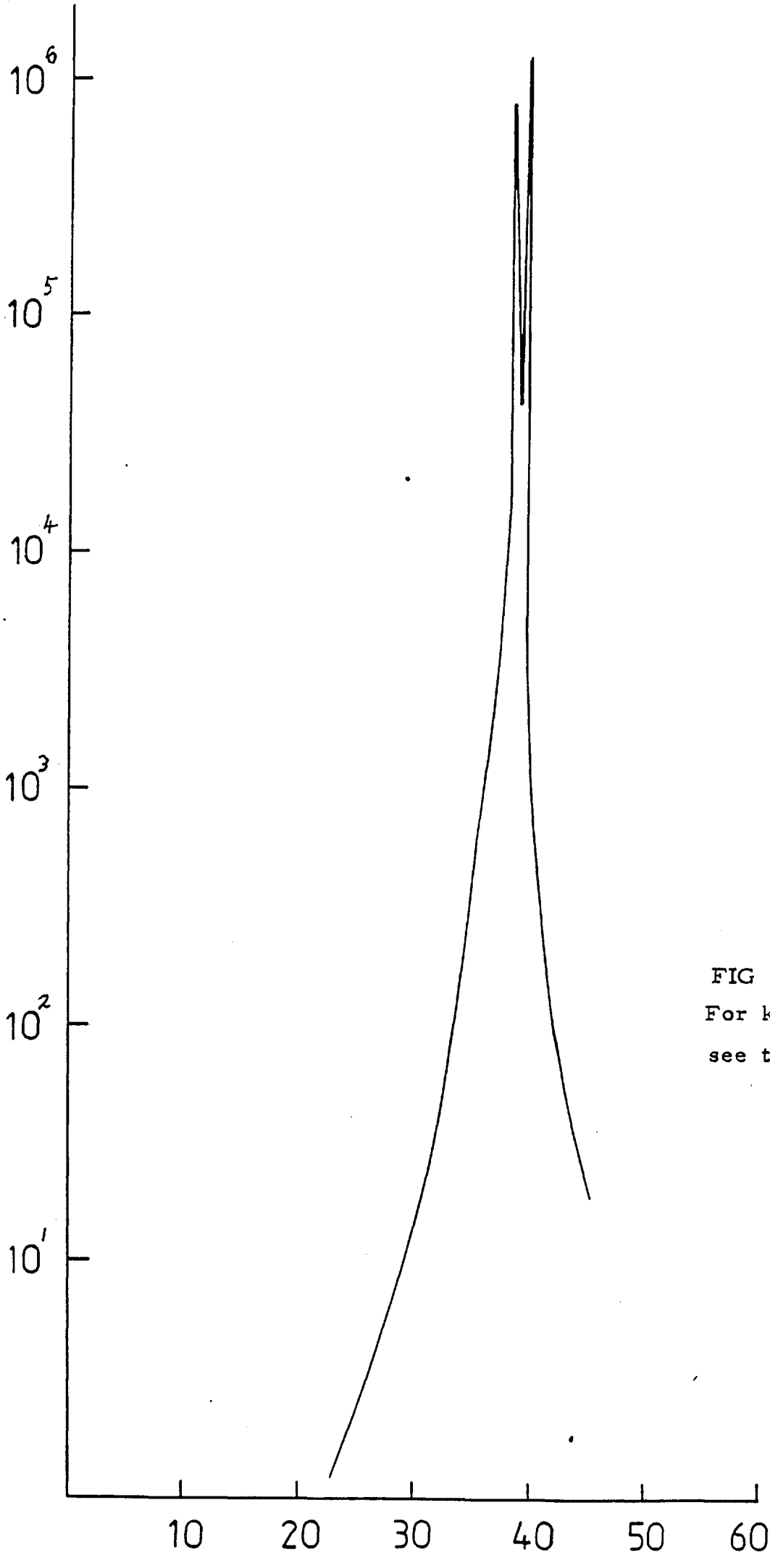


FIG 6.3
For key to diagram
see text (p.96)

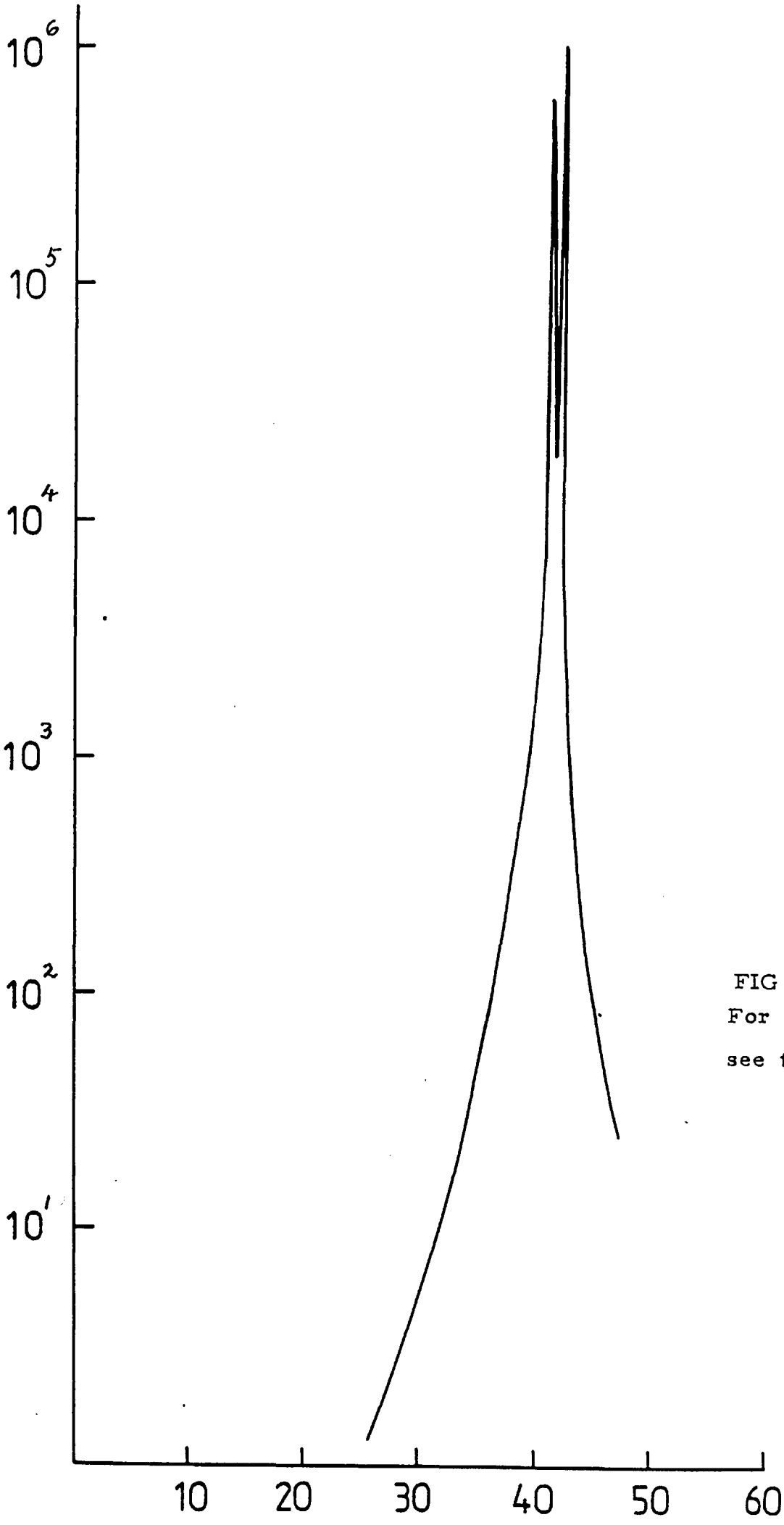


FIG 6.4
For key to diagram
see text (p.96).

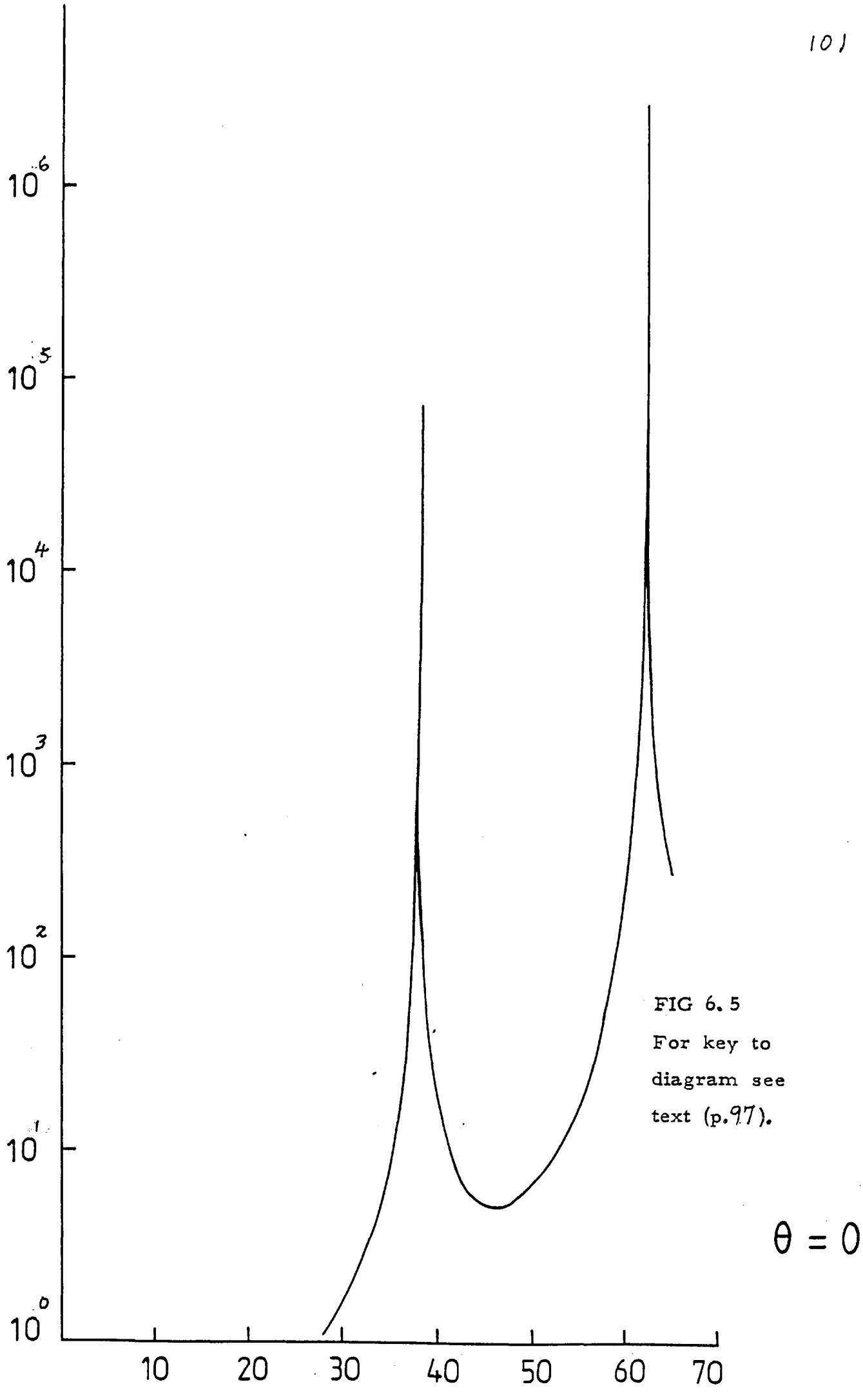


FIG 6.5
For key to diagram see text (p.97).

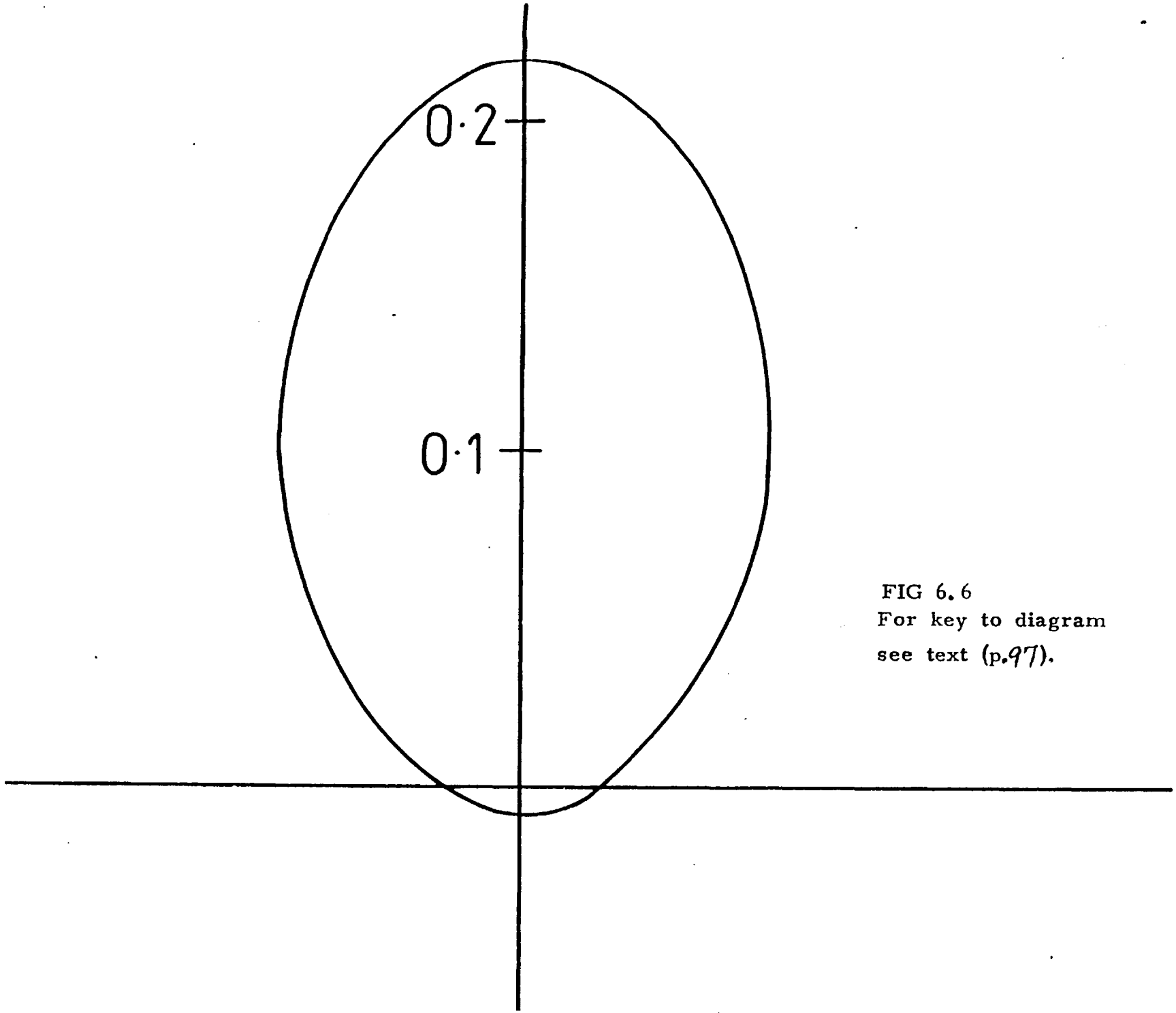


FIG 6.6
For key to diagram
see text (p.97).

REFERENCES

Adler, S.L., 1971, Ann. Phys. (NY), 67, 599.

Becker, R.H. et al, 1978, Astrophys. Journal, 221, 912.

Becklin, E. et al. 1973, Nature, 245, 302.

Bjorken, J.D., Drell, S.D., 1964, Relativistic Quantum Mechanics, pp.103, McGraw-Hill.

Boldt, E.A. et al, 1976, Astron. Astrophys., 50 (2), 161.

Bowyer, C.S. et al, 1964a, Nature, 201, 1307.

Bowyer, C.S.et al, 1964b, Science, 146, 912.

Bowyer, C.S. et al, 1970, Astrophys. Journal, 161, L1.

Braes, L., Miley, G., 1971, Nature, 232, 246.

Braes, L., Miley, G., 1972, Nature, 237, 506

Brussaard, P.J., Van de Hulst, H.C., 1962, Rev. Mod. Phys., 34, (3), 507.

Canuto, V., Chiu, H.Y., Fassio-Canuto, L., 1969, Phys. Rev., 185 (5), 1607.

Canuto, V., Lodenquai, J., Ruderman, M., 1971, Phys. Rev., D3, 2303.

Carpenter, G.F., Coe, M.J., Engel, A.R., 1976, Nature, 259, 99.

Chiu, H.Y., Fassio-Canuto, L., Phys. Rev., 1969, 185 (5), 1614.

Coe, M.J., 1976, PhD Thesis, Imperial College London.

Cooke, B.A. et al, 1978, Mon. Not. Roy. Astr. Soc. 182, 661.

Cruise, A.M., Willmore, A.P., 1975, Mon. Not. Roy. Astr. Soc., 170, 165.

Daugherty, J.K., Ventura, J., 1978, Phys. Rev., D18, 1053.

Davidsen, A., 1975, I.A.U. Circ. No. 2824.

Elvis, M.S. et al, 1978, Mon Not. Roy. Astr. Soc., 183, 129.

Engel, A.R., Coe, M.J., 1977, Space Science Instrumentation, 3, 407.

Evans, A.J., Quenby, J.J., Engel, A.R., 1980, Astron. Astrophys. (supp.Ser.), 41, 13.

Giacconi, R. et al, 1962, Phys. Rev. Lett., 9, 439.

Giacconi, R. et al, 1971, Astrophys. Journal, 167, L67.

Giacconi, R. et al, 1974, Astrophys. Journal Supp. 27, 37.

Giacconi, R., Gursky, H., 1974, X-ray Astronomy, D. Reidel Pub. Co., Dordrecht-Holland.

Giacconi R. et al, 1979, Astrophys. Journal, 230, 540.

Gnedin, Y.N., Pavlov, G.G., 1974, Sov. Phys. JETP, 38, 403.

Gnedin, Y.N., Sunyaev, R.A. 1973, Astron. Astrophys., 25, 233.

Gnedin, Y.N., Sunyaev, R.A., 1974, Astron. Astrophys., 36, 379.

Gorenstein, P., Tucker, W.H., 1976, Ann. Rev. Astron. Astrophys., 14, 373.

Gradshteyn, I.S., Ryzhik, I.M., 1965, Table of Integrals and Products, Academic Press.

Gursky, H. et al, 1978, Astrophys. Journal, 223, 973.

Hayakawa, S., Matsuoka, M. 1964, Progr. Theor. Phys. Supp., 30, 204.

Heitler, W., 1954, The Quantum Theory of Radiation, Oxford.

Herold, H., 1979, Phys. Rev., D19 (10), 2868.

Holt, S.S. et al, 1976, Nature, 261, 213

Johnson, M.H., Lippmann, B.A., 1949, Phys. Rev., 76,828.

Kaitna, R., Urban, P., 1964, Nuclear Phys., 56, 518.

Kellogg, E. et al, 1971, Astrophys. Journal, 165, L49.

Kellogg, E., 1973, I.A.U. Symp., 55, 171.

Kopal, Z., 1959, Close Binary Systems, Chapman Hall and John Wiley, New York.

Lamb, F.K., Pethick, C.J., Pines, D., 1973, Astrophys. Journal 184, 271.

Lewin, W.H.G., 1978, Workshop of Cyclotron Lines from Accreting Neutron Stars, Munich.

Lieu, R., 1980, Astrophys. and Space Sci., 73, 481.

Lodenquai, S., Canuto, V., Ruderman, M., Tsuruta, S., 1974, Astrophys. Journal, 190, 141.

McClintock, J.E. et al, 1977, Nature, 270, 320.

McClintock, J.E., 1977, I.A.U. Circ. No., 3088

Mertz, L., 1967, Modern Optics, pp.787, Brooklyn Polytechnic Press, New York.

Mészáros, P., 1978, Astron. Astrophys., 63, L19.

Mészáros, P., Ventura, J., 1978, Phys. Rev. Lett., 41, 1544.

Mészáros, P., Ventura, J., 1979, Phys. Rev., D19, 3565.

Nagel, W., 1980, Astrophys. Journal, 236, 904.

Nishimura, J., 1975, Proc. 14th Int. Cosmis Rays Conf. München, 12, 4091.

Oda, M., 1965, Applied Optics, 4, 143.

Oda, M. et al, 1965, Nature, 205, 554.

Parsignault, D.R., et al, 1972, Nature Phys. Sci. 239, 123.

Pavlov, G.G., Panov, A.N., 1976, Sov. Phys. JETP, 44(3), 300.

Pomraning, G.C., 1973, The Equations of Radiation Hydrodynamics, Pergamon, New York.

Pravdo et al, 1979, Astrophys. Journal, 231, 912.

Prendergast, K., Burbidge, G., 1968, Astrophys. Journal, 15, L83.

Primini, F.A. et al, 1980, Edi. Attn., Astrophys. Journal.

Pringle, J.E., Rees, M.J., 1972, Astron. Astrophys. 21, 1.

Rappaport, S. et al, 1971, Astrophys. Journal, 168, L17.

Ricker, G.R. et al, 1975, Astrophys. Journal, 197, L83.

Ricker, G.R. et al, 1978, Nature, 271, 35.

Rose, M.E., 1961, Relativistic Electron Theory, John Wiley and Sons.

Rose, W.K., 1973, Astrophysics, Rinehart and Winston Inc.

Schnopper, H.W., Thompson, R.I., 1968, Space Science Reviews, 8, 534.

Schnopper, H.W. et al, 1970, Astrophys.Journal, 161, L161.

Schnopper, H.W. et al, 1976, Astrophys. Journal, 210, L75.

Tananbaum, H. et al, 1972, Astrophys. Journal, 174, L143.

Tananbaum, H. et al, 1978, Astrophys. Journal, 223, 74.

Trümper, J. et al, 1977, Ann. N.Y. Acad. Sci., 302, 538.

Ventura, J., 1979a, Phys. Rev., D19, 1684.

Ventura, J., 1979b, Astrophys. Journal, 233, L125.

Virtamo, J., Jauho, P., 1975, Nuovo Cimento, 26B (2), 537.

Watson, M.G., Griffiths, R.E., 1977, Mon. Not. Roy. Astr. Soc., 178, 513.

Webster, B., Murdin, P., 1972, Nature, 235, 37.

Wheaton, J. et al, 1978, IAU Circ. No.3238.

Yahel, R.Z., 1979, Astrophys. Journal, 229, L73.

```
FORTRAN IV      V02.04          TUE 29-JAN-80 16:40:00          PAGE 001
COPE=14K, UIC=[7,3]                          DK2:LADMOC,LADMOC=DK2:LADMOC

      C
0001          COMMON /DATA/ ISFN,ISFNX,VMAG1,VMAG2,HA,DEC
0002          REAL LAMBDA
0003          ASIN(X)=ATAN(X/SQRT(1.-X*X))
0004          WRITE (4,100)
0005     100    FORMAT (1X,' ENTER NO. OF BLOCKS,DN, LOCATION',/,' (1 IF
             1ALICE SPRING,2 IF MILDURA)',/,' RA & DEC OF SOURCE
             2FORMAT I3,I4,I2,2F8.3',/)
0006          READ (4,200) NBLOCK,IDN,IL,SRA,SDEC
0007     200  FORMAT (I3,I4,I2,2F8.3)
0008          LP=3
      C       PROGRAM TO CHECK INPUT READ
      C       READ IN NO OF BLOCKS AS PER NBLOCK
      C       AND THEN PROCESS IT
0009          DO 30 I=1,NBLOCK
0010          CALL NEXT(IFLAG)
0011          IF (IFLAG .EQ. 0) GOTO 30
      C       PROCESS DATA
0013     300  WMAG1=(VMAG1-4.743)/1.9855
0014          WMAG2=(VMAG2-4.7165)/1.9275
0015          IF((ABS(WMAG1).GE.1.0).OR.(ABS(WMAG2).GE.1.0)) GO TO 30
0017     110  PHI1=ASIN(WMAG1)
0018          PHI2=ACOS(WMAG2)
0019          IF ((WMAG1 .LT. 0.) .AND. (WMAG2 .GT. 0.)) PHI=(PHI1+PHI2)/2.0
0021          IF ((WMAG1 .GT. 0.) .AND. (WMAG2 .LT. 0.)) PHI=3.14159-(PHI1
             1+(3.14159-PHI2))/2.0
0023          IF ((WMAG1 .LT. 0.) .AND. (WMAG2 .GT. 0.))PHI=6.28318-
             1(ABS(PHI1)+(PHI2))/2.0
0025          IF ((WMAG1 .LT. 0.) .AND. (WMAG2 .LT. 0.))PHI=3.14159+(ABS(PHI1))+
             1(3.14159-PHI2))/2.0
0027          IF ((WMAG1)*(WMAG2) .EQ. 0.0)PHI=0.0
0029     600  HA=(HA/180.)*3.14159
0030            PRA=HA
0031          PDEC=DEC
0032          DEC=(DEC/180.0)*3.14159
0033          IF (IL .EQ.2)LAMBDA=.6109
0035          PSI=SIN(LAMBDA)
0036          ETA=COS(LAMBDA)
0037          DEC=DEC-LAMBDA
0038          SQSIN=(SIN(HA))**2.0
0039          SQCOS=(COS(HA))**2
0040          F=ETA**2*SQSIN+SQCOS+2.0*PSI**2*SQSIN
             1+(PSI**4*SQSIN)/(ETA**2)+(PSI**2*SQCOS)/
             2ETA**2
0041          G=2.0*PSI*SQSIN*SIN(DEC)+2.0*PSI**3.0*SQSIN*
             1(SIN(DEC)/ETA**2)+(2.0*PSI*SQCOS*SIN(DEC))/
             2ETA**2
0042          H=((SIN(DEC))**2.0*(PSI**2.0*SQSIN+SQCOS))/
             1ETA**2-SQCOS
0043          C=(-G+(G**2.0-4.0*F*H)**0.5)/(2.0*F)
0044          IF (C .LE. 0.0) GOTO 29
0046          A=-(C*PSI+SIN(DEC))/ETA
0047          B=(1.0-A**2.0-C**2.0)**.5
0048          IF (HA .LT. 3.14159) B=-B
```

```
0050          AP=A*COS(PHI)+B*SIN(PHI)
0051          BP=-A*SIN(PHI)+B*COS(PHI)
0052          CP=C
0053          COSHA=-(AP*PSI-CP*ETA)/((AP*PSI-CP*ETA)**2.0+BP**
             1     2.0)**.5
0054          SINDEC=ETA*AP+PSI*CP
0055          RDEC=ASIN(SINDEC)
0056             RDEC=ABS(RDEC)
0057             IF(SINDEC.GT.0.0) RDEC=-RDEC
0059          RDEC=(RDEC*180./3.14159
0060          RHA=ACOS(COSHA)
0061          IF (BP .GT. 0.0) RHA=-ABS(RHA)
0063          EST=(19746.592+(1800.*ISFNX+ISFN)*.5128)
0064          TL=(EST/3600.)-.52766
0065          ST=12.+((IDN-82)*24.)/366.2422+TL*1.00273
0066          IF (ST .GE. 24.)ST=ST-24.
0068          RST=ST*15.
0069          RA=RST+(RHA*180./3.14159)
0070          H=EST/3600.
0071          IH=IFIX(H)
0072          AM=(EST -IH*3600.)/60.
0073          IM=IFIX(AM)
0074          S=(EST-IH*3600.-IM*60)
0075          RRA=(RA-SRA)*COS(((RDEC+SDEC)*3.14159
             1/360.))*3.14159/180.
0076             RRDEC=(RDEC-SDEC)*3.14159/180.
0077          DEV=ACOS((COS(RRA)*COS(RRDEC)))*(180
             1/3.14159)
0078          PHI=(PHI*180.)/3.14159
0079          WRITE(LP,9999)IH,IM,S,ISFNX,ISFN,RA,RDEC,
             1PRA,PDEC,PHI,DEV
0080          GO TO 30
0081       29 WRITE (LP,1001) C
0082     9999  FORMAT (1X,I2,I3,F7.3,I4,I5,6F12.3)
0083     1001  FORMAT (1X,'C= ',F7.3,/)
0084       30  CONTINUE
         C     WRITE OUTPUT
0085          CALL SPOOL(LP)
0086          STOP
0087          END
```